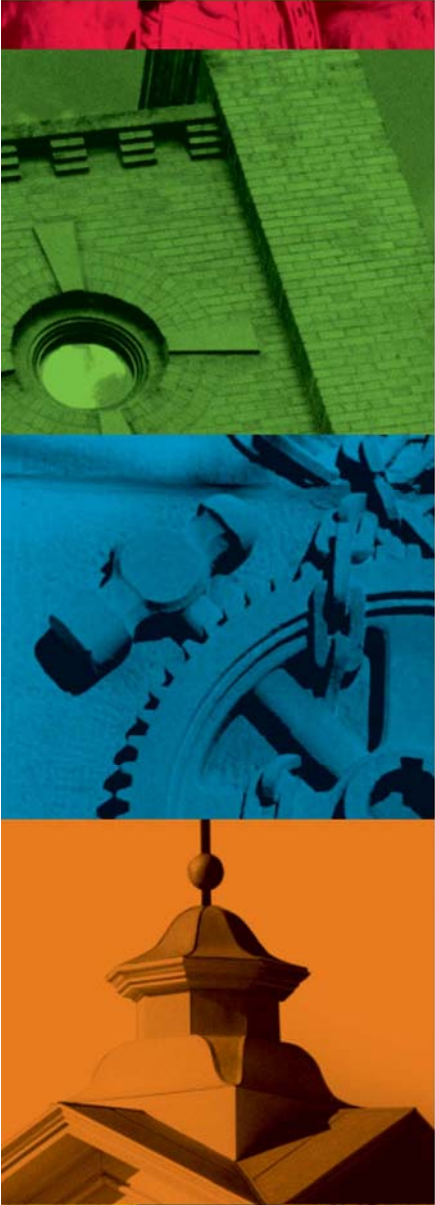




MISSOURI
S&T

CENTER FOR INFRASTRUCTURE ENGINEERING STUDIES



DEVELOPMENT AND ASSESSMENT OF TRANSPARENT SOIL AND PARTICLE IMAGE VELOCIMETRY IN DYNAMIC SOIL- STRUCTURE INTERACTION

by

HONGHUA ZHAO



**UTC
R155**

**A University Transportation Center Program
at Missouri University of Science & Technology**

Disclaimer

The contents of this report reflect the views of the author(s), who are responsible for the facts and the accuracy of information presented herein. This document is disseminated under the sponsorship of the Department of Transportation, University Transportation Centers Program and the Center for Infrastructure Engineering Studies UTC program at the University of Missouri - Rolla, in the interest of information exchange. The U.S. Government and Center for Infrastructure Engineering Studies assumes no liability for the contents or use thereof.

Technical Report Documentation Page

1. Report No. UTC R155	2. Government Accession No.	3. Recipient's Catalog No.	
4. Title and Subtitle DEVELOPMENT AND ASSESSMENT OF TRANSPARENT SOIL AND PARTICLE IMAGE VELOCIMETRY IN DYNAMIC SOIL-STRUCTURE INTERACTION		5. Report Date February 2007	
		6. Performing Organization Code	
7. Author/s HONGHUA ZHAO		8. Performing Organization Report No. 00008811	
9. Performing Organization Name and Address Center for Infrastructure Engineering Studies/UTC program Missouri University of Science & Technology 223 Engineering Research Lab Rolla, MO 65409		10. Work Unit No. (TRAIS)	
		11. Contract or Grant No. DTRS98-G-0021	
12. Sponsoring Organization Name and Address U.S. Department of Transportation Research and Special Programs Administration 400 7 th Street, SW Washington, DC 20590-0001		13. Type of Report and Period Covered Final	
		14. Sponsoring Agency Code	
15. Supplementary Notes			
<p>16. Abstract</p> <p>This research combines Particle Image Velocimetry (PIV) and transparent soil to investigate the dynamic rigid block and soil interaction. In order to get a low viscosity pore fluid for the transparent soil, 12 different types of chemical solvents were tested and the two best-matching pore fluids were identified. Transparent soil was adopted in the research as a substitute for natural sand. To examine the dynamic properties of transparent soil, a series of resonant column tests were carried out on dry silica gel under different confining pressures. The test results showed that transparent soil has a similar dynamic behavior as natural soil under low confining pressure. Hence, transparent soil can be used as an effective substitute for natural soil in the shake table test, in which the confining pressure is usually lower than 400 kPa.</p> <p>A neural network-based camera calibration algorithm was developed for the PIV technique. Its application was illustrated through a case study of a rectangular strip footing by modifying the MatPIV code. The neural network camera calibration model was also compared with the linear model and second-order polynomial model. The comparison proved that the neural network camera calibration model is the most effective method.</p> <p>Three shake table tests were conducted in this research. The free-field motion shake table test clearly showed the amplification effects as the wave propagated upward from the bottom. Two shake table tests conducted on a small-scale rigid wood model investigated the interaction between the block and the soil under the input of 2-Hz, 0.25- inch and 2-Hz, 0.5-inch sinusoidal waves. The testing results from the shake table test showed that the rigid wood block failed by the bearing capacity type of failure. The larger amplitude of the input motion at the same frequency would more easily topple the rigid block. The shake table test has also showed the near-field and far-field effects due to the soil-structure interaction. The near-field soil motion was significantly influenced by the motion of the rigid block. The far-field soil motion was unaffected by the motion of the rigid block. This research shows that transparent soil combined with PIV can be a powerful tool for future research in the field of dynamic geomechanics.</p>			
17. Key Words Liquefaction		18. Distribution Statement No restrictions. This document is available to the public through the National Technical Information Service, Springfield, Virginia 22161.	
19. Security Classification (of this report) unclassified	20. Security Classification (of this page) unclassified	21. No. Of Pages 150	22. Price

DEVELOPMENT AND ASSESSMENT OF TRANSPARENT SOIL AND PARTICLE
IMAGE VELOCIMETRY IN DYNAMIC SOIL-STRUCTURE INTERACTION

by

HONGHUA ZHAO

A DISSERTATION

Presented to the Faculty of the Graduate School of the

UNIVERSITY OF MISSOURI-ROLLA

In Partial Fulfillment of the Requirements for the Degree

DOCTOR OF PHILOSOPHY

in

CIVIL ENGINEERING

2007

Yu-Ning Ge, Advisor

Thomas M. Petry

Ronaldo Luna

Richard W. Stephenson

Genda Chen

J. David Rogers

© 2007

Honghua Zhao

All Rights Reserved

ABSTRACT

This research combines Particle Image Velocimetry (PIV) and transparent soil to investigate the dynamic rigid block and soil interaction. In order to get a low viscosity pore fluid for the transparent soil, 12 different types of chemical solvents were tested and the two best-matching pore fluids were identified. Transparent soil was adopted in the research as a substitute for natural sand. To examine the dynamic properties of transparent soil, a series of resonant column tests were carried out on dry silica gel under different confining pressures. The test results showed that transparent soil has a similar dynamic behavior as natural soil under low confining pressure. Hence, transparent soil can be used as an effective substitute for natural soil in the shake table test, in which the confining pressure is usually lower than 400 kPa.

A neural network-based camera calibration algorithm was developed for the PIV technique. Its application was illustrated through a case study of a rectangular strip footing by modifying the MatPIV code. The neural network camera calibration model was also compared with the linear model and second-order polynomial model. The comparison proved that the neural network camera calibration model is the most effective method.

Three shake table tests were conducted in this research. The free-field motion shake table test clearly showed the amplification effects as the wave propagated upward from the bottom. Two shake table tests conducted on a small-scale rigid wood model investigated the interaction between the block and the soil under the input of 2-Hz, 0.25-inch and 2-Hz, 0.5-inch sinusoidal waves. The testing results from the shake table test showed that the rigid wood block failed by the bearing capacity type of failure. The larger amplitude of the input motion at the same frequency would more easily topple the rigid block. The shake table test has also showed the near-field and far-field effects due to the soil-structure interaction. The near-field soil motion was significantly influenced by the motion of the rigid block. The far-field soil motion was unaffected by the motion of the rigid block. This research shows that transparent soil combined with PIV can be a powerful tool for future research in the field of dynamic geomechanics.

ACKNOWLEDGMENTS

I would like to express my gratitude to my advisor, Dr. Yu-Ning Ge, for his support and advice throughout this research work. I would also like to thank Dr. Thomas Petry for his instructions on carrying out this research work, as well as for his support, and encouragement. I greatly appreciate the comments and advice from Dr. Ronaldo Luna, Dr. Richard Stephenson, Dr. David Rogers, and Dr. Genda Chen, and I am thankful for their continued support and encouragement. Furthermore, I would like to thank Dr. Shamsheer Prakash and Dr. Salah Taqieddin for their review and comments, which have been of great help to this research. I am also thankful for Dr. David C. Van Aken for his help with some of the tensile tests carried out in the research.

Many current graduate students and former graduate students have assisted me with the difficulties of my Ph.D. studies. These students include: Adam Sevi, Ali Izadi, Quevedo Torres Mariel Rocio, Dr. Wanxing Liu, Dr. Wei Zheng, Dr. Yong Wu, Dr. Yu-Puh Han, Dr. Cheng-Ping Jiang, Mikel Ludwikosky, and Benjamin Kudlacek. I would like to express my sincere appreciation to each of these students.

I would also like to thank the great technicians in the Civil Engineering Department—Steve Gabel, Jeff Bradshaw, Garry Abbott, and Bill Frederickson—for their assistance in setting up the tests and for their equipment training. Without their help, it would have been impossible to accomplish this research. Also, I would like to thank Miss Kathryn B. Mudd for her great editing work.

In addition, I would like to thank my friends for all of their support and encouragement during my time in Rolla. They are Hongxia Ning, Veeraraghavan Preetha, Dr. Xijing Bi, Dr. Wen Liang, Dr. Xinlin Shi, Ke Wang, Xiaohua Wang, Vivek Yadav, Xiaowen Guo, Wanrong Yin, Thidaporn Supapakorn, Pooja Kapil, and Dr. Wenjian Wang. They brought a lot of happy times to my four and a half years of Ph.D. life.

Finally and most importantly, I would like to express deep appreciation for the support of my family. They are the source of energy that has kept me persistent with my research work, and without them this could not have happened.

TABLE OF CONTENTS

	Page
ABSTRACT	iii
ACKNOWLEDGMENTS	iv
LIST OF ILLUSTRATIONS	v
LIST OF TABLES	vi
SECTION	
1. INTRODUCTION.....	1
1.1. MOTIVE OF THE RESEARCH	1
1.2. PROBLEM STATEMENT	3
1.3. DISSERTATION OUTLINE.....	3
2. LITERATURE REVIEW	5
2.1. INTRODUCTION	5
2.2. TRANSPARENT SOIL	5
2.3. MECHANICAL PROPERTIES OF TRANSPARENT SOIL.....	6
2.4. DYNAMIC SOIL-STRUCTURE INTERACTION	7
2.5. PARTICLE IMAGE VELOCIMETRY (PIV).....	9
2.6. PIV APPLICATION IN GEOTECHNICAL ENGINEERING RESEARCH..	12
2.7. CAMERA CALIBRATION FOR PIV	18
3. LOW VISCOSITY PORE FLUID FOR TRANSPARENT SOIL.....	20
3.1. INTRODUCTION	20
3.2. TEMPERATURE VARIATION OF REFRACTIVE INDEX AND VISCOSITY OF SOLVENTS	20
3.3. DETERMINATION OF THE MATCHING REFRACTIVE INDEX	30
3.4. INVESTIGATION ON THE INTERACTIONS BETWEEN THE PORE FLUID AND THE LATEX MEMBRANE.....	39
3.4.1. Immersion Test.....	39
3.4.2. Tensile Test	42
3.5. DISCUSSION ON THE LOW VISCOSITY PORE FLUID FOR THE SHAKE TABLE TEST	46
3.6. SUMMARY.....	47

4. DYNAMIC MECHANICAL BEHAVIOR OF TRANSPARENT SILICA GEL ..	49
4.1. INTRODUCTION	49
4.2. METHOD TO EVALUATE DYNAMIC PROPERTIES OF SOIL	49
4.3. TESTING PROGRAM AND SAMPLE PREPARATION	52
4.4. RESONANT COLUMN TEST RESULTS	54
4.4.1. Small-Strain Shear Modulus of Silica Gel	55
4.4.2. Modulus Reduction Behavior and Damping Characteristics of Silica Gel	55
4.4.3. Discussion on Damping Ratio Determination by the Half-Power Method and Free Vibration Method	70
4.5. SUMMARY	72
5. THE CAMERA CALIBRATION AND APPLICATION INTO PIV	74
5.1. INTRODUCTION	74
5.2. CAMERA CALIBRATION DATA	74
5.3. THE NEURAL NETWORK CALIBRATION MODEL	74
5.3.1. Training Function	76
5.3.2. The Neural Network Model Validation	76
5.4. COMPARISON OF DIFFERENT CALIBRATION MODELS	77
5.5. THE ANGLE ERROR ANALYSIS	80
5.6. THE APPLICATION OF THE CALIBRATION IN THE PARTICLE IMAGE VELOCIMETRY	82
5.7. SUMMARY	86
6. VISUALIZATION OF DYNAMIC RIGID-BLOCK AND SOIL INTERACTION	87
6.1. INTRODUCTION	87
6.2. 1-G SHAKE TABLE TEST	87
6.2.1. The Similitude Law for the Shake Table Test	88
6.2.2. The Model Container	92
6.2.3. The Shake Table System	92
6.2.4. The Rigid-Block Model	93
6.2.5. The Transparent Soil Model	94
6.2.6. The Shake Table Test Setup	94

6.2.7. The Shake Table Test Program	95
6.2.7.1. Examination of the PIV algorithm.....	96
6.2.7.2. The free-field motion of transparent soil model	101
6.2.7.3. The shake table tests on the rigid-block and soil interaction	107
6.2.7.4. The motion of the transparent soil and the rigid-block during the shaking	110
6.6. SUMMARY	118
7. CONCLUSIONS AND FUTURE RESEARCH RECOMMENDATIONS.....	120
7.1. CONCLUSIONS.....	120
7.2. RECOMMENDATIONS FOR FUTURE RESEARCH WORK	122
APPENDIX.....	124
BIBLIOGRAPHY.....	130
VITA	136

LIST OF ILLUSTRATIONS

Figure	Page
2.1. A Particle Image Velocimetry System to Measure the Flow Velocity	10
2.2. Velocity Vector Field of a High-Speed Land Impact into the Water	11
2.3. Schematic of a Vertically Oscillating Box and PIV Setup	11
2.4. Image Captured after 45 s of Vertical Oscillation	11
2.5. Displacement Vectors Showing a Convective Roll	12
2.6. The Image of Ottawa Sand in Contact with the Steel Plate	13
2.7. The Displacement Vectors from the Image Analysis	13
2.8. Displacement Field around Plane Strain Displacement in Sand	14
2.9. The Schematic Diagram of the Experimental Setup Used for Applying Footing Displacements on the Transparent Synthetic Soil Model	14
2.10. DIC Analysis Results: the Arrows Indicate Spatial Displacements in Transparent Soil Slice	15
2.11. Typical Digital Image of Sand Sample Taken During a Biaxial Test.	16
2.12. DIC-Measured Displacements Surrounding a Persistent Shear Band	16
2.13. Example Image from a Plane Strain Foundation Test	17
2.14. Instantaneous Velocity Field of the Skirted Strip Foundation Subject to the Eccentric Load	17
2.15. The Illustration of Camera Calibration Concept	19
3.1. The AR200 Digital Handheld Refractometer	22
3.2. The Refractive Index Variation with the Temperature for Acetonitrile	24
3.3. The Refractive Index Variation with the Temperature for Heptane	25
3.4. The Refractive Index Variation with the Temperature for 2, 2, 4- Trimethylpentane	25
3.5. The Refractive Index Variation with the Temperature for Cyclohexane	26
3.6. The Refractive Index Variation with the Temperature for 2 Propanol	26
3.7. The Refractive Index Variation with the Temperature for Toluene	27
3.8. The Refractive Index Variation with the Temperature for Iso-Butanol	27
3.9. The Refractive Index Variation with the Temperature for Pyridine	28
3.10. The Refractive Index Variation with the Temperature for Norpar 12	28

3.11. The Refractive Index Variation with the Temperature for Lamp Oil	29
3.12. The Refractive Index Variation with the Temperature for Methyl Ethyl Ketone...	29
3.13. The Refractive Index Variation with the Temperature for Ethyl Acetate	30
3.14. The Cannon-Fenske Viscometer Tube, No. 25	31
3.15. The Viscosity Variation of Acetonitrile with Temperature	31
3.16. The Viscosity Variation of Heptane with Temperature	32
3.17. The Viscosity Variation of 2, 2, 4,-Trimethylpentane with the Temperature	32
3.18. The Viscosity Variation of Cyclohexane with the Temperature	33
3.19. The Viscosity Variation of 2 Propanol with the Temperature	33
3.20. The Viscosity Variation of Toluene with the Temperature	34
3.21. The Viscosity Variation of Iso-Butanol with the Temperature	34
3.22. The Viscosity Variation of Lamp Oil with the Temperature	35
3.23. The Viscosity Variation of Methyl Ethyl Ketone with the Temperature	35
3.24. The Viscosity Variation of Pyridine with the Temperature.....	36
3.25. The Viscosity Variation of Norpar12 with the Temperature	36
3.26. The Viscosity Variation of Ethyl Acetate with Temperature	37
3.27. The Membrane before the Immersion Test	41
3.28. The Membrane at 40 hrs after the Immersion Test	41
3.29. The Tensile Test Setup for the Latex Membranes	44
3.30. The Typical Testing Results for the Membrane of Low Degradation	44
3.31. The Stress-Strain Curve for the Latex Membranes Immersed into Different Chemical Solvent Mixtures.....	46
4.1. Typical Strain Level Associated with Different Laboratory Tests and Field Events.....	50
4.2. Classification of Dynamic Methods of Obtaining the Shear Modulus	51
4.3. GCTS Resonant Column Apparatus	52
4.4. Grain Size Distribution for Tested Silica Gel	53
4.5. Variation of the Small-Strain Shear Modulus of Silica Gel	56
4.6. Shear Modulus Degradation with Shear Strain for a 0.5-5 mm Loose Silica Gel Sample under Different Confining Pressures	57
4.7. Normalized Shear Modulus Degradation with Shear Strain for a 0.5-5 mm Loose Silica Gel Sample under Different Confining Pressures	57

4.8. Shear Modulus Degradation with Shear Strain for a 0.5-5 mm Dense Silica Gel Sample under Different Confining Pressures	58
4.9. Normalized Shear Modulus Degradation with Shear Strain for a 0.5-5 mm Dense Silica Gel Sample under Different Confining Pressures	58
4.10. Shear Modulus Degradation with Shear Strain for a 0.5-1 mm Loose Silica Gel Sample under Different Confining Pressures.	59
4.11. Normalized Shear Modulus Degradation with Shear Strain for a 0.5-1 mm Loose Silica Gel Sample under Different Confining Pressures	59
4.12. Shear Modulus Degradation with Shear Strain for a 0.5-1 mm Dense Silica Gel Sample under Different Confining Pressures	60
4.13. Normalized Shear Modulus Degradation with Shear Strain for a 0.5-1 mm Dense Silica Gel Sample under Different Confining Pressures	60
4.14. Shear Modulus Degradation with Shear Strain for a 1-3 mm Loose Silica Gel Sample under Different Confining Pressures	61
4.15. Normalized Shear Modulus Degradation with Shear Strain for a 1-3 mm Loose Silica Gel Sample under Different Confining Pressures	61
4.16. Shear Modulus Degradation with Shear Strain for a 1-3 mm Dense Silica Gel Sample under Different Confining Pressures	62
4.17. Normalized Shear Modulus Degradation with Shear Strain for a 1-3 mm Dense Silica Gel Sample under Different Confining Pressures	62
4.18. Shear Modulus Degradation with Shear Strain for a 2-5 mm Loose Silica Gel Sample under Different Confining Pressures	63
4.19. Normalized Shear Modulus Degradation with Shear Strain for a 2-5 mm Loose Silica Gel Different Confining Pressures	63
4.20. Shear Modulus Degradation with Shear Strain for a 2-5 mm Dense Silica Gel Sample under Different Confining Pressures	64
4.21. Normalized Shear Modulus Degradation with Shear Strain for a 2-5 mm Dense Silica Gel Sample under Different Confining Pressures	64
4.22. Variation of Shear Modulus for Sand and Silica Gel with Shear Strain at the Confining Pressure of 100kPa	65
4.23. Damping Ratio Variation of 0.5-5 mm Loose Silica Gel with Shear Strain	66
4.24. Damping Ratio Variation of 0.5-5 mm Dense Silica Gel with Shear Strain	67
4.25. Damping Ratio Variation of 0.5-1 mm Loose Silica Gel with Shear Strain.....	67
4.26. Damping Ratio Variation of 0.5-1 mm Dense Silica Gel with Shear Strain	68
4.27. Damping Ratio Variation of 1-3 mm Loose Silica Gel with Shear Strain.....	68
4.28. Damping Ratio Variation of 1-3 mm Dense Silica Gel with Shear Strain	69

4.29. Damping Ratio Variation of 2-5 mm Loose Silica Gel with Shear Strain	69
4.30. Damping Ratio Variation of 2-5 mm Dense Silica Gel with Shear Strain	70
4.31. Damping Ratio versus Shear Strain for a 0.5-5 mm Loose Silica Gel Sample under Confining Pressures	71
5.1. Camera Calibration Check Board with 2.5 mm Spacing Grids	75
5.2. Corner Points Extraction and Coordinate Systems in the Object Plane and Image Plane	75
5.3. Residual Error for X from the Neural Network Model	77
5.4. Residual Error for Y from the Neural Network Model	77
5.5. Residual Error for X from the Linear Calibration Model	78
5.6. Residual Error for Y from the Linear Calibration Model	79
5.7. Residual Error for X from the Second-Order Polynomial Model.....	79
5.8. Residual Error for Y from the Second-Order Polynomial Model	80
5.9. The Relative Position of Different Calibration Planes to the Image Plane.....	81
5.10. Experiment Setup for the Rectangular Footing	83
5.11. The Deformation Vector Field of Sand under the Rectangular Footing (t =6 min, P=0.092 kN).....	83
5.12. The Magnitude Contour of Displacement Vector for Sand under the Rectangular Footing (t =6 min, P=0.092 kN)	84
5.13. The Normal Direction of Flow Line for Sand Particles under the Rectangular Footing (t =6 min, P=0.092 kN).....	85
6.1. The UCIST Shake Table System	93
6.2. Dimensions of the Rigid Wood Block (The toppling angle $\phi=14^\circ$).....	94
6.3. The Shake Table Test Setup for the Rigid-Block and Soil Interaction	95
6.4. Mark Points Setup in the Transparent Soil Model	97
6.5. Displacements vs Time Data from PIV and Tracking for Points A, B, C, D, E, F, and G	97
6.6. Instantaneous Velocity Field of Transparent Soil Mass	102
6.7. The Locations of Points A, B C, and D in the Soil Model	104
6.8. The Displacement History of Point A, B, C, and D.....	104
6.9. The Motion of the Rigid-Block at Different Time under the Input Motion of 2 Hz, 0.25 inch (0.635 cm)	110
6.10. The Motion of the Rigid-Block at Different Time under the Input Motion of 2 Hz, 0.5 inch (1.27 cm)	111

6.11. The Time History of the Rotating Angle α	112
6.12. The Time History of Rotation of a Slender Rigid-Block with B =1 m and H =5 m	113
6.13. Instantaneous Velocity Field of the Testing Model.....	114
6.14. The Locations of Points A1, B1, C1, and D1	115
6.15. Displacement – Time History for Points A1, B1 in both the Vertical Direction and the Horizontal Direction in the Image Space	116
6.16. Displacement – Time History for Points A1, B1 in both the Vertical Direction and the Horizontal Direction in the Real Space.....	117
6.17. Displacement – Time History for Points C1, D1 in both the Vertical Direction and the Horizontal Direction in the Image Space	117
6.18. Displacement – Time History for Points C1, D1 in both the Vertical Direction and the Horizontal Direction in the Real Space.....	118

LIST OF TABLES

Table	Page
3.1. Properties of Potential Solvents	21
3.2. The Refractive Index of the Chemical Solvents-I.....	22
3.3. The Refractive Index of the Chemical Solvents-II	23
3.4. Mixture of Toluene and the Compensating Solvents with Dry Silica Gel	38
3.5. Mixture of Lamp Oil and the Compensating Solvents with Dry Silica Gel	39
3.6. Immersion Test on a Humboldt Membrane.....	42
3.7. The Tensile Test Specimen and Test Description for the Latex Membrane.....	45
4.1. Resonant Column Testing Program.....	54
5.1. Absolute Error for Nine Planes from Three Calibration Algorithms	81
6.1. The Similitude Law for Model Tests in 1 g Gravitational Field.....	89
6.2. Similitude for Model Tests in 1 g Gravitational Field in the Special Case in which $\lambda_\rho = 1$ and $\lambda_\varepsilon = \lambda^{0.5}$	90
6.3. Scaling Relations for Primary Soil Properties	92
6.4. Shake Table Specifications.....	93

1. INTRODUCTION

1.1. MOTIVE OF THE RESEARCH

Interaction between different objects is a ubiquitous phenomenon. Newton's Third Law quantitatively explains it: "For every action, there is an equal and opposite reaction." The interaction between the sun and the earth causes the earth to suspend in the air without falling. Gravity effects are the reflection of this interaction. Without gravity, it would be impossible for human beings to live on the earth. The interaction between soil and a structure is just one example of all the types of interactions that exist. The static interaction between soil and a structure was first investigated by geotechnical engineers because the foundation structure of a building must be built upon the soil. The investigation of this subject led to bearing capacity theory, settlement of foundations, foundation design, slope stability, and retaining structure design. These are all the subjects of classic static soil mechanics. In fact, all the objects are in movement; no object is absolutely still. In this case, static interaction means that the movement of the object is relatively slow. When the movement speed becomes obvious or high, it is usually classified as dynamic interaction. The usually observed launch of a rocket, rowing of a boat, hammer hitting an object, and swimming are all examples of dynamic interaction phenomena.

Dynamic interaction is described by Newton's Second Law: "The acceleration of an object as produced by a net force is directly proportional to the magnitude of the net force, in the same direction as the net force, and inversely proportional to the mass of the object." Dynamic soil-structure interaction can be defined as the interaction between the soil and structure when either one of them is in movement. When the soil is in movement, which is typically due to an earthquake event, the wave from the fault propagates upward to the soil surface and the structure. The motion (movement) of the earth thus leads to the movement of the structure, which in turn reacts back to the soil, changing the motion state of the soil. The soil's motion characteristics also change the natural period of the structure. For example, when the structure is moving due to machine vibration, wind load, impact, or an explosion, the motion of the structure will be transferred to the supporting soil and then will propagate away from the structure. The interaction of the soil and

structure will change the vibration of the structure and cause the movement of the soil. Dynamic soil-structure interaction is a very complicated phenomenon. It integrates dynamic soil mechanics, dynamic structural mechanics, and the theory of wave propagation, where the combined efforts of geotechnical engineers, structural engineers, and earthquake engineers are needed.

Dynamic properties of soil strongly affect the dynamic soil-structure interaction. Dynamic properties of soil are affected by many factors including soil types (clay or sand), the damping effect, the over consolidation effect, water table location, stiffness of the soil, shear modulus of the soil, loose or dense status of the sand, liquefaction potential of the soil, and shear strength of the soil. How the wave propagates from the fault location in the soil, as well as the direction, frequency, and amplitude of each different type of wave and its incident direction into the structure, will also affect the soil-structure interaction. The size and type of structure, foundation embedment, vibration mode of the structure, dynamic load acting on the structure, natural period of the structure, and dynamic properties of the structural material will also influence the soil-structure interaction. Research on the dynamic soil-structure interaction is important for designing nuclear facilities, buildings, and structures in a seismic zone as well as machine foundations.

The importance of dynamic soil-structure interaction in a seismic zone did not receive the attention of researchers until several big earthquake events occurred. The interaction between the structure and soil were first observed in many earthquake events. During the Arvin – Tehachapi, California earthquake of July 1952, a number of tall, slender, petroleum cracking towers stretched their anchor bolts and rocked back and forth on their foundations. After an earthquake in Alaska in March 1964, the oil tanks were found lifted off from the soil. In a 1985 earthquake in Mexico City, seismic capacity failure of the foundation was found. Recently, Hyogoken – Nanbu earthquake, in January 1995, a slender building did not suffer any structural damage, even though it was located in the heavily damaged area of Kobe (Hayashi, 1996, 1999). However, many highway bridges were destroyed due to the rotation and sliding of the bridge abutment. In 1999, an earthquake in Izmit, Turkey, tilting and overturning of the buildings was observed. In order to properly design buildings and structures and to avoid damage caused by

earthquakes, it is important to study the interaction mode between soil and a structure, the movement pattern of the soil surrounding the structure, the movement mode of the structure, and the parameters effects (the embedment, structural dimensions, and the type of structure) on the soil-structure interaction.

1.2. PROBLEM STATEMENT

The interaction mode between soil and a structure usually consists of rocking, sliding, or combined rocking and sliding. It depends on the types and dimensions of the structure, the frequency and amplitude of different input excitations, and the stiffness and damping characteristics of the soil. Currently, it is still a mystery regarding how a structure will behave under earthquake excitation, how the soil will behave under a seismic event, how the failure will happen, and how the interaction mode will react under a seismic event. Because the soil is opaque, the commonly observed failure pattern usually obtained from the soil surface, it is difficult to know what is really happening inside the soil mass. Traditional experimental work has usually been carried out to get information from several discrete points on the structure and inside the soil mass using LVDTs, accelerometers, and strain gauges. The full-field information is impossible to obtain. Without the full-field information, it is difficult to completely understand the dynamic interaction behavior between soil and a structure.

In this study, transparent soil with a low viscosity pore fluid has been developed to visualize the soil-structure interaction. The Particle Image Velocimetry (PIV) technique has been applied to investigate the full-field deformation of the dynamic soil-structure interaction. Using transparent soil, it is able to observe what is happening inside the soil mass during a shaking event. Transparent soil combined with the PIV technique proves to be a powerful tool for research on the dynamic soil-structure interaction. This study also clearly revealed how the rigid block would interact with the transparent soil under the simulated input sinusoidal wave motion.

1.3. DISSERTATION OUTLINE

The research has been carried out to achieve the following goals:

- 1) Development of a low viscosity pore fluid to manufacture the transparent soil.

- 2) Investigation of the dynamic properties of transparent soil.
- 3) Development of a simple camera calibration algorithm for PIV.
- 4) Application of PIV to study the deformation pattern of the soil during a seismic event.
- 5) Investigation of the rigid block-soil interaction using a shake table test.

In this dissertation, Section 1 briefly introduces the scope of this research. Section 2 presents a literature review on transparent soil, dynamic soil-structure interaction, PIV as well as its application in geotechnical engineering, and camera calibration. Section 3 presents the investigation on searching the low viscosity pore fluid for the transparent soil. Section 4 presents the dynamic properties of transparent soil, which is compared to the dynamic properties of sand through literature review and a series of resonant column tests. Section 5 describes a neural network-based camera calibration algorithm for PIV. Section 6 presents testing data for a series of shake table tests on the rigid-block model resting on the transparent soil mass through PIV analysis. Conclusions and future research work are summarized in Section 7.

2. LITERATURE REVIEW

2.1. INTRODUCTION

This research touches several different subjects including transparent soil, pore fluid, dynamic properties of transparent soil, dynamic soil-structure interaction, and PIV. The current status of these subjects is briefly reviewed and summarized in this section.

2.2. TRANSPARENT SOIL

Transparent soil is a mixture of pore fluid and granular silica gel or amorphous silica gel. It is transparent because pore fluid has the same refractive index as silica gel. Silica gel is a porous, amorphous form of silica (SiO_2) that closely resembles natural sands. It is composed of a vast network of interconnected microscopic pores. The diameter of pores varies between 5\AA and 300\AA . Silica gel has either a granular or beaded shape. It is made by partially dehydrating metasilicic acid and is commonly used as a moisture absorbent, catalyst, and in purifying different substances. Silica gels are able to absorb pore fluids and thus drive air out of the internal pores (Mannheimer and Oswald, 1993). Therefore, an appropriate pore fluid is critical for manufacturing the transparent soils with silica gel. Iskander (1994) discovered two matching pore fluids. The first pore fluid is a 50:50 blend by weight of a colorless mineral oil (Drakeol 35) and normal-paraffinic solvent (Norpar 12). Its refractive index is 1.447 at 24°C , and its viscosity is 5.0 cP at 24°C . The density of the pore fluid is 0.804 g/cm^3 . The second matching pore fluid is a mixture of calcium bromide and water. The refractive index and viscosity of the mixture is 1.448 and 3.6 cP , respectively, at 25°C . The dry unit weight of the silica gel is $6 - 9\text{ kN/m}^3$. The saturated unit weight of the silica gel is $11-14\text{ kN/m}^3$ depending on the pore fluids used in manufacturing the transparent soil. According to Mannheimer and Oswald (1993), silica gel specimens usually have a large apparent total void ratio e due to the internal pores of the transparent aggregates. The interaggregate void ratio, e_i , is usually used to describe the effective void space between silica gel aggregates. The interaggregate void ratio, e_i , can be defined as shown in Equation (2.1):

$$e_i = \frac{V_v - V_{vi}}{V_s + V_{vi}} = \frac{e - a\gamma_s}{1 + a\gamma_s}$$

(2.1)

where V_v = the total volume of voids, V_{vi} = the volume of voids inside solid aggregates, V_s = the volume of solids, γ_s = the unit weight of solids, and a = the adsorption factor (the volume of fluid absorbed by a unit mass of the dry silica gel).

Welker et al. (1999) adopted transparent soil to investigate the PVD (Plastic Vertical Drain) flow pattern problem. They found difficulties in using the transparent soil mentioned above such as incompatibilities with the latex membranes, high viscosity of the pore fluid, degradation in the transparency for the large samples, special sealing requirements for the experiment, and costly expense. These areas need further investigation and examination.

In order to correctly model the behavior of natural soil, the selected pore fluids will have the following properties: (1) kinematic viscosity identical to or close to that of water; (2) surface tension close to that of water; (3) incompressibility; (4) affordability; and (5) low or no interaction with silica gel, membranes, and the model container. Further research work needs to be carried out to search the appropriate pore fluid for manufacturing the transparent soil.

2.3. MECHANICAL PROPERTIES OF TRANSPARENT SOIL

Iskander et al. (2003) conducted a series of laboratory tests on two types of silica gels to investigate their geotechnical properties. The first type of silica gel tested is angular shaped silica with a size of 0.5-1.5 mm; the second type of silica gel is round shaped silica with a grain size of 2-5 mm in grain size. His research findings are summarized as follows:

- (1) The silica gel has shown a consistent stress strain behavior with that of sand. The peak shear stress was reached at a higher strain level compared to the behavior of sand.
- (2) The angle of internal friction for silica gel is in the range of 29-42° for the

angular shaped silica gel and $34-50^\circ$ from both the direct shear tests and the triaxial tests.

(3) The typical values of elastic modulus (E_{50} , the elastic modulus at 50% of the failure strain) for the angular shaped silica gel is 15-22 Mpa for the loose sample and 26-32 Mpa for the dense sample. The typical values of elastic modulus for the round shaped silica gel is 24-52 Mpa for the loose sample and 36-84 Mpa for the dense sample.

(4) The hydraulic conductivity of silica gel was tested using the flexible wall permeability tests. The hydraulic conductivity is 1.5×10^{-4} cm/sec for the angular shaped silica gel and 7×10^{-3} cm/sec for the round shaped silica gel.

(5) The silica gel shows a much more compressible behavior to that of sand.

In a summary, the silica gel has a similar static behavior compared to that of sand.

It has been searched thoroughly through the literature; however, the author did not find any information currently available for the dynamic properties of the transparent soil. Therefore, the dynamic properties of silica gel are investigated in the research through a series of resonant column tests.

2.4. DYNAMIC SOIL-STRUCTURE INTERACTION

It is widely recognized the importance of dynamic soil-structure interaction in the design of structures in the seismic zone. Dynamic soil-structure interaction was influenced by many factors such as soil properties, structure type, and excitation wave. Dynamic soil-structure interaction is a very complicated phenomenon. The literature review in this section only focuses on the case of a rigid block on the deformable foundation.

Muto et al. (1960) performed a series of small scale shake model test to study the overturning vibration of slender elastic and rigid structures on rigid, hard, and elastic foundation. The flexible structure is modeled as mass supported on a flexible bar frame and the rigid structure is simply reinforcing the flexible structures with wire stays. The rigid foundation is modeled as wood base sheet, hard foundation as hard rubber sheet, and elastic foundation as soft rubber. And a theoretical analysis also performed on the rigid block and rigid foundation case.

Psycharis (1982) studied the dynamics of the rigid block on the deformable foundation using two spring foundation model and Winkler foundation model. He derived the complete equations for describing the behavior of the structure when the uplift of the foundation was allowed.

Following Psycharis' work, Koh and Spanos (1986) studied the harmonic rocking of rigid block on flexible foundation. In their study, a rigid block is resting on a foundation of independent springs and dashpots. Uplifting of the block base from the foundation is allowed when the springs are in tension. Two piecewise equations are derived to describe the rocking motion, and they are coupled and nonlinear. When the foundation moves horizontally due to a harmonic acceleration, an approximate analytical solution is used to predict the rocking amplitude of the block. They showed that relatively large rocking amplitudes, compared to the model without uplift can happen when excitation frequencies is below the natural rocking frequency of the block. They also developed an approximate method for predicting the maximum tilt-angle under horizontal excitation by relying on the linear seismic response spectra. The results were in reasonable agreement with data obtained from numerical integration of the exact equation of motion.

Gazetas et al. (2003) investigated the case of rocking and uplifting of a rigid-block type of structure in contact with a visco-elastic horizontally-oscillating ground and the case of a structure supported on soft soil which may undergo large plastic deformations and bearing capacity failure during rocking and uplifting of the structure, under horizontal excitation. The dynamic analysis was carried out by Abaqus finite element program. They found that the block can sustain the rocking motion safely even for values of moment much higher than the static overturning moment. Decreasing the elastic modulus of the soil will lead to the higher values of the maximum rocking angle without lifting, which can reach 2.5 times of rigid soil value. However, when the soil is very soft, the maximum rocking angle without lifting will increase instead. They also found that the overall size of the block affects strongly its rotation; the smaller, the bigger the rocking angle. This observation also occurred for the rigid-block rigid foundation case which is first discovered by Housner(1963).

A limited research has been conducted on the rigid block resting on a deformable foundation case, the following conclusions can be obtained from these limited research:

- 1) The behavior of a rigid block on a flexible foundation is different from that of a rigid block on a rigid foundation.
- 2) The damping effect of a deformable foundation tends to decrease the rocking frequency of a block.
- 3) The flexibility of the soil foundation does not have a monotonic effect on the maximum rocking angle of a block.
- 4) The rocking of a rigid block may lead to the yielding or even bearing capacity failure of the soil.

It is thus important to conduct further research to study the dynamic soil-structure interaction of a rigid block on the flexible foundation.

2.5. PARTICLE IMAGE VELOCIMETRY (PIV)

Particle Image Velocimetry (PIV) is a measurement technique that was originally developed in the field of experimental fluid mechanics to recover instantaneous velocity fields from photographs of seeded flow (Adrian, 1991). Figure 2.1 shows a PIV system for measuring the flow velocity. It consists of a laser light sheet (for illumination), water flow with seeding particles, an image recording system (camera), and an image data processing system. This technique has recently been applied to geotechnical modeling (White et al., 2002, 2003) and it is sometimes referred to as digital image correlation (DIC)(Sadek et al., 2003; Rechenmacher and Finno, 2004), or block-matching (Michalowski and Shi, 2002).

The principles behind PIV are the image pattern matching technique. Assume two images (I_1 and I_2) were obtained, and these two images were divided into smaller regions (sub-windows, interrogation-windows, or interrogation-regions). Then, each sub-window in the image, I_1 , was compared with the corresponding sub-window in the image, I_2 . The cross-correlation between the two sub-windows is defined as

$$R(s,t) = \sum_{m=0}^{M-1} \sum_{n=0}^{N-1} I_1^{i,j}(m,n) \cdot I_2^{i,j}(m-s,n-t) \quad (2.2)$$

where $I_1^{i,j}$ is the sub-window number (i, j) in the first image; and $I_2^{i,j}$ is the sub-window number (i, j) in the second image. When this expression reaches its peak value, the two sub-windows will most likely match each other. The sub-window has moved s and t units in i and j directions, respectively.

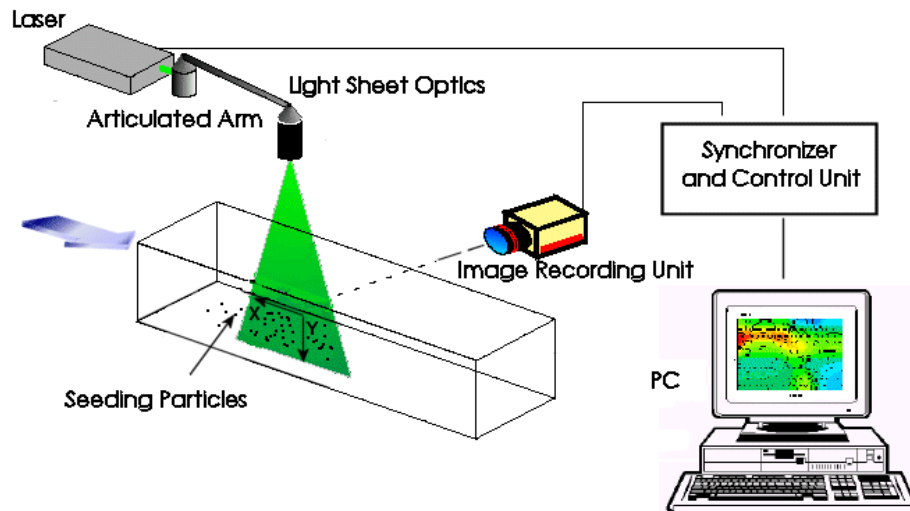


Figure 2.1. A Particle Image Velocimetry System to Measure the Flow Velocity (<http://gedenoe.de.unifi.it/attivita%20piv.html>)

PIV has seen a steady increase and acceptance in a variety of engineering disciplines. It has been applied to aerodynamics, liquid flow, multiphase flow, combustion, supersonic flow, and hypersonic flow. Sousa (2002) studied the mean turbulent flow structure around a cube mounted on the surface of an open-surface water channel.

PIV has also found its application in fluid-structure interaction and impact wave study. Figure 2.2 shows the velocity vector field of a high-speed granular land slide impact into the water by the PIV technique (Fritz, 2000).

PIV has also been applied to study the granular flow phenomena. Lueptow et al. (2000) adapted PIV to measure particle displacement and velocity fields in granular flows. "Seeding" is achieved by using light and dark particles. Figure 2.3 shows the schematic setup of his test. Figure 2.4 is the image captured after 45 s oscillation. Figure 2.5 (a), (b) show the vector fields from the PIV analysis.

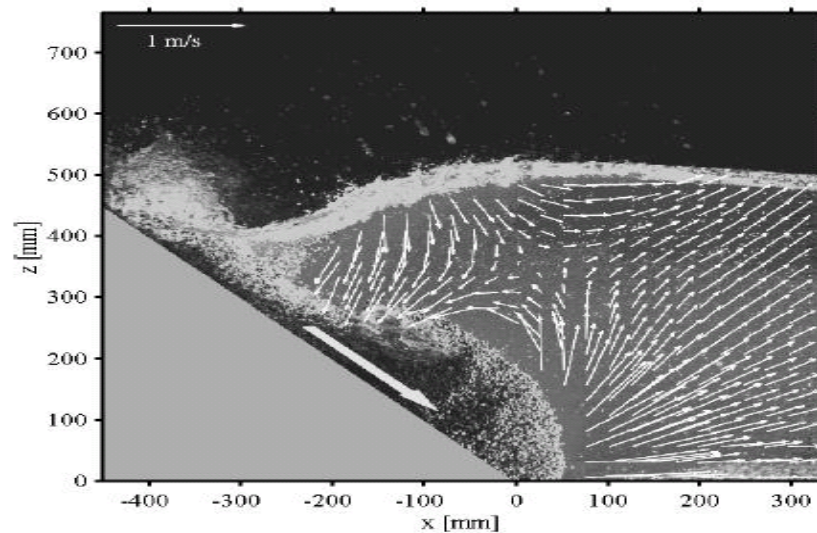


Figure 2.2. Velocity Vector Field of a High-Speed Land Impact into the Water (Fritz, 2000)

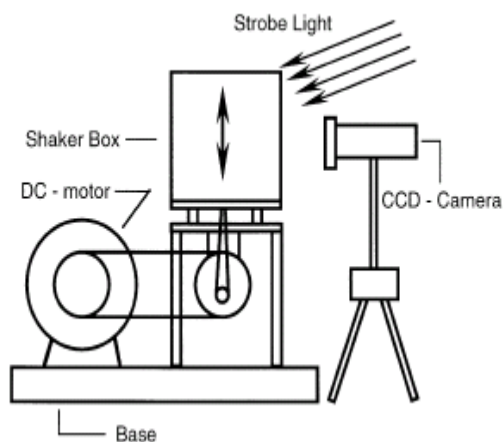


Figure 2.3. Schematic of Vertically Oscillating Box and PIV Setup (Lueptow, 2000)

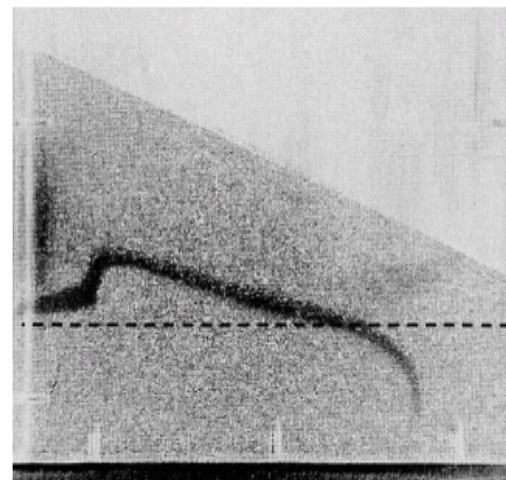


Figure 2.4. Image Captured after 45 s of Vertical Oscillation. The Dark Curve is a Layer of Yellow Beads Initially Located at the Horizontal Dashed line (Lueptow, 2000)

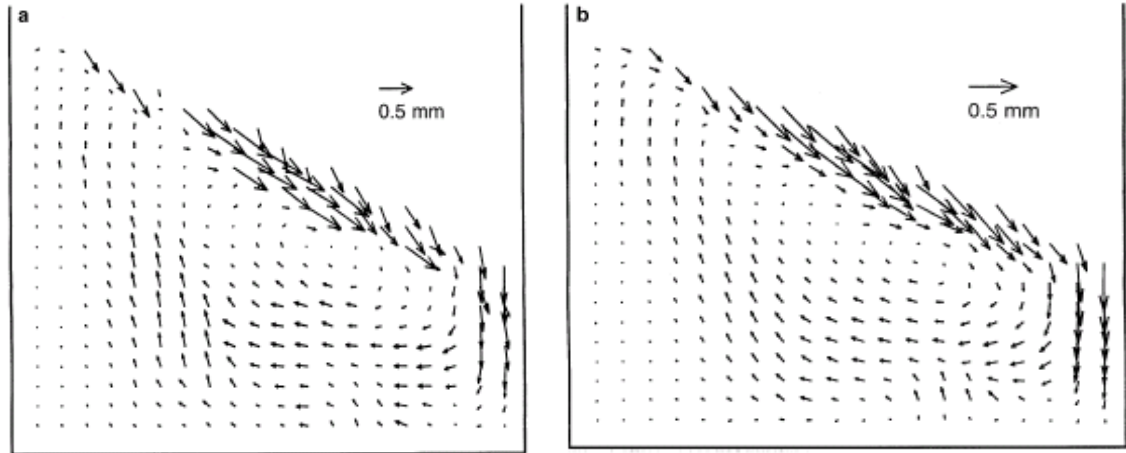


Figure 2.5. Displacement Vectors Showing a Convective Roll (a) Single Realization of Displacement Vectors; (b) Ensemble Average of Eight Realization of Displacement Vectors (Lueptow, et al., 2000)

2.6. PIV APPLICATION IN GEOTECHNICAL ENGINEERING RESEARCH

Guler, et al. (1999) measured the particle movement in granular soils using image analysis. In their study, the image of Ottawa sand at the interface with the steel plate was acquired by a microscope camera. Then the images were analyzed by block matching method and individual particles tracking method. Figure 2.6 shows the image of sand particles in contact with a steel plate. Figure 2.7 shows the displacement vector of sand particles from the image analysis.

White, et al. (2003) applied the PIV technique to investigate the installation of a displacement pile. Figure 2.8 shows the displacement field around the pile from the PIV analysis. Take (2003) observed the onset of progressive failure under moisture cycles in a clay embankment model.

Sadek, et al. (2003) applied the DIC (digital image correlation which is based on the same image analysis algorithm with PIV) in measuring the spatial deformation throughout a transparent soil model. His setup for the experiment is illustrated in Figure 2.9. The setup consists of a transparent soil model, a laser source, a sheet generator lens, and a digital camera. The model container is made of Plexiglas and was filled with fine

silica gel (grain size 0.5-1.5 mm). A rigid footing with a footprint of 50 mm x 50 mm (2 in x 2 in) was mounted on the surface of the silica gel. The footing was pushed into the model using a loading system. The total displacement recorded by the LVDT was 2.41 mm (0.095 in.). Figure 2.10 shows the displacement field from the DIC analysis.

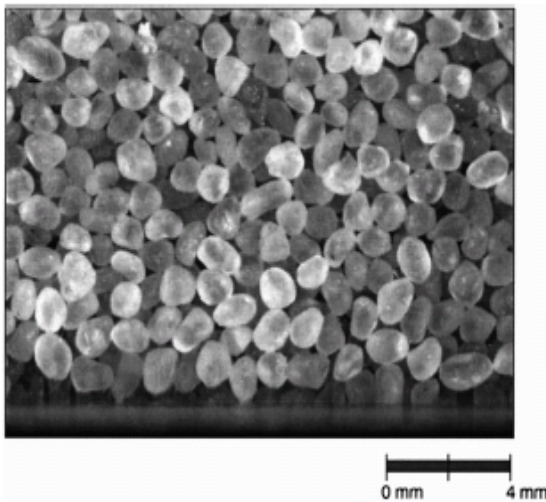


Figure 2.6. The Image of Ottawa Sand in Contact with the Steel Plate

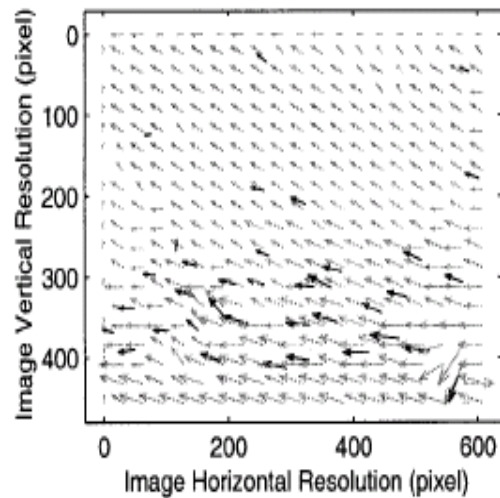


Figure 2.7. The Displacement Vectors from the Image Analysis (Guler et al., 1999)

Rechenmacher and Finno (2004) used DIC to quantify the localized displacements on dense sands in plane strain compression experiments. Figure 2.11 showed the typical digital image of a sand sample. Figure 2.12 shows the displacement field of the sand subject to compression.

White, et al. (2005) applied this technique to study the instantaneous velocity field at failure of a skirted strip foundation under an eccentric vertical load in the centrifuge test. Figure 2.13 showed the physical model of the problem. Figure 2.14 showed the velocity field of the skirted foundation subjected to the eccentric load.

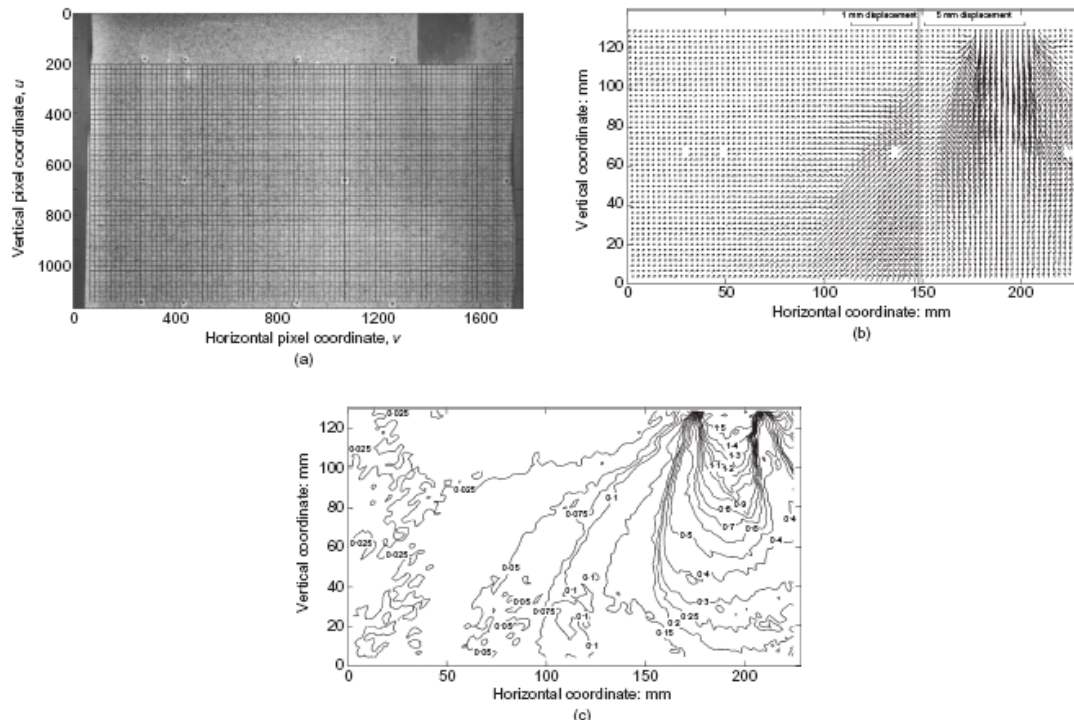


Figure 2.8. Displacement Field around Plane Strain Displacement in Sand: (a) a Mesh of PIV Patches; (b) Displacement Vector Field; (c) Magnitude of the Displacement Vectors (White, 2002)

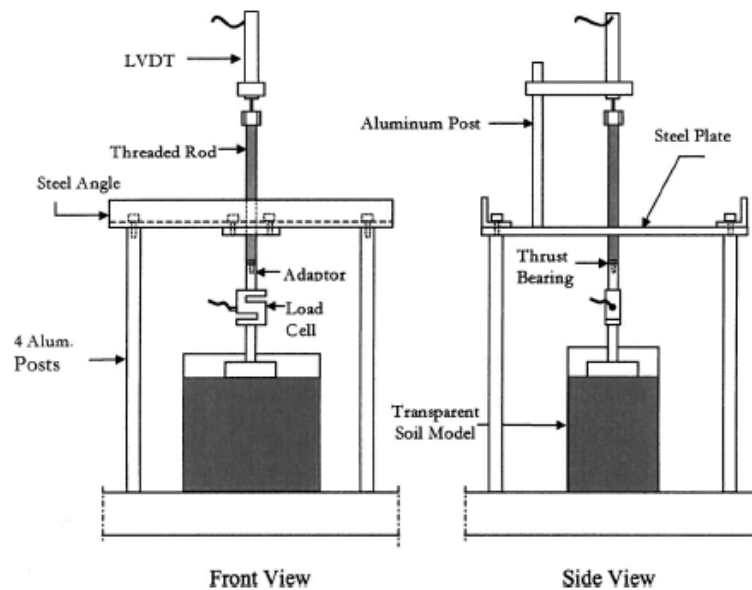


Figure 2.9. The Schematic Diagram of the Experimental Setup Used for Applying Footing Displacements on the Transparent Synthetic Soil Model (Sadek, et al., 2003)

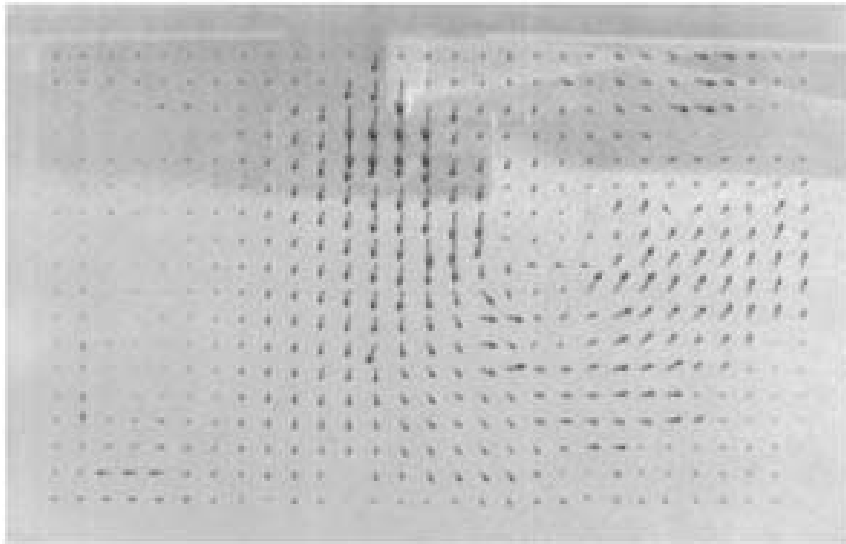


Figure 2.10. DIC Analysis Results: the Arrows Indicate Spatial Displacements in Transparent Soil Slice (Sadek et al., 2003)

The application of the PIV technique in geotechnical engineering does not need the seeding particles. Soils such as sands have their own texture, and they will have different image density profile on the image sensor. Clay can be covered with powder to provide a specific texture in order to be identified. However, the observed soil behavior was restricted only to the soil surface boundary.

The reviewed researchers (White, 2002; White, et al., 2005; Take, 2003; Sadek, et al., 2003; Rechenmacher & Finno, 2004) used the PIV technique in the various geotechnical problems under static loading conditions. This is due to the limitation of the camera and laser power used in their research. Most of the researchers used the still digital camera with a Megapixel resolution. The camera can not take the image of the soil deformation quick enough to capture the real motion of the soil particles in a seismic event. With the coming of high-speed cameras, this limitation can be solved. Some high-end high-speed cameras now can take up to tens thousands of images per second. The camera with high frame rate made possible the visualization of the high speed motion in soil particle. In the current research, PIV technique combined with a high speed digital camera was applied to capture the dynamic motion of soil particles inside of a transparent soil mass.

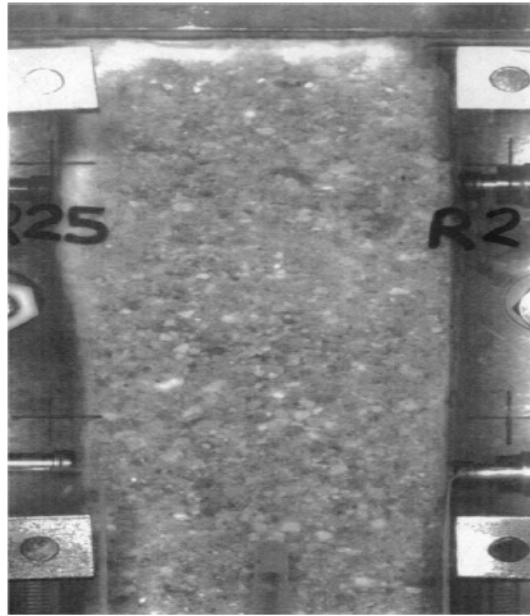


Figure 2.11. Typical Digital Image of Sand Sample Taken During a Biaxial Test (Renchenmacher and Finno, 2004)

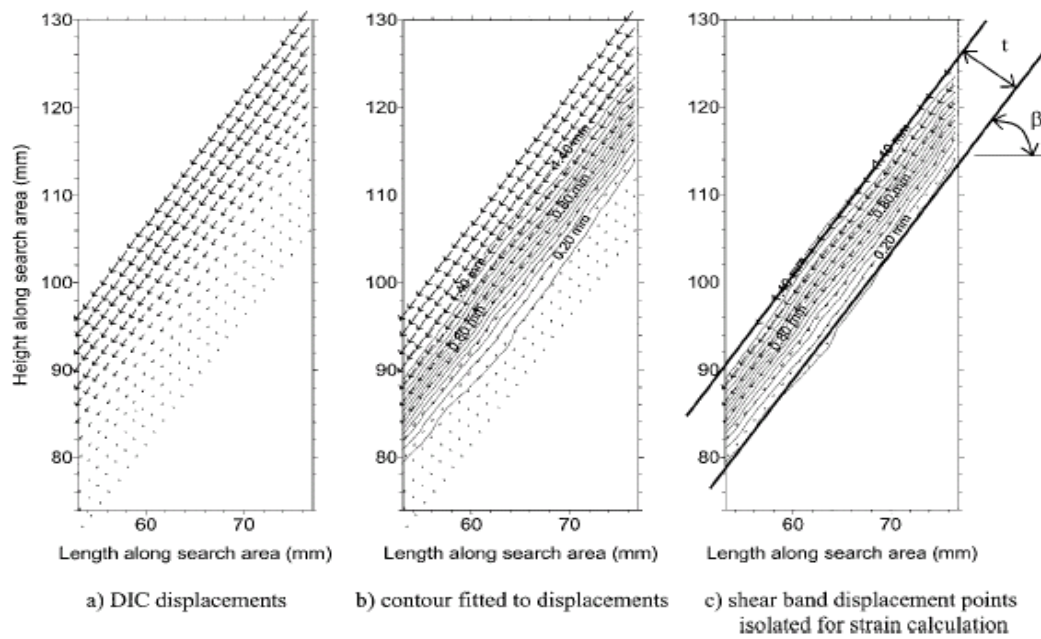


Figure 2.12. DIC-Measured Displacements Surrounding a Persistent Shear Band (Renchenmacher and Finno, 2004)

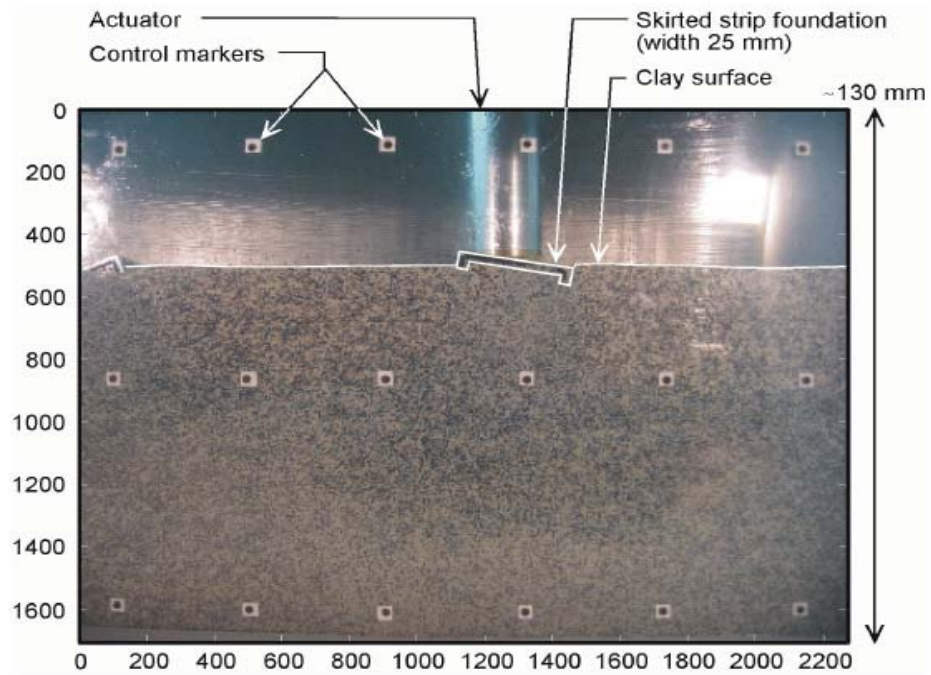


Figure 2.13. Example Image from a Plane Strain Foundation Test (axes in pixels) (White, et al., 2005)

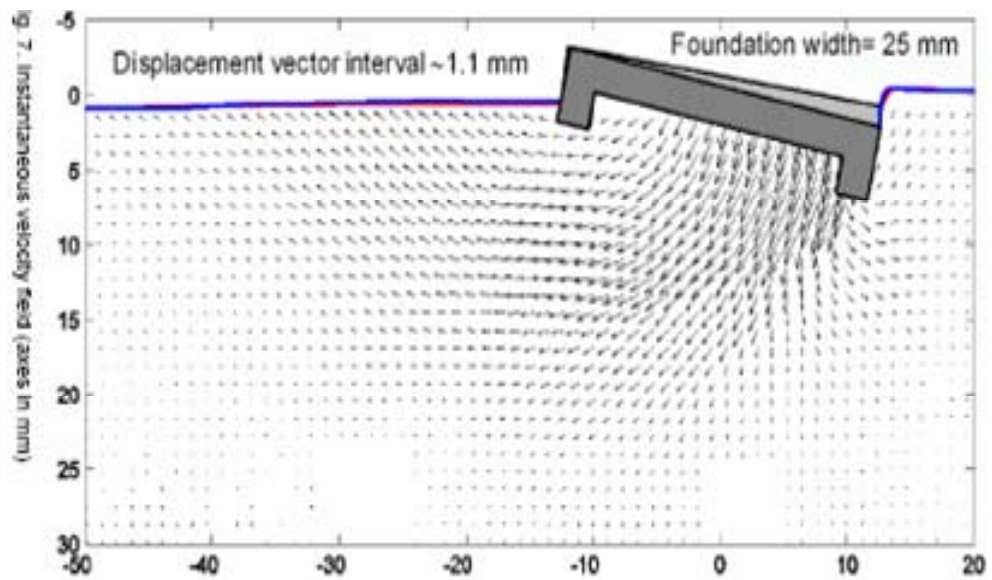


Figure 2.14. Instantaneous Velocity Field of the Skirted Strip Foundation Subject to the Eccentric Load (White et al., 2005)

2.7. CAMERA CALIBRATION FOR PIV

The accuracy of the image based measurement system depends on the resolution of the image-acquiring system and calibration of the system to handle various errors. Camera calibration is an important component of the system. Calibration from the measurement point of view is to find a point $P(X,Y)$ in the object plane coordinate system through its corresponding point $p(u,v)$ in the image plane coordinate system, as illustrated in Figure 2.15. The data obtained from PIV analysis are in the image space. The deformation data obtained under the image space coordinates must be converted into object space coordinates. The image space coordinates is usually in pixels. Several methods for geometric camera calibration are presented in the literature. The first simple model is through the pin-hole camera model, which is assumed that there is a linear relationship between the object points and its image points. However, since the camera distorts the iamge, and the object is commonly behind Plexiglass, a simple relationship between the object points and the image points does not exist. Paikowsky and Xi (2000) used a polynomial function to fit the points $P(X,Y)$ in the object plane to their image points $p(u,v)$ in the image plane. The absolute error can reach 0.4 mm. The classical approach that first came from the field of photogrammetry solves the problem by finding the minimum value of a nonlinear error function (Slama, 1980). This method is slow and requires a lot of computation effort. Closed-form solutions have been also suggested by Abdel-Aziz et al. (1971), Tsai (1987), and Melen (1994). However, these methods are based on certain simplification in the camera model, and therefore, they do not provide as good results as nonlinear minimization. Melen (1994) and Weng et al. (1992) also proposed calibration procedures where both nonlinear minimization and a closed form solution are used. In these two-step methods, the initial parameter values are computed linearly and the final values are obtained with nonlinear minimization. Heikkil & Silven (1997) proposed a four-step camera calibration procure with implicit image correction using 14 parameters. This four-step method is an extension of the two-step calibration methods. There is additional step to compensate for distortion caused by circular features, and a step for correcting the distorted image coordinates.

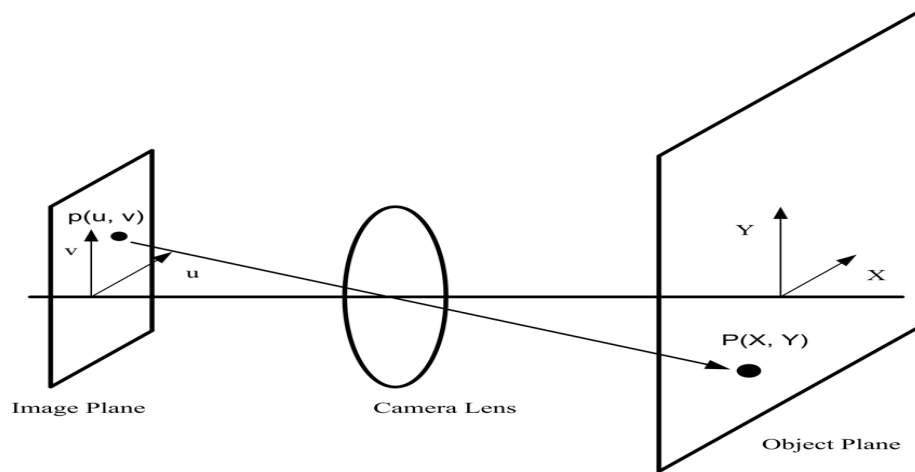


Figure 2.15. The Illustration of Camera Calibration Concept

White et al. (2003) extended the 14-parameter model of Heikkila and Silven (1997) to perform the calibration task. This method works pretty well for the camera calibration taking into account all the possible errors. The calibration control points were obtained through multiple-threshold centroiding. This method still requires a lot of computational effort.

3. LOW VISCOSITY PORE FLUID FOR TRANSPARENT SOIL

3.1. INTRODUCTION

As reviewed from the literature, transparent soil is a mixture of pore fluid and granular silica gel or amorphous silica gel. It is transparent because the pore fluid has the same refractive index as the silica gel. Welker et al. (1999) adopted transparent soil to investigate the PVD (Plastic Vertical Drain) flow pattern problem. They found difficulties in using the transparent soil mentioned above such as the interaction of the pore fluid and the membranes, high viscosity of the pore fluid, degradation in the transparency for the large samples, special sealing requirements for the experiment, and costly expense. These areas need further investigation and examination.

In order to correctly model behavior of natural soil, the selected pore fluids will have the following properties: (1) kinematic viscosity identical to or close to that of water; (2) surface tension close to that of water; (3) incompressibility; (4) affordability; and (5) low or no interaction with silica gel, membranes, and the model container. In this research, 12 types of chemical fluids were selected and tested in order to identify the appropriate pore fluids to make the transparent soils. Table 3.1 lists their basic properties. Toluene, Lamp Oil, and Pyridine were chosen as the base pore fluids because their refractive index is higher than 1.448 (the refractive index of silica gel from Iskander's work). Then, another type of chemical solvent was added to it to achieve the best transparency effect with the silica gel. In order to understand the basic properties of the chemical solvents investigated, first their viscosity and refractive index were studied under different temperatures.

3.2. TEMPERATURE VARIATION OF REFRACTIVE INDEX AND VISCOSITY OF SOLVENTS

It is well known that the refractive index and viscosity of fluid changes with a change of temperature. The first task of this research was to identify the refractive index-temperature relationship and viscosity-temperature relationship for all the chemical solvents tested. The testing device adopted for measuring the refractive index was an AR200 Digital Handheld Refractometer as shown in Figure 3.1. It can measure a wide refractive index range from 1.3300 to 1.5600, and it is accurate to $\pm 0.0001 nD$. All the

solvents were put into a temperature chamber. The refractive indexes of all the solvents were measured by the refractometer at six different temperatures (10°C, 15°C, 20°C, 25°C, 30°C, and 35°C), which cover the possible range of the operating temperature. The test data are presented in Tables 3.2 and 3.3. Tests were repeated after the first measurement in order to assure the repeatability and accuracy of the data.

Table 3.1. Properties of Potential Solvents

Solvent	Viscosity (cP, 25°C)	Kinematic Viscosity (cSt, 25°C)	Density (g/ml, 25°C)	Refractive Index (25°C)	Boiling Point (°C)	Solubility in Water
Acetonitrile	0.34	0.433	0.786	1.341	82	miscible
Cyclohexane	0.90	1.163	0.774	1.423	81	immiscible
Ethyl Acetate	0.43	0.478	0.900	1.370	77	8.3g/100ml (20°C)
n-Heptane	0.40	0.585	0.684	1.385	98	immiscible
Iso-Butanol	4.70	5.860	0.802	1.384	108	moderate
Methyl Ethyl Ketone	0.38	0.472	0.805	1.367	80	soluble
2-Propanol	1.90	2.420	0.785	1.384	82	fully miscible
Pyridine	0.88	0.898	0.980	1.507	115	miscible
Toluene	0.55	0.634	0.867	1.494	110	0.053g/ml (20-25°C)
2,2,4-Trime Thylpentane	0.47	0.681	0.690	1.389	99	immiscible
Water	0.89	0.890	1.000	1.333	100	—
Norpar 12	0.57	0.902	0.63	1.4051	189	immiscible
Lamp Oil	1.778	2.1	0.849	1.783	495	immiscible

(Source: <http://www.jtbaker.com/conversion/solventphydata.htm>)



Figure 3.1. The AR200 Digital Handheld Refractometer

Table 3.2. The Refractive Index of the Chemical Solvents-I

Heptane				2,2,4-Trimethylpentane			
$T_1(^{\circ}\text{C})$	nD_1	$T_2(^{\circ}\text{C})$	nD_2	$T_1(^{\circ}\text{C})$	nD_1	$T_2(^{\circ}\text{C})$	nD_2
10.7	1.3913	10.7	1.3938	10.8	1.3963	10.7	1.3963
13.7	1.3909	16.1	1.3909	16.7	1.3936	16.1	1.3938
20.5	1.3876	20.9	1.3893	20.5	1.3916	20.9	1.3915
25.6	1.3864	25.4	1.386	25.6	1.3894	25.3	1.3894
29.9	1.384	30.4	1.3833	29.9	1.387	30.3	1.3872
35	1.3811	35.8	1.3816	35	1.3849	35.8	1.3847
Toluene				Iso-Butanol			
		$T_2(^{\circ}\text{C})$	nD_2	$T_1(^{\circ}\text{C})$	nD_1	$T_2(^{\circ}\text{C})$	nD_2
11.1	1.5	10.8	1.4997	11.1	1.3996	11	1.3999
16.9	1.4972	16.1	1.4957	17	1.3973	16.3	1.3974
20.7	1.4964	21	1.4947	20.8	1.3964	21.1	1.3952
25.6	1.4928	25.3	1.4938	25.7	1.394	25.5	1.3946
30.1	1.4912	30	1.4919	30.2	1.3948	30.2	1.3934
35	1.4879	35.8	1.4859	35	1.3909	35.9	1.3901

Table 3.2. The Refractive Index of the Chemical Solvents-I Cont'

Ethyl Acetate				Methyl Ethyl Ketone			
$T_1(^{\circ}\text{C})$	n_{D_1}	$T_2(^{\circ}\text{C})$	n_{D_2}	$T_1(^{\circ}\text{C})$	n_{D_1}	$T_2(^{\circ}\text{C})$	n_{D_2}
10.7	1.3913	11.1	1.3784	10.7	1.3913	11.1	1.3841
13.7	1.3909	16.3	1.376	13.7	1.3909	16.3	1.3817
20.5	1.3876	21.2	1.3745	20.5	1.3876	21.2	1.3794
25.6	1.3864	25.5	1.3716	25.6	1.3864	25.5	1.3768
29.9	1.384	30.2	1.37	29.9	1.384	30.2	1.375
35	1.3811	36	1.3655	35	1.3811	35.9	1.372

Table 3.3. The Refractive Index of the Chemical Solvents-II

Cyclohexane				2-Propanol			
$T_1(^{\circ}\text{C})$	n_{D_1}	$T_2(^{\circ}\text{C})$	n_{D_2}	$T_1(^{\circ}\text{C})$	n_{D_1}	$T_2(^{\circ}\text{C})$	n_{D_2}
10.9	1.4318	10.7	1.4318	11.1	1.3812	10.8	1.3817
16.7	1.4289	16.1	1.429	16.7	1.3796	16.1	1.3796
20.6	1.4267	20.9	1.4269	20.6	1.3775	21	1.3777
25.6	1.4237	25.3	1.4239	25.6	1.3757	25.3	1.3758
29.9	1.4214	30.2	1.4216	30	1.3733	30.2	1.3739
35	1.4195	35.8	1.4187	35	1.3715	35.8	1.3712
Acetonitrile				Pyridine			
$T_1(^{\circ}\text{C})$	n_{D_1}	$T_2(^{\circ}\text{C})$	n_{D_2}	$T_1(^{\circ}\text{C})$	n_{D_1}	$T_2(^{\circ}\text{C})$	n_{D_2}
11.1	1.35	11	1.3509	11.1	1.5074	11.1	1.5154
17.2	1.3463	16.2	1.3485	17	1.5111	16.3	1.5118
20.8	1.3463	21.1	1.346	20.9	1.5064	21.2	1.507
25.7	1.3441	25.5	1.3439	25.7	1.5067	25.5	1.5065
30.4	1.3399	30.1	1.3422	30.5	1.5038	30.2	1.5044
35	1.3386	35.9	1.3379	35	1.5016	36	1.5004

Table 3.3. The Refractive Index of the Chemical Solvents-II Cont'

Norpar 12				Lamp Oil			
T ₁ (°C)	nD ₁	T ₂ (°C)	nD ₂	T ₁ (°C)	nD ₁	T ₂ (°C)	nD ₂
10.7	1.3913	11.1	1.4231	10.7	1.3913	11.2	1.4424
13.7	1.3909	16.4	1.4208	13.7	1.3909	16.6	1.4400
20.5	1.3876	21.3	1.4187	20.5	1.3876	21.3	1.4371
25.6	1.3864	25.5	1.4168	25.6	1.3864	26.1	1.4358
29.9	1.384	30.2	1.4144	29.9	1.384	30.4	1.4341
35	1.3811	36.1	1.4116	35	1.3811	36.3	1.4316

After the analysis on the tested data, a linear relationship was established between the refractive index and the temperature for each type of solvent as shown in Figures 3.2. to 3.13. The refractive index linearly decreases with an increasing temperature for all the chemical solvents tested.

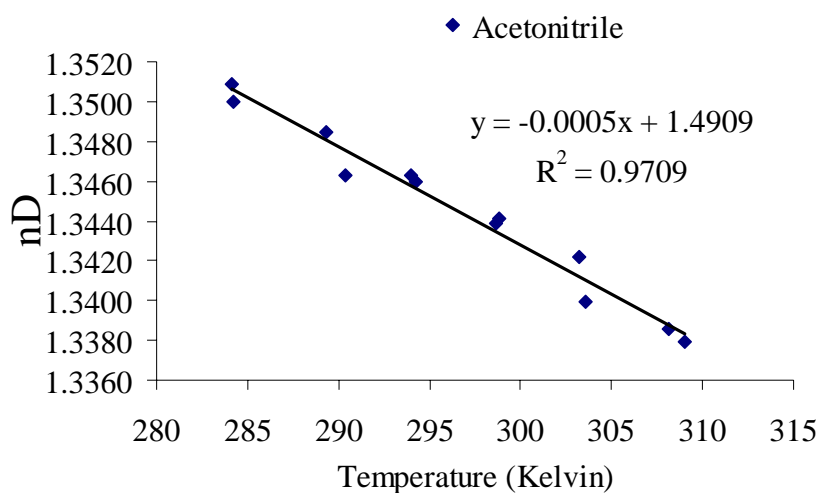


Figure 3.2. The Refractive Index Variation with the Temperature for Acetonitrile

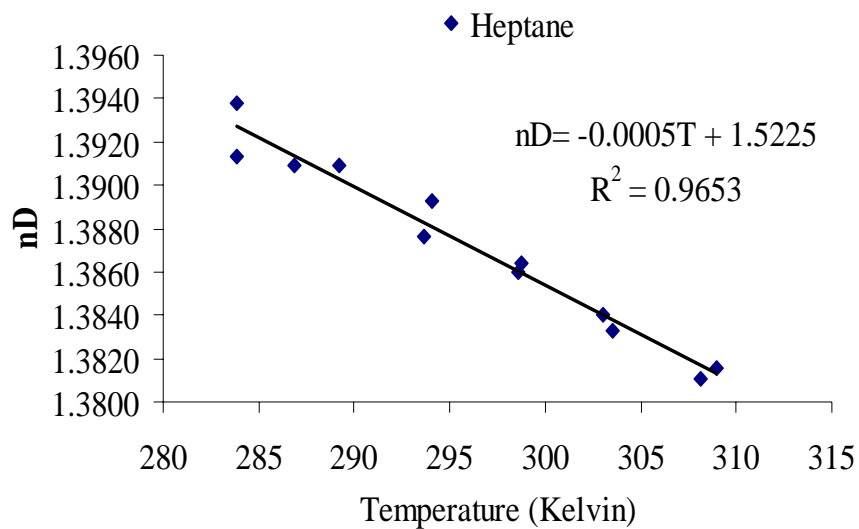


Figure 3.3. The Refractive Index Variation with the Temperature for Heptane

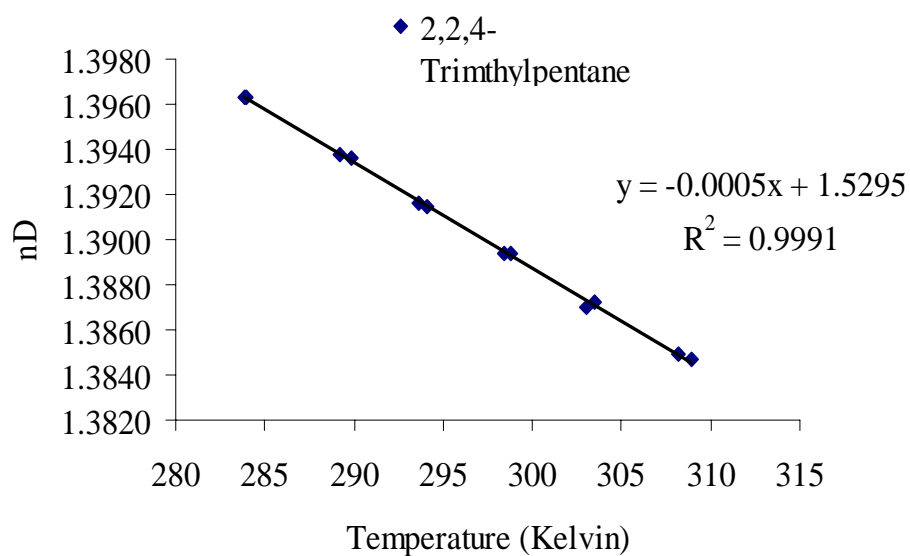


Figure 3.4. The Refractive Index Variation with the Temperature for 2, 2, 4-Trimethylpentane

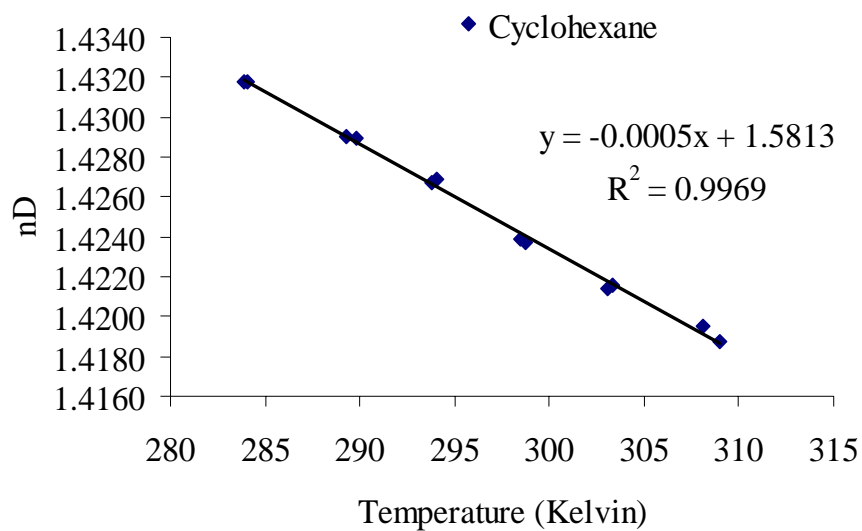


Figure 3.5. The Refractive Index Variation with the Temperature for Cyclohexane

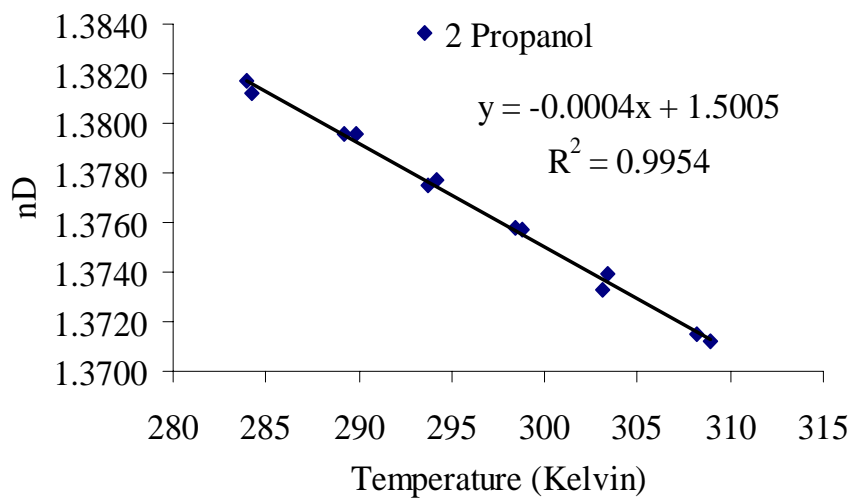


Figure 3.6. The Refractive Index Variation with the Temperature for 2 Propanol

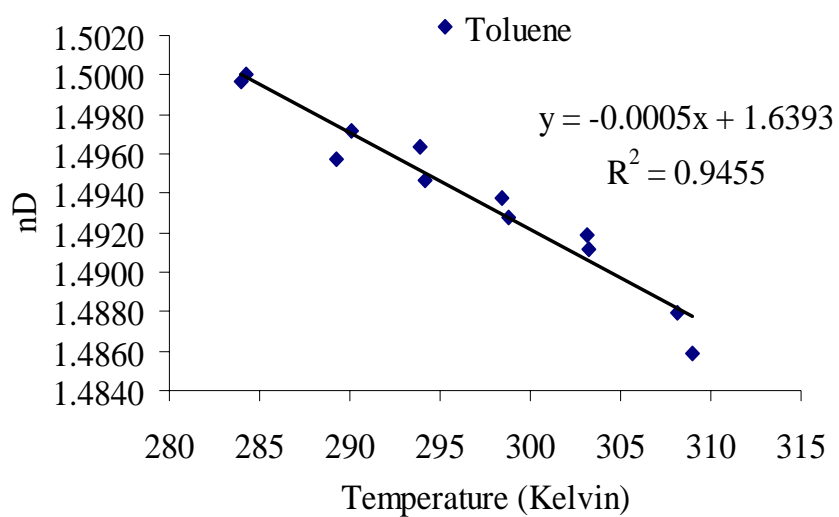


Figure 3.7. The Refractive Index Variation with the Temperature for Toluene

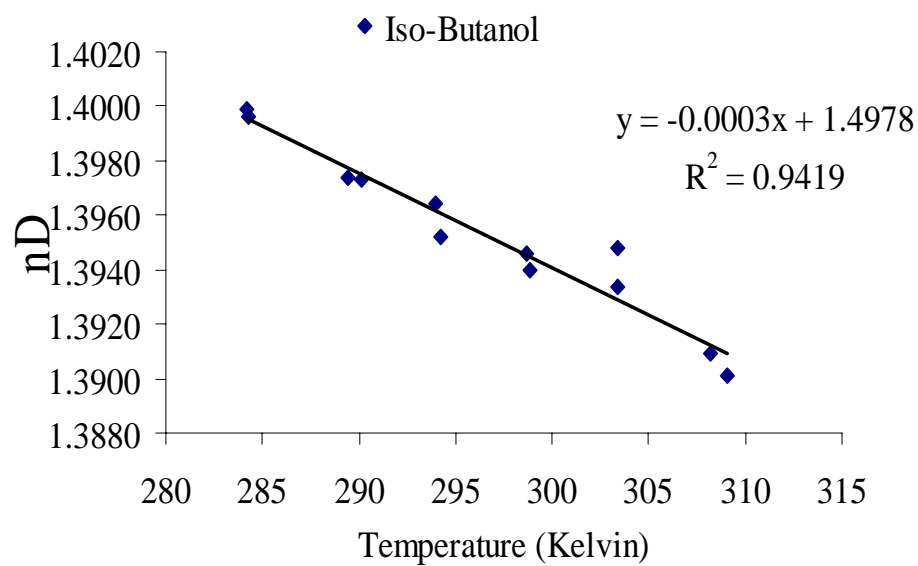


Figure 3.8. The Refractive Index Variation with the Temperature for Iso-Butanol

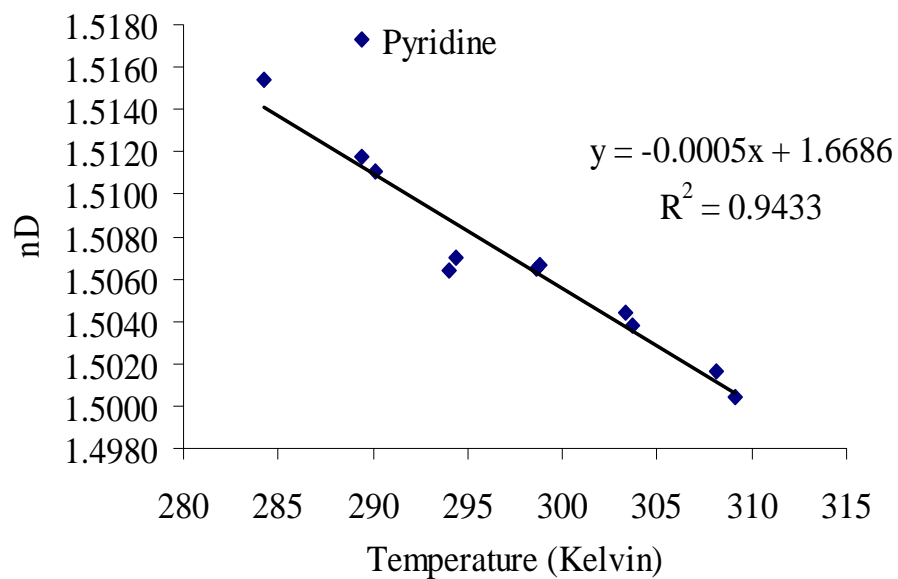


Figure 3.9. The Refractive Index Variation with the Temperature for Pyridine

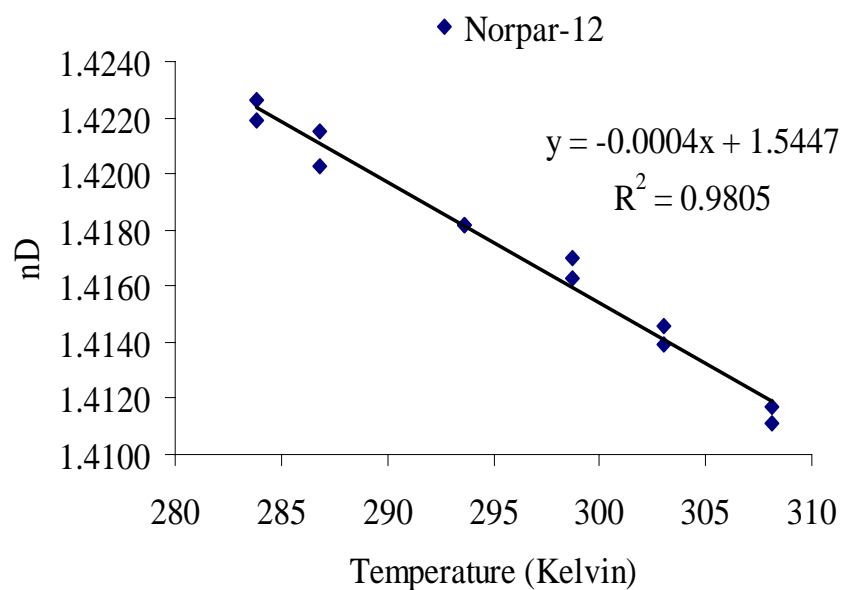


Figure 3.10. The Refractive Index Variation with the Temperature for Norpar 12

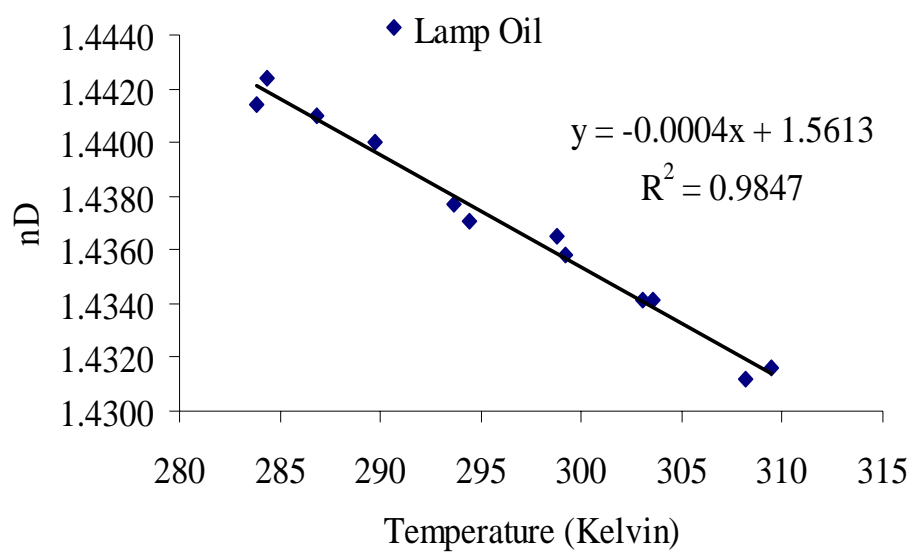


Figure 3.11. The Refractive Index Variation with the Temperature for Lamp Oil

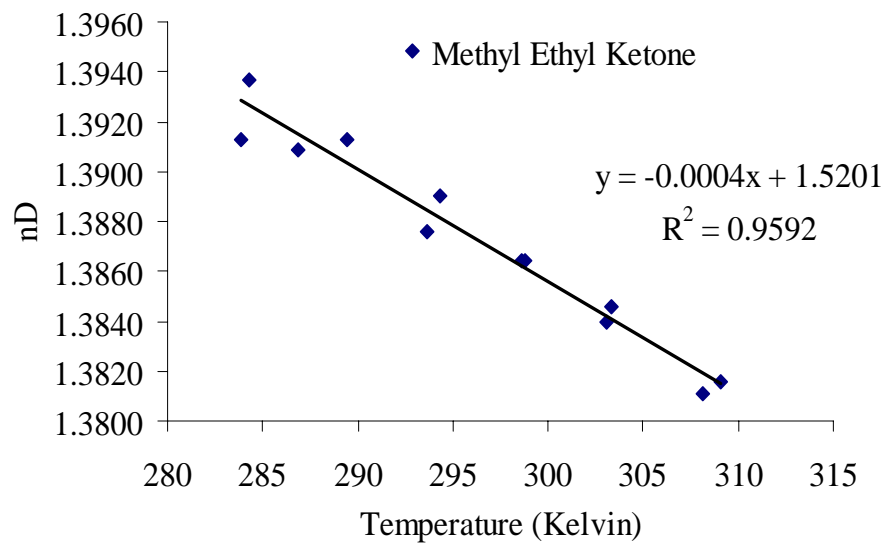


Figure 3.12. The Refractive Index Variation with the Temperature for Methyl Ethyl Ketone

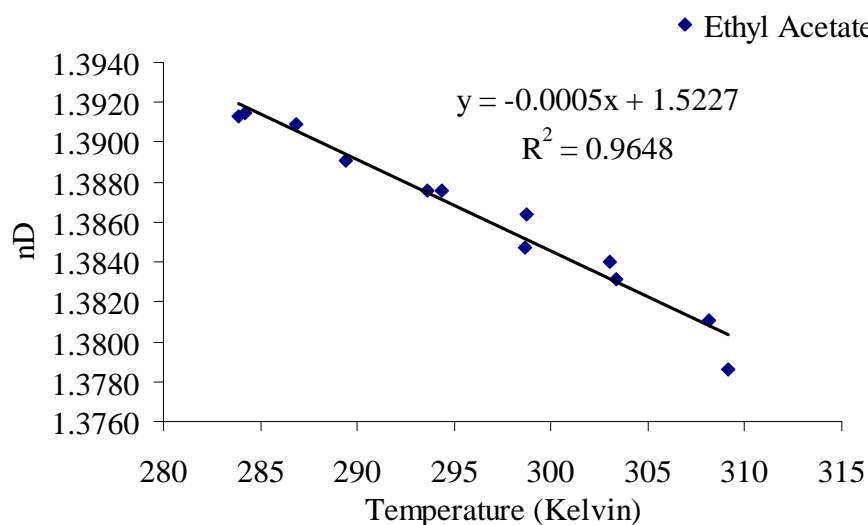


Figure 3.13. The Refractive Index Variation with the Temperature for Ethyl Acetate

The viscosity of the chemical solvents was also measured at different temperatures in order to study their variation characteristics with temperature. The test procedure followed ASTM D 445 – 06, and Cannon-Fenske viscometer tubes were used as shown in Figure 3.14. Two different sizes of tubes (No.25 and No.75) were used in this research for measuring the viscosity of the solvents. Size No. 25 was suitable for the viscosity range from 0.5 to 2 centistokes. Size No.75 was suitable for the viscosity range from 1.6 to 8 centistokes.

The viscosity of each solvent was also measured at six different temperatures (10°C, 15°C, 20°C, 25°C, 30°C, and 35°C). Appendix A shows the test data for the viscosity of all the chemical solvents used. It was also found that the viscosity of all the solvents linearly decreases with the temperature in this range (10°C-35°C). The data are plotted in Figures 3.15 through 3.26.

3.3. DETERMINATION OF THE MATCHING REFRACTIVE INDEX

In order to obtain a pore fluid with the matching refractive index to get the best transparency effects for the silica gel, 4 ml of the base pore fluid (Toluene, Lamp Oil or Pyridine) was first put into the glass tube (Diameter 1.50 cm), and 3~4 grams of dry silica

gel were added into the tube. Then, the compensating pore fluid was added gradually until the best transparency effect was achieved.



Figure 3.14. The Cannon-Fenske Viscometer Tube, No. 25

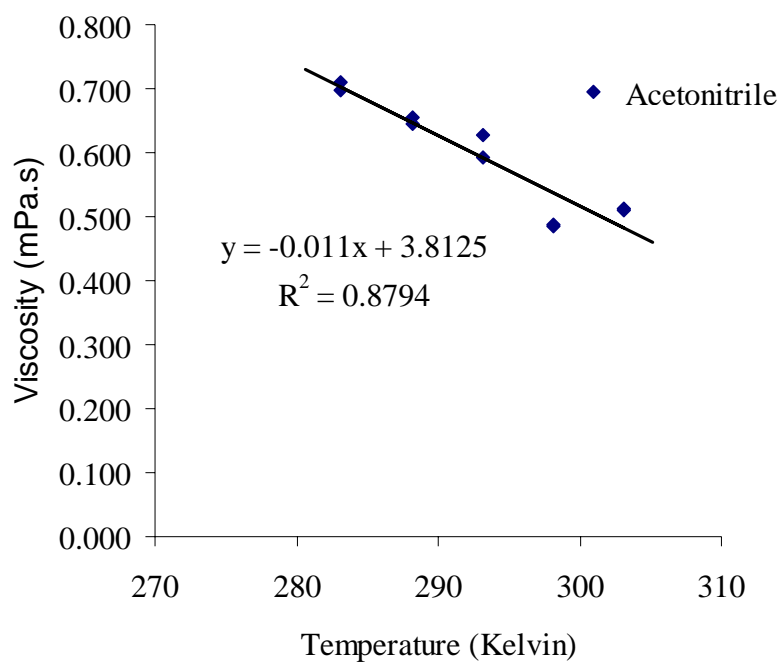


Figure 3.15. The Viscosity Variation of Acetonitrile with Temperature

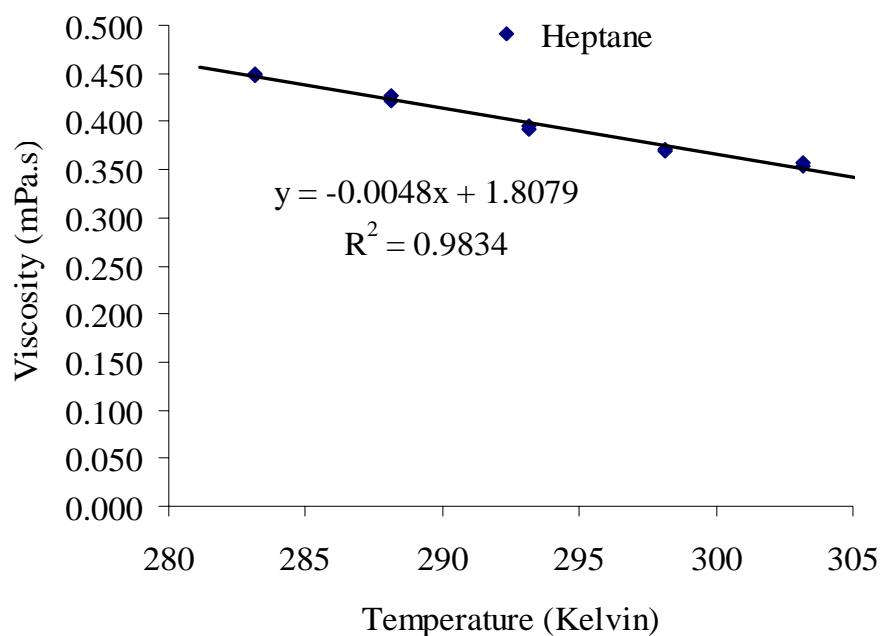


Figure 3.16. The Viscosity Variation of Heptane with Temperature

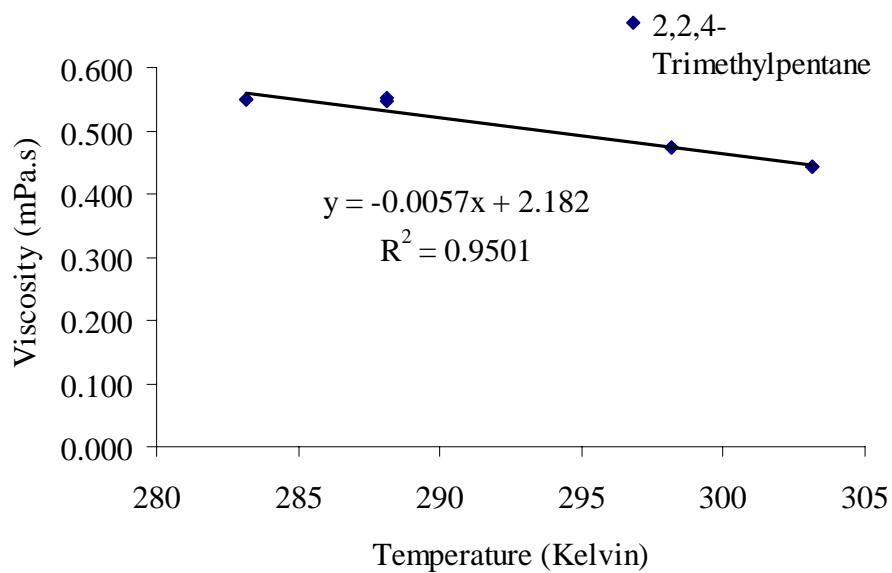


Figure 3.17. The Viscosity Variation of 2, 2, 4,-Trimethylpentane with the Temperature

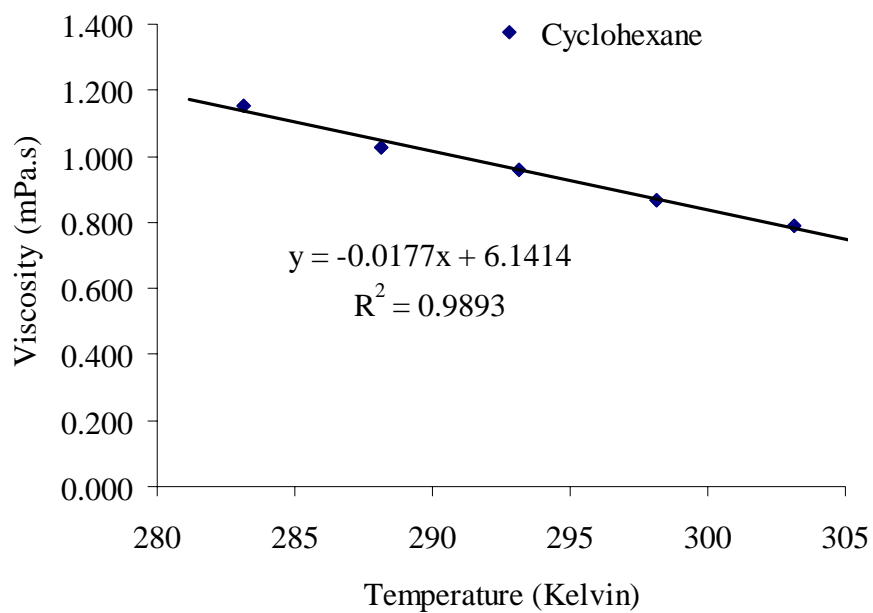


Figure 3.18. The Viscosity Variation of Cyclohexane with the Temperature

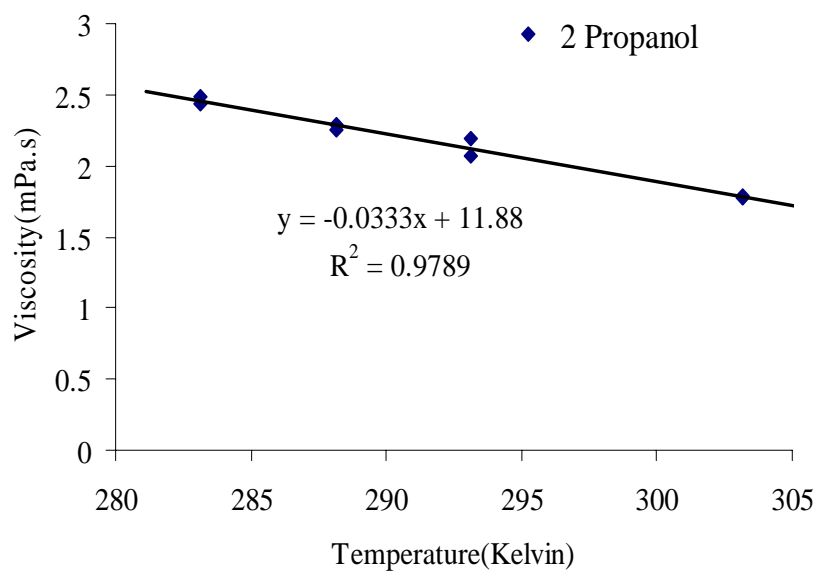


Figure 3.19. The Viscosity Variation of 2 Propanol with the Temperature

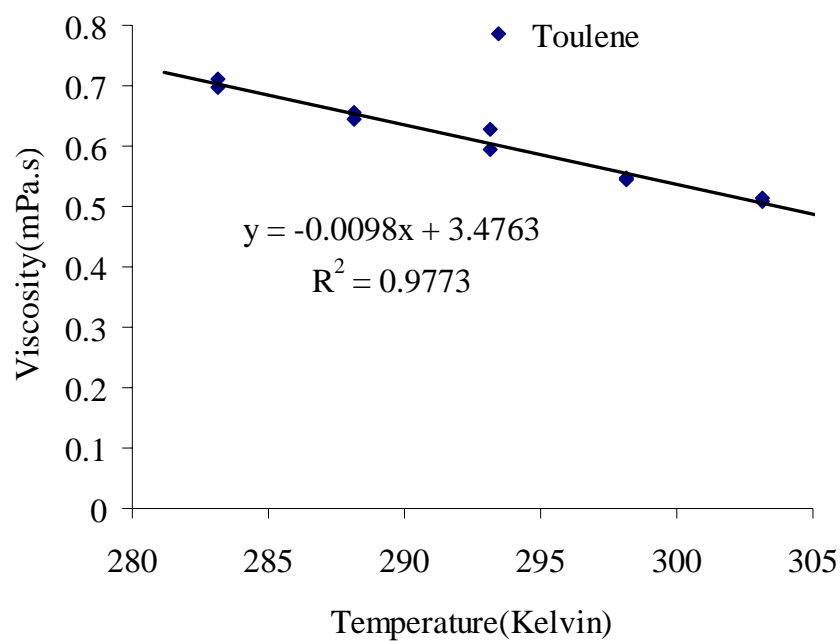


Figure 3.20. The Viscosity Variation of Toluene with the Temperature

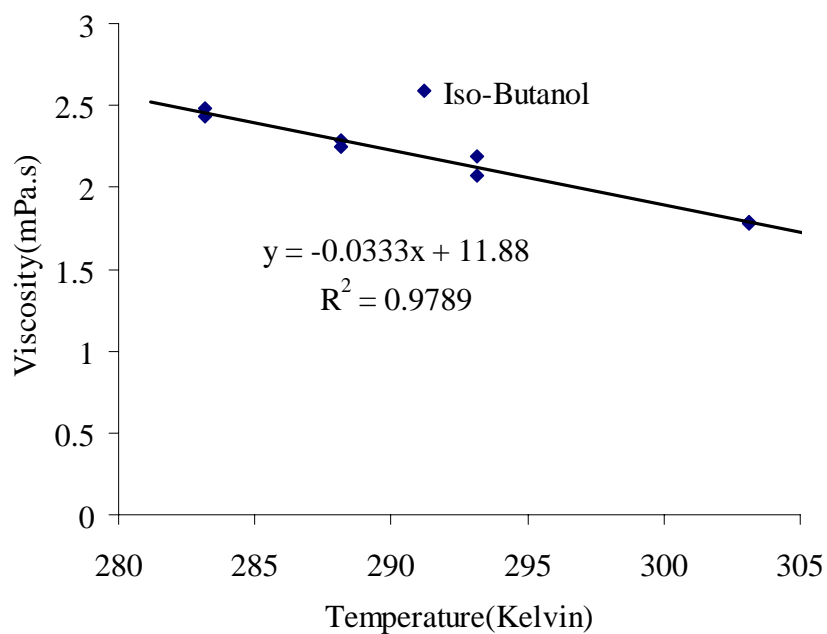


Figure 3.21. The Viscosity Variation of Iso-Butanol with the Temperature

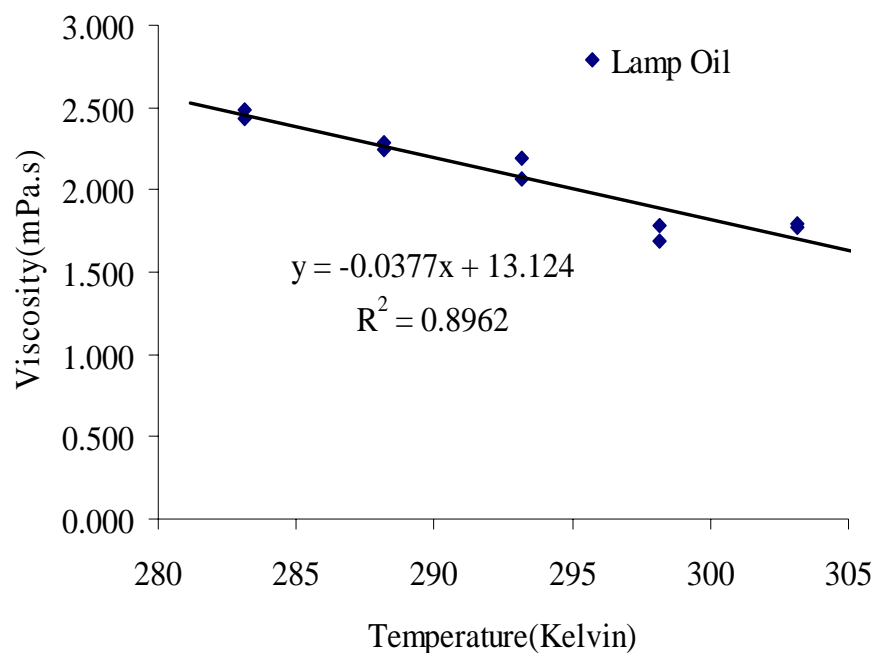


Figure 3.22. The Viscosity Variation of Lamp Oil with the Temperature

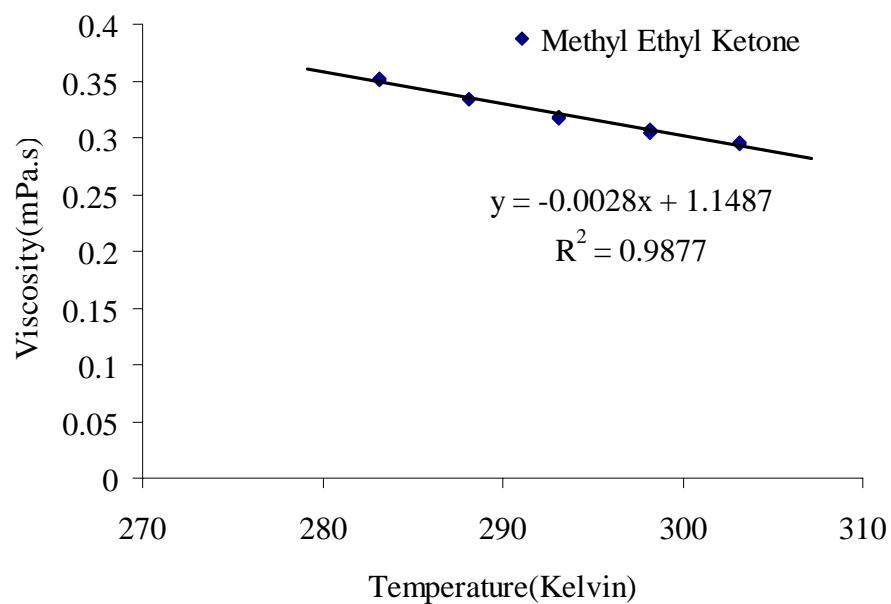


Figure 3.23. The Viscosity Variation of Methyl Ethyl Ketone with the Temperature

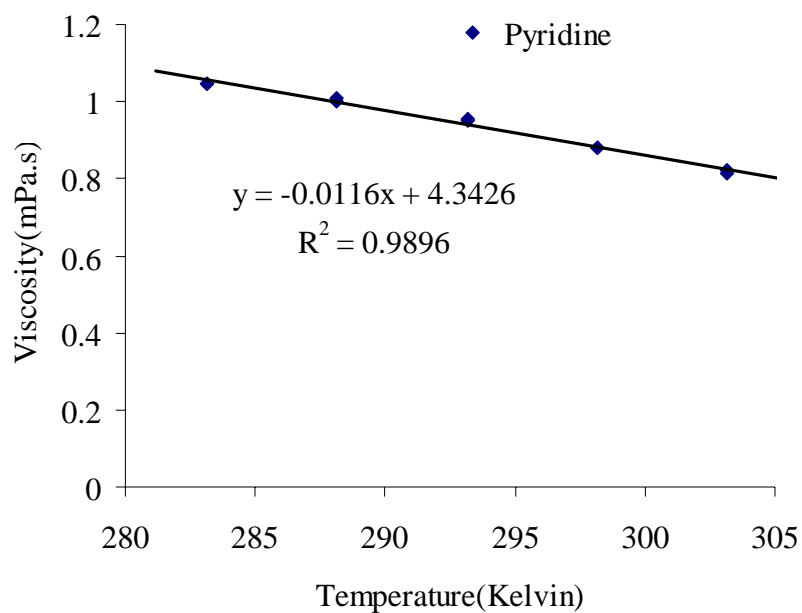


Figure 3.24. The Viscosity Variation of Pyridine with the Temperature

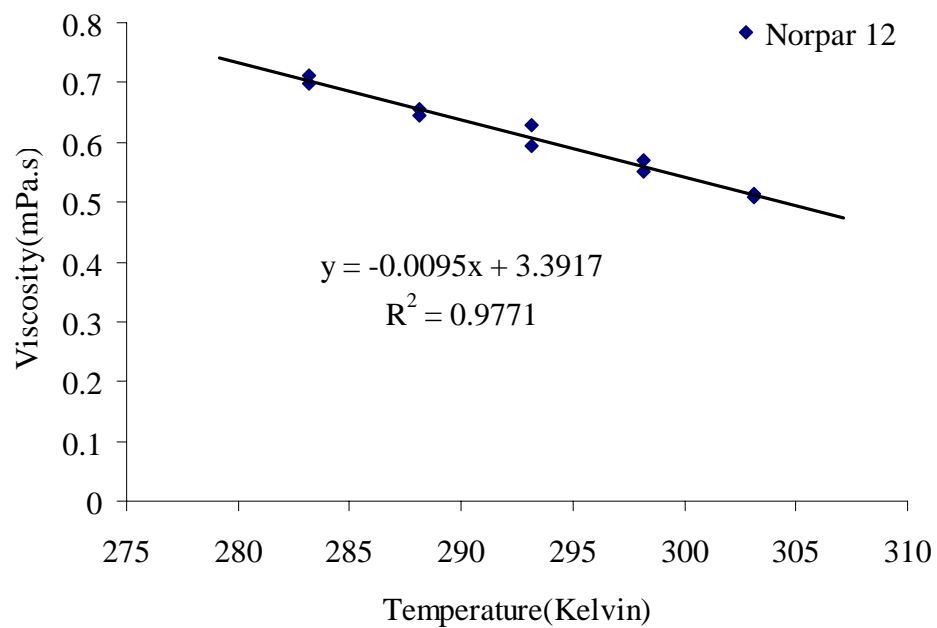


Figure 3.25. The Viscosity Variation of Norpar12 with the Temperature

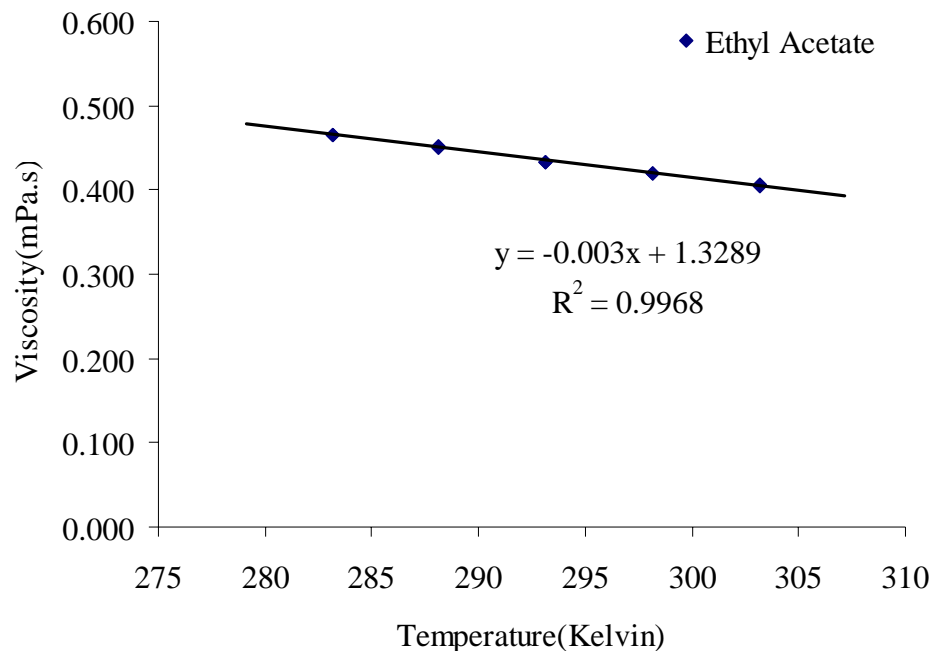


Figure 3.26. The Viscosity Variation of the Ethyl Acetate with Temperature

The volume ratio between the base pore fluid and compensating pore fluid was then recorded and its refractive index was measured. During the test, the temperature was kept at 25 °C. It was found that Toluene as a base pore fluid can make a refractive index matching fluid by mixing with 2 Propanol, Acetonitrile, Ethyl Acetate, Methyl Ethyl Ketone, and Iso-Butanol. However, Pyridine can not make the dry silica gel become transparent when mixed with any other solvent. The test results are summarized in Table 3.4. When the dry silica gel was added into the mixture of Toluene and Cyclohexane, air came out, but not as quick as that for Toluene and Ethyl Acetate, no obvious heat was released. The behavior observed when adding the compensating pore fluid to the base solvent Toluene was described in Table 3.4.

Another type of base fluid investigated in this research was Lamp Oil. Lamp Oil is a liquid petroleum product that is designed to burn cleanly in brass and glass oil lamps, torches and lanterns. It is from the same family as kerosene. Lamp Oil has been further processed and refined so that it doesn't produce as much harmful smoke, soot and other pollutants as kerosene. The Lamp Oil investigated in this research is 99% pure liquid wax

paraffin produced by Lamplight Farms, a Division of the W.C. Bradley Company. It was available at a local supermarket. Lamp Oil can be mixed with 2-Propanol, Acetonitrile, 2, 2, 4-Trimethylpentane, Ethyl Acetate, Iso-Butanol and Cyclohexane to reach the refractive index of dry silica gel. The test results are summarized in Table 3.5. When the dry silica gel was added into the mixture of Lamp Oil and Ethyl Acetate, air inside the silica gel pores quickly came out; and a large amount of heat was released. It took about 1 hour to make the silica gel become transparent. However, the transparency deteriorated when used with the large silica gel samples.

Table 3.4. Mixture of Toluene and the Compensating Solvents with Dry Silica Gel

Mixing Fluid	Transparency Effect	Volume Ratio	Refractive Index (25 °C)	Interactions Observed
Toluene : Cyclohexane	Poor	N/A	N/A	A moderate amount heat released
Toluene: 2 Propanol	Good	1.07:1	1.448	None
Toluene: Acetonitrile	Good	1.08:1	1.448	A large amount heat released
Toluene: 2,2,4,- Trimethylpentane	Poor	N/A	N/A	None
Toluene: Ethyl Acetate	Good	0.72:1	1.448	A large amount of heat released
Toluene: Methyl Ethyl Ketone	Good	0.95:1	1.448	A large amount of heat released
Toluene: Heptane	Poor	N/A	N/A	Turned into yellow color
Toluene: Iso- Butanol	Good	2.22:1	1.448	None
Toluene: Norpar12	Poor	N/A	N/A	None

Table 3.5. Mixture of Lamp Oil and the Compensating Solvents with Dry Silica Gel

Mixing Fluid	Transparency Effect	Mixing Ratio	Refractive Index (25 °C)	Interactions Observed
Lamp Oil: Cyclohexane	Poor	N/A	N/A	None
Lamp Oil: 2 Propanol	Good	1:0.15	1.434	Heat released
Lamp Oil: Acetonitrile	Poor	N/A	N/A	Separation found
Lamp Oil: 2,2,4,-Trimethylpentane	Poor	N/A	N/A	None
Lamp Oil: Ethyl Acetate	Good	1.28:1	1.434	Heat released, transparency deteriorates with large sample
Lamp Oil: Methyl Ethyl Ketone	Good	5:1	1.434	None, transparency deteriorates with large sample
Lamp Oil: Heptane	Poor	N/A	N/A	None
Lamp Oil: Iso-Butanol	Poor	N/A	N/A	Heat released
Lamp Oil: Norpar12	Poor	N/A	N/A	None

3.4. INVESTIGATION ON THE INTERACTIONS BETWEEN THE PORE FLUID AND THE LATEX MEMBRANE

The low viscosity pore fluids tested in this research are organic chemical solvents. Degradation of the membrane was of concern when exposed to these chemical solvents will be a concern during triaxial tests. Iskander, et al. (2002a) observed the deterioration of the latex membrane when using a pore fluid of Drakeol 35 and Norpar 12. In order to investigate the interaction between the pore fluid and the latex membrane, an immersion test program was conducted following ASTM D 543. It includes two parts: weight and dimension change of plastic membrane and measurement of mechanical property changes of the membrane.

3.4.1. Immersion Test. The latex membrane from Humboldt Company was selected as the testing material since it is commonly available at the lab for soil testing.

The specimen size of the tested membrane was 2.54 cm (1 in.) x 7.62 cm (3 in.) x 0.0635 cm (0.025 in.). It was weighed first. Then, the test specimen was completely immersed into the pore fluid for seven days, allowing the total surface area to be exposed to the fluid. After seven days, the specimen was removed from the container; after wiped dry, its weight and dimensions were remeasured. Observations were made on the appearance of the surface for each specimen after exposure to the pore fluid. Figure 3.27 shows the membrane before the immersion test. After the 7-day immersion test, the membrane was taken out. Immediately after being taken out, it were wiped dry and weighed. Then, the membrane was air dried for 40 hrs, they were weighed and measured again. Figure 3.28 shows the membranes after 40 hrs air dry. From these pictures, it can be observed that:

- 1) The pore fluid of Toluene and 2 Propanol mixture did not change the color of the membrane, which is a sign of low interaction.
- 2) The color of the membrane immersed into the mixed fluid of Toluene and the Methyl Ethyl Ketone, mixed fluid of Toluene and Acetronitrile, mixed fluid of Toluene and Iso-Butanol, and the mixed fluid of Lamp Oil and 2 Propanol had a moderate level of deterioration. The membrane immersed into the mixed fluid of Toluene + Ethyl Acetate, Lamp Oil + Methyl Ethyl Ketone, and Lamp Oil + Ethyl Acetate had the strongest color deterioration.
- 3) The membrane immersed into the pore fluid of Lamp Oil + 2 Propanol, Toluene + Iso-Butanol, Lamp Oil + Methyl Ethyl Ketone, and Lamp Oil + Ethyl Acertate curved after 40 hrs air dry after being taken out and wiped dry.

The immersion test data are shown in Table 3.6. The data shows that after the immersion, the mass of the membrane greatly increased due to the absorption of the pore fluid. There was also an increase in the length, width, and thickness for the membrane immersed in all the solvents. Also, there was an increase in the density for the membrane immersed in the pore fluid of Toluene and 2 Propanol, Toluene and Acetronile, Toluene and Ethyl Acetate, Toluene and Methyl Ethyl Ketone, and Toluene and Iso-Butnaol. However, the density for the membrane immersed in the pore fluid of Lamp Oil and 2 Propanol, Lamp Oil and Ethyl Acetate, Lamp Oil and Methyl Ethyl Ketone decreased.



Figure 3.27. The Membrane before the Immersion Test



Figure 3.28. The Membrane at 40 hrs after the Immersion Test

Table 3.6. Immersion Test on Humboldt Membrane

Testing Pore Fluid		T+2Pro	T+ Ace	T+EA	T+MK	T+IB	LO+ 2 Pro	LO+EA	LO+ MK
Mass Change (%)	7 days	185.58	53.17	260.92	220.95	245.28	262.96	278.18	282.76
Length Change (%)	7 days	35.06	9.74	46.75	38.16	41.56	53.85	57.69	61.04
Width Change (%)	7 days	32.81	20.69	48	38.46	48.44	60.00	60.78	67.33
Thickness Change (%)	7 days	53.85	0	46.15	46.15	7.69	53.85	53.85	53.85
Density Change (%)	7 days	3.48	15.65	13.70	14.79	52.58	-4.16	-3.05	-7.67
Mass Change (%)	40 hrs after	10.26	5.31	7.35	8.19	-1.89	31.48	32.73	43.10
Length Change (%)	40hrs after	0	-1.30	-1.30	0	1.82	6.41	15.38	12.99
Width Change (%)	40hrs after	1.56	4.83	4.00	0	-1.95	8.00	1.96	5.58
Thickness Change (%)	40hrs after	7.69	-7.69	0	0	-15.38	0	0	10.77
Density Change (%)	40hrs after	0.81	10.26	4.58	8.19	16.15	14.41	12.82	8.30

Note: T—Toluene; Ace—Acetronile; EA—Ethyl Acetate; MK—Methyl Ethyl Ketone; IB—Iso-Butanol; LO—Lamp Oil.

3.4.2. Tensile Test. The tensile test was performed on the latex membrane immediately after the immersion test. A low load capacity of 0.045 kN(10 lbs) and high sensitivity load cell was used in performing the tensile test because the load capacity of the latex membrane was very low. The deflection rate was taken as 0.085 cm/sec (2 inch/minute). The original size of the specimen for the tensile test before the immersion

was 3.81 cm (1.5 inch) in width and 76.2 cm (2.5 ft) in length. This specimen was prepared by cutting the 70 mm (2.8 inch) x 0.0381 mm (0.015 inch) Humbolt membrane roundly at a 15° angle. After the immersion test, the specimen was taken out and wiped dry. Then, it was cut into 12.7 cm (5 inch) pieces for the tensile test. The tensile test for the membrane was set up as shown in Figure 3.29. A typical tensile test is shown in Figure 3.30 for the latex membrane with a low degradation. The membrane can be stretched to six times its original length. The detailed information for the tested specimens is listed in Table 3.7. The stress-strain curve for the tested membranes is plotted in Figure 3.31. Latex0 was the original Humboldt membrane before any treatment. The test results showed that there was a strong degradation for the latex membranes immersed in the chemical solvents of the mixture of Toluene and Acetronile (latex10), Lamp Oil and 2 Propanol(latex54), Lamp Oil and Methyl Ethyl Ketone(latex13), Lamp Oil and Ethyl Acetate(latex17) in both the tensile strength and elasticity. For the latex membrane immersed in the water (latex1), the membrane became stronger but crispier, lost most of its elasticity; and the membrane was easily being torn apart. The latex membranes immersed in the mixture of Toluene and Acetronile (latex10), Lamp Oil and 2 Propanol (latex54), Lamp Oil and Methyl Ethyl Ketone (latex13), Lamp Oil and Ethyl (latex17) were broken at a low stress and also at a small strain level. The latex membranes immersed in the mixture of Toluene and Methyl Ethyl Ktone (latex14), Toluene and 2 Propanol (latex28) only had a slight degradation. For the membranes immersed in the mixture of Toluene and Ethyl Acetate (latex37), there was a drop in the tensile strength of the membrane, but the elasticity of the membrane did not drop. From these test results and the analysis, it was concluded that the mixtures of Toluene and Methyl Ethyl Ketone, Toluene and 2 Propanol would be the best choices for the pore fluid. The mixture of Toluene and Ethyl Acetate was also recommended to be used for manufacturing the transparent soil. The Lamp Oil was not recommended to make the transparent soil since it greatly reduced the tensile strength and elasticity of the latex membrane (latex13, latex17, latex54 as shown in Figure 3.31)



Figure 3.29. The Tensile Test Setup for the Latex Membranes



Figure 3.30. The Typical Testing Results for the Membrane of Low Degradation
(The specimen can be stretched to six times its original length)

Table 3.7. The Tensile Test Specimen and Test Description for the Latex Membrane

Sample Description	Sample No	Thickness (inch)	Width (inch)	Length (inch)	Test Condition Description
L + 2 Propanol	Latex54	0.018	2.283	3.824	Membrane being torn apart
L + MEK	Latex13	0.020	2.535	4.055	Slipped from grip, nearly exceeded the testing device capacity
T + Ace	Latex10	0.014	1.536	2.562	Used sand paper to suppress slipping, nearly exceeded the extension limit, aborted
T + Ethyl Acetate	Latex37	0.014	1.510	3.097	Sand paper used
T + 2 Propanol	Latex28	0.013	1.600	2.523	Membrane slipped
L + Ethyl Acetate	Latex17	0.012	2.348	2.681	Membrane being torn apart, sand paper used
Water	Latex1	0.015	1.500	2.761	Sand paper used, membrane slipped from the grip
T + MEK	Latex14	0.015	1.556	2.215	Sand paper used, membrane kinked, load dropped
Original Latex Membrane	Latex0	0.015	1.518	2.227	Sand paper used, membrane kinked

Note: T- Toluene, MEK-Methyl Ethyl Ketone, L-Lamp Oil, Ace-Acetonitrile,

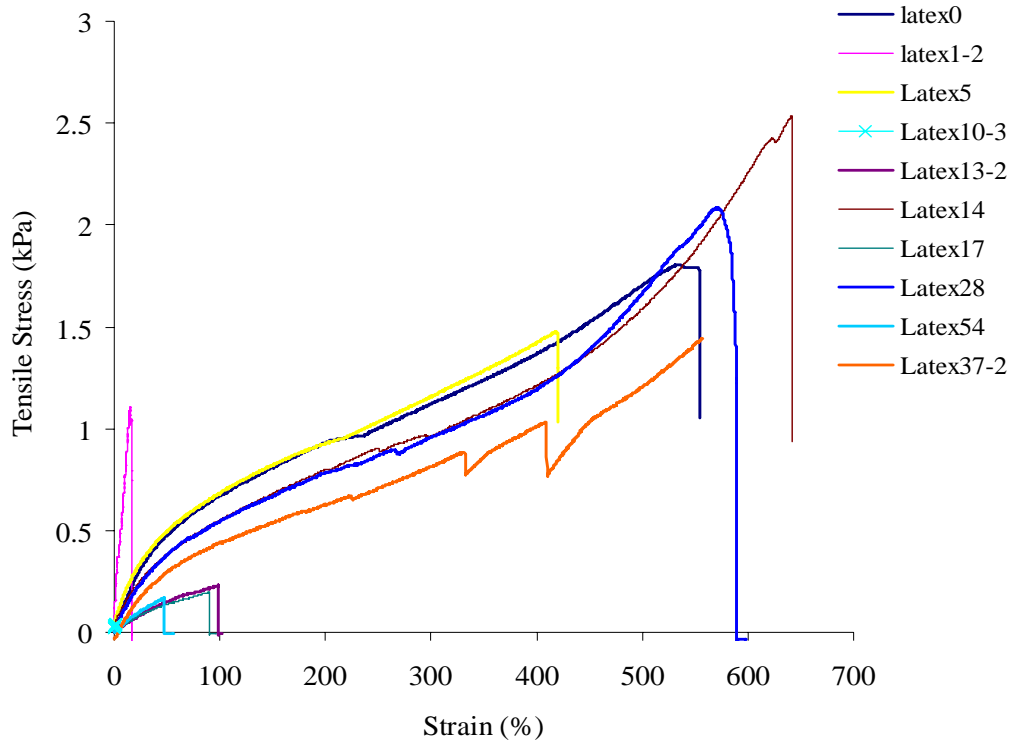


Figure 3.31. The Stress-Strain Curve for the Latex Membranes Immersed into Different Chemical Solvent Mixtures

3.5. DISCUSSIONS ON THE LOW VISCOSITY PORE FLUID FOR THE SHAKE TABLE TEST

In this research, the transparent soil was to be used to perform the shaking table test which points out the special concern for the viscosity of the pore fluid. In any dynamic test with saturated soil, the generation and dissipation of excess pore water pressure is a significant issue. The generation and dissipation of pore pressure is closely related to the permeability of the soil. The permeability of a soil can be expressed as follows:

$$k_{s,f} = \frac{\rho_f g k_s}{\eta_f} = \frac{g k_s}{\nu_f} \quad (3.2)$$

where ρ_f = pore fluid density, g = gravitational acceleration, k_s = intrinsic permeability of soil, η_f = dynamic viscosity of pore fluid, and $\nu_f = \eta_f / \rho_f$ kinematic viscosity of pore fluid. The kinematic viscosity of water at 20°C is 1.007 cSt (centistokes). Because of the porous structure of the silica gel, its intrinsic permeability is different from that of water. So when low viscosity pore fluid is used for the silica gel in a shake table test, the permeability of the transparent soil will be much higher than that of water. When interpreting the testing data about the dissipation of pore water pressure, the pore pressure data obtained needs to be further processed to mimic what really would happen in the natural soil (sand). An appropriate scale rule can be adopted to interpret the pore water pressure data. This will not be further discussed in this research since it is not the focus of the research program.

3.6. SUMMARY

This section has presented results of searching for a low viscosity pore fluids, the refractive index and viscosity testing results on the tested chemical solvents, and the interaction between the pore fluid and the latex membrane. Conclusions obtained through this series of tests are as follows:

- 1) In the temperature range of 15°C -35 °C, it was found out that the refractive index and the viscosity of all the tested chemical solvents varied linearly with the temperature (in Kelvin).
- 2) Toluene can make the matching refractive index pore fluid with a low viscosity. The compensating chemical solvents are: 2 Propanol, Acetonitrile, Ethyl Acetate, Methyl Ethyl Ketone, Iso-Butanol. The matching volume ratio is 1.07:1, 1.08:1, 0.72:1, 0.95:1, and 2.22:1, respectively. The matching refractive index is 1.447 at 25 °C, which is consistent with Iskander's testing data. Among them, the pore fluid made from the Toluene and Acetonitrile will cause a strong degradation to the latex membrane; the pore fluid of Toluene and Methyl Ethyl Ketone, Toluene and 2 Propanol will cause the least degradation effect on the latex membrane; the pore fluid of Toluene and Iso-Butanol only caused a small amount drop in the tensile strength of the latex membrane.

- 3) Lamp Oil can also make a low viscosity pore fluid for the transparent soil. The compensating chemical solvents are: 2 Propanol, Ethyl Acetate, and Methyl Ethyl Ketone. The matching volume ratio is 1.0:0.15, 1.28:1, 5:1. The matching refractive index is 1.434 at 25 °C. However, these pore fluids caused a strong degradation of the latex membrane. Hence, they are not recommended to manufacture transparent soil.

4. DYNAMIC MECHANICAL BEHAVIOR OF TRANSPARENT SILICA GEL

4.1. INTRODUCTION

Static mechanical behavior of transparent soil has been investigated by Iskander (1994, 1998) and Iskander et al. (2002a, b) and reviewed in the literature section. Their research focused on the static properties of transparent soil, and testing data obtained from their investigations showed that the stress-strain behavior for fine and coarse silica gels was consistent with the typical stress strain behavior of sands. However, the peak strength of silica gels was reached at higher strains than normally expected for natural sands, which was due to the compressibility of the silica gel particles. In this research, the static behavior of silica gel will not be studied; Iskander's testing data can be taken as a reference.

Even though comprehensive tests have been performed on silica gels to investigate their static properties, the author of this research has not found any information available about the dynamic behavior of transparent silica gels. Therefore, the research presented in this dissertation focuses on the dynamic properties of transparent silica gels. A series of resonant column tests were conducted in this section. The shear modulus and damping behavior of the transparent silica gel were presented.

4.2. METHOD TO EVALUATE DYNAMIC PROPERTIES OF SOIL

The loading frequency for an earthquake event is typically from 1 to 3 Hz. The soil underneath railways and road pavements usually experiences load frequency ranges from 1 to 10 Hz with a very large number of repetitions. Pile driving and machinery foundation can apply loads at very high speeds from 0.1 to 0.01 seconds (10 to 100 Hz). Blasting can apply shock or impulse loads at speeds of up to 1000 Hz. Quite a few devices are now available to test the dynamic properties of soil in the field and in the laboratory. An ultrasonic device, resonant column, cyclic triaxial machine, and simple cyclic triaxial machine are commonly used laboratory devices to test the dynamic properties of soil. Figure 4.1 shows the suitable testing strain level of different devices and the field events associated with different strain levels. The cross-hole test, down-hole test, and spectral analysis surface wave method are the field methods used to obtain the

dynamic properties of soil in the field. In this research, a resonant column device was used to test the dynamic properties of the silica gels. Sitharam et al. (2004) summarized the available testing methods for measuring the dynamic properties of soil as shown in Figure 4.2.

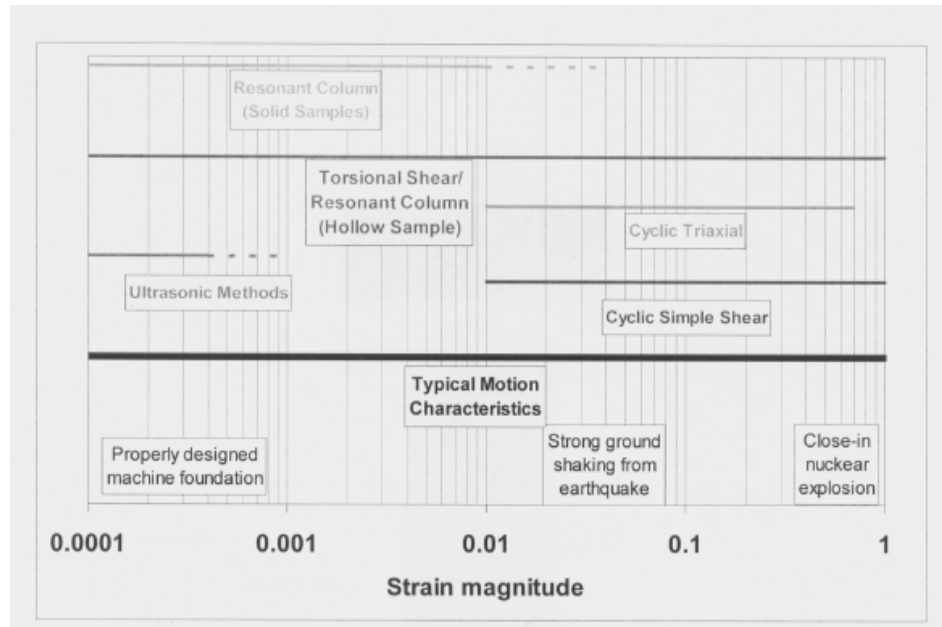


Figure 4.1. Typical Strain Level Associated with Different Laboratory Tests and Field Events (GCTS Resonant Column Manual)

The resonant column test is the most commonly used laboratory test for measuring the dynamic soil properties at low to medium strain levels. The test is performed by vibrating a solid or hollow soil column in one of its natural modes. The shear wave velocity is then determined from the resonant frequency. The resonant column apparatus used in this research program is from GCTS. In the GCTS resonant column device, a harmonic torsional excitation is applied to the top of the specimen by an electromagnetic motor. A torsional harmonic load with constant amplitude is applied over

a range of frequencies, and the response curve (strain amplitude) is measured. The shear modulus is calculated using Equation (4.1):

$$G = \rho V_s^2 \quad (4.1)$$

where ρ is the density of the soil, and V_s is the shear wave velocity of the soil.

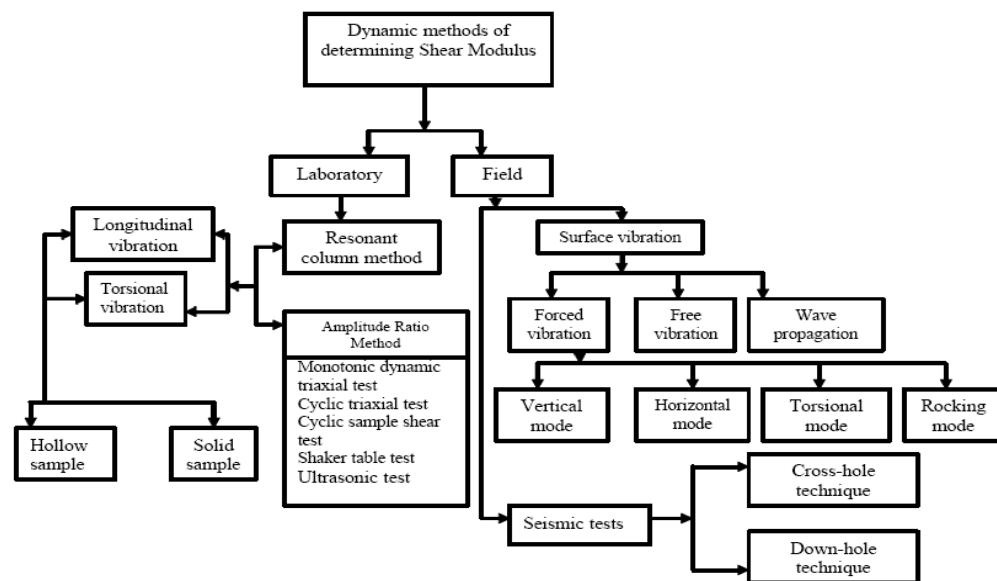


Figure 4.2. Classification of Dynamic Methods of Obtaining the Shear Modulus (Sitharam, GovindaRaju and Sridharan, 2004)

Material damping can be obtained from either the free-vibration decay stage or from the width of the frequency response curve assuming viscous damping (the Half-power width method). The torsional harmonic load amplitude is increased with each test to obtain the shear modulus and damping values for different strain ranges. Figure 4.3 shows the GCTS resonant column device used in this research.

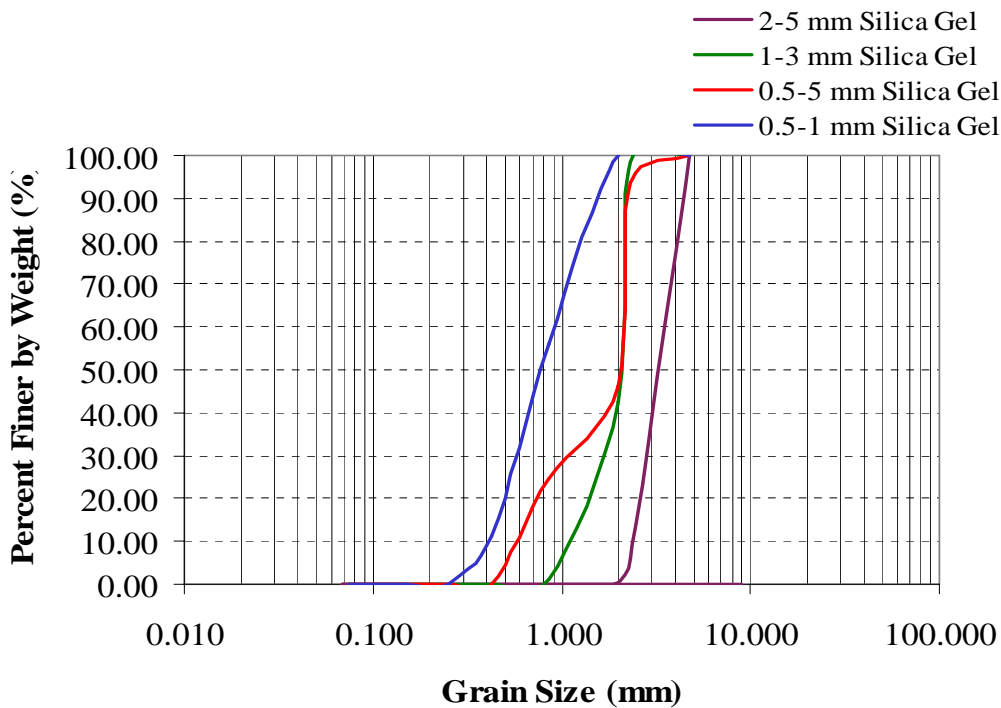


Figure 4.3. GCTS Resonant Column Apparatus

4.3. TESTING PROGRAM AND SAMPLE PREPARATION

Hardin and Drnevich (1972 a) summarized that the shear strain amplitude, effective stress level, and void ratio are the primary factors that affect the shear modulus in clean sands. The grain size, grain shape, and degree of saturation have a secondary influence on the shear modulus of sands. The damping ratio was also considered to be affected by these factors. The effective confining stress, void ratio, and strain amplitude were selected as the controlling factors in setting up the test program. The selected strain level ranged from 10^{-5} to 10^{-3} , and four different grain sizes of silica gel as shown in Figure 4.4 were tested. They were within the range of 2-5 mm, 1-3 mm, 0.5-1 mm, and 0.5-5 mm, respectively. In the current study, for each type of grain size, silica gel samples at two different void ratios were tested, representing the dense and loose state of the silica gel. For each sample, the confining pressure varied from 50 kPa to 100 kPa, 200 kPa, 300

kPa and 400 kPa. The air pluviation method was used to prepare the loose sample. Silica gel was poured from a nozzle while maintaining a constant drop-height (4.0 cm) throughout the preparation. Then, the confining pressure was applied to the specimen. The confining pressure was raised to the desired value for each test. For the dense sample, the whole sample was evenly divided into five layers, and then each layer was compacted by a miniature compactor. The mass of silica gel for each layer was determined by trial and error. The average sample diameter was 70 mm, and the average height of the sample was 158 mm. Table 4.1 lists the testing specimens and the testing program.



SILT or CLAY	SAND			GRAVEL	
	Fine	Medium	Coarse	Fine	Coarse

Figure 4.4. Grain Size Distribution for Tested Silica Gel

Table 4.1. Resonant Column Testing Program

Silica Gel Specimen	Confining Pressure (kPa)					Grain Size	Void Ratio	Height/ Diameter
	50	100	200	300	400			
L-11	50	100	200	300	400	2-5 mm	1.885	163.5/68.82
L-12	50	100	200	300	400	2-5 mm	1.908	157/70.70
L-d1	50	100	200	300	400	2-5 mm	1.775	160/71.71
L-d2	50	100	200	300	400	2-5 mm	1.797	160.03/71.17
M-11	50	100	200	300	400	1-3 mm	1.882	150.81/71.16
M-12	50	100	200	300	400	1-3 mm	1.881	158.75/69.384
M-d1	50	100	200	300	400	1-3 mm	1.776	157/71.26
M-d2	50	100	200	300	400	1-3 mm	1.791	161.92/72.11
S-11	50	100	200	300	400	0.5-1mm	1.912	157/67.01
S-12	50	100	200	300	400	0.5-1mm	1.886	156.37/70.25
S-d1	50	100	200	300	400	0.5-1 mm	1.778	160/70.29
S-d2	50	100	200	300	400	0.5-1mm	1.831	161.92/71.52
C-11	50	100	200	300	400	0.5-5 mm	1.542	160.4/67.24
C-12	50	100	200	300	400	0.5-5 mm	1.536	155.4/69.12
C-d1	50	100	200	300	400	0.5-5 mm	1.475	157.8/68.85
C-d2	50	100	200	300	400	0.5-5 mm	1.482	156.37/69.28

(L-11, loose sample 1; L-12, loose sample 2; L-d1, dense sample 1; L-d2, dense sample 2, etc.)

4.4. RESONANT COLUMN TEST RESULTS

The torsional resonant column apparatus from Geotechnical Consulting and Testing Systems (GCTS) was used in this research. The theory of the resonant column tests can be found in Drnevich et al. (1978). The resonant column device has a fixed bottom and a rotating top. An accelerometer was used as the output to obtain the angular displacement and shear strain of the silica gel specimen. The specimens were tested at five different confining pressures: 50 kPa, 100 kPa, 200 kPa, 300 kPa, and 400 kPa. ASTM D 4015 specification was followed as the operating and data reduction procedure.

Typical shear modulus and damping ratio results for silica gel specimens are shown in Figures 4.6 to 4.30.

4.4.1. Small-Strain Shear Modulus of Silica Gel. This section discusses the characteristics of a small-strain shear modulus for a silica gel specimen with different void ratios under the influence of the confining pressure. Richart (1977) stated that the shear modulus at a strain amplitude of 10^{-5} or less can be taken as the small-strain shear modulus for soils. In this study, the shear modulus at a strain amplitude of 10^{-5} was treated as the small-strain shear modulus, G_{\max} , for silica gel. The small-strain shear modulus, G_{\max} , for silica gel at different void ratios of different grain sizes was plotted under different mean effective stresses as shown in Figure 4.5. This shows that the G_{\max} increases with increasing confining pressure and the G_{\max} of the dense silica gel sample is slightly higher than G_{\max} of the loose silica gel sample under the same confining pressure for the same grain size specimen. When the mean effective stress continues to increase, the small-strain shear modulus curve tends to become flat. For sand, it is generally agreed upon that the G_{\max} increases with increasing confining pressure (Larid and Stoke, 1993). At a confining stress higher than 400 kPa, the shear modulus of sand continues to increase. From the above discussion, it can be concluded that the G_{\max} for silica gel has similar behavior as that of sands at low confining pressure; however, silica gel shows different behavior from that of sands at high confining pressure. The void ratio is an important factor that influences the small-strain shear modulus. The grain size distribution has a secondary effect on the small-strain shear modulus.

4.4.2. Modulus Reduction Behavior and Damping Characteristics of Silica Gel. Figures 4.6 to 4.21 show the variation of the shear modulus and normalized shear modulus as a function of the shear strain for silica gel. It is clear that the reduction in the shear modulus and increase in damping varied significantly throughout a wide range of shear strains tested. The silica gel specimen with a smaller void ratio had a higher shear modulus than did silica gel with a large void ratio under the same confining pressure. Within the linear shear strain range, the shear modulus of silica gel increased with an increase in the confining pressure. However, beyond the threshold shear strain value, the

silica gel samples tended to have the same values of shear modulus irrespective of the initial void ratio and confining pressure of the silica gel.

In order to compare the behavior of sand more clearly with the behavior of silica gel, the extracted values of shear modulus for silica gel were plotted together with the typical values of sand from Seed and Idriss (1970) as shown in Figure 4.22. It is clear that the normalized shear modulus values of silica gel are above the range of values for sand. The silica gel specimen has a clear range of linear elastic behavior and nonlinear elastic range of elastic behavior; and after passing the nonlinear elastic threshold strain, the silica gel exhibited a more dramatic degradation behavior. This is possibly due to the much more compressible behavior of the silica gel.

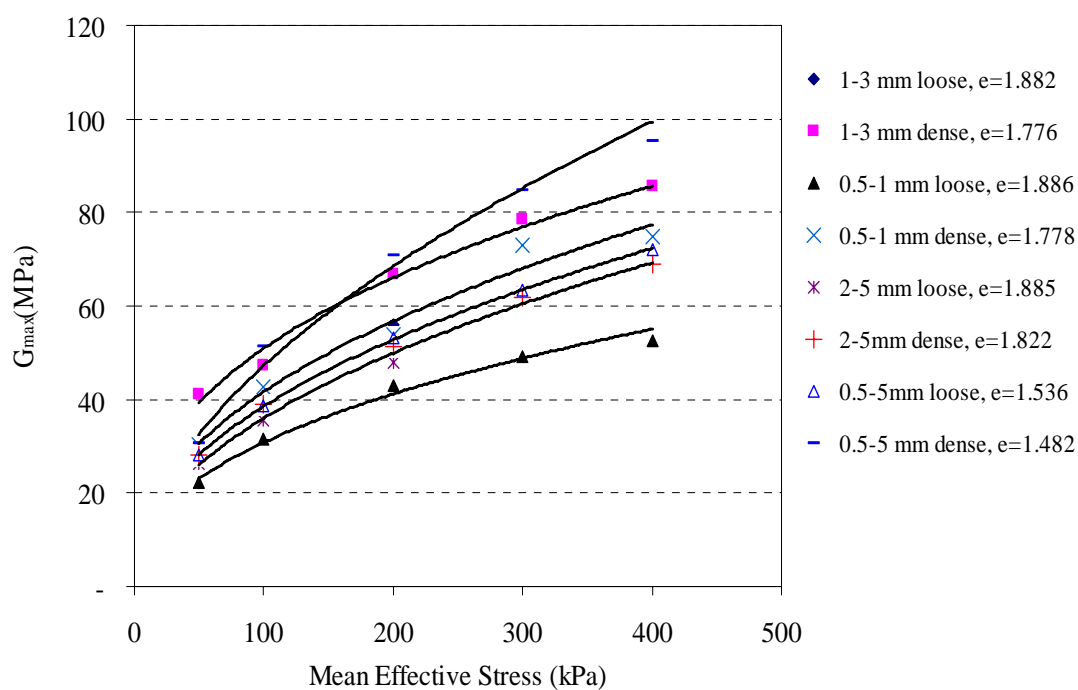


Figure 4.5. Variation of the Small-Strain Shear Modulus of Silica Gel

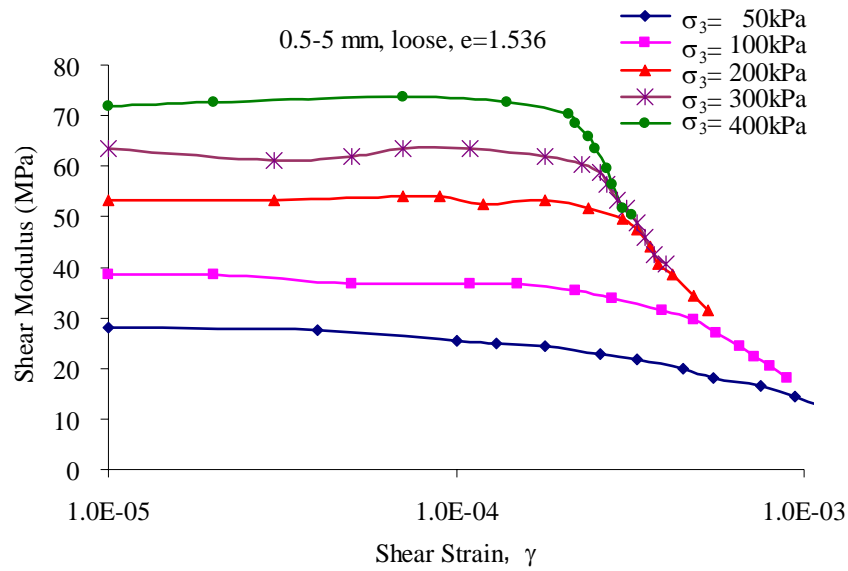


Figure 4.6. Shear Modulus Degradation with Shear Strain for a 0.5-5 mm Loose Silica Gel Sample under Different Confining Pressures

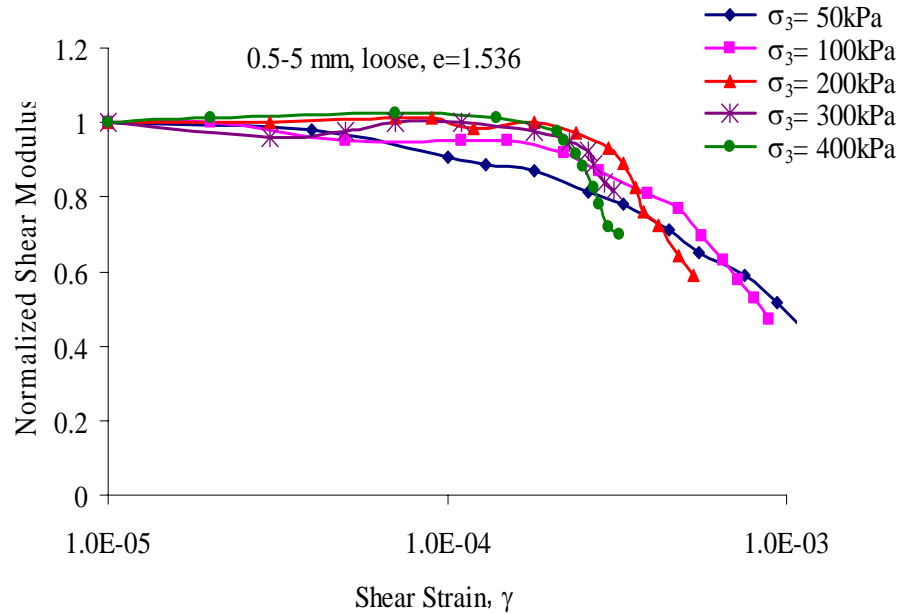


Figure 4.7. Normalized Shear Modulus Degradation with Shear Strain for a 0.5-5 mm Loose Silica Gel Sample under Different Confining Pressures

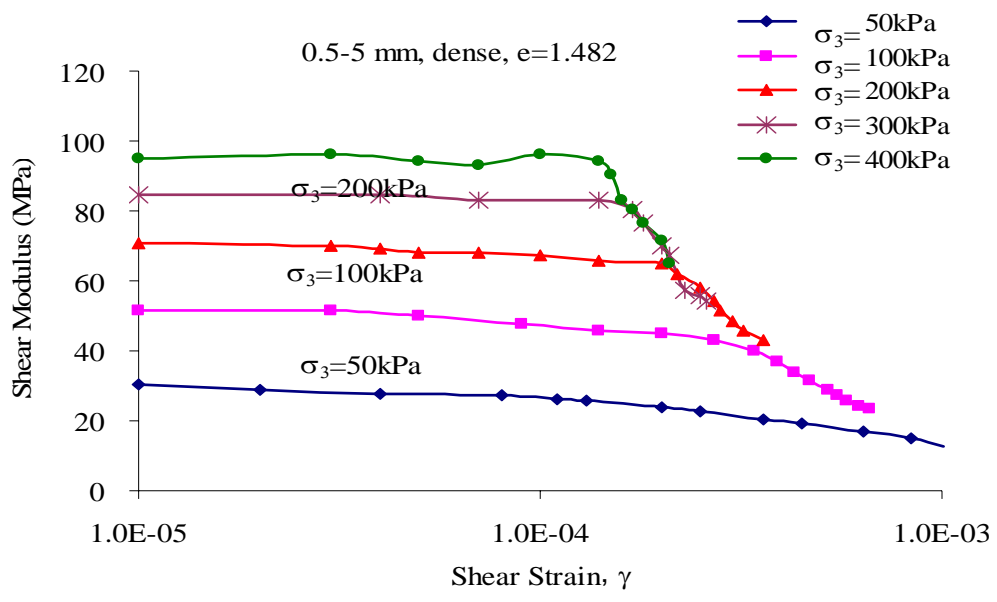


Figure 4.8. Shear Modulus Degradation with Shear Strain for a 0.5-5 mm Dense Silica Gel Sample under Different Confining Pressures

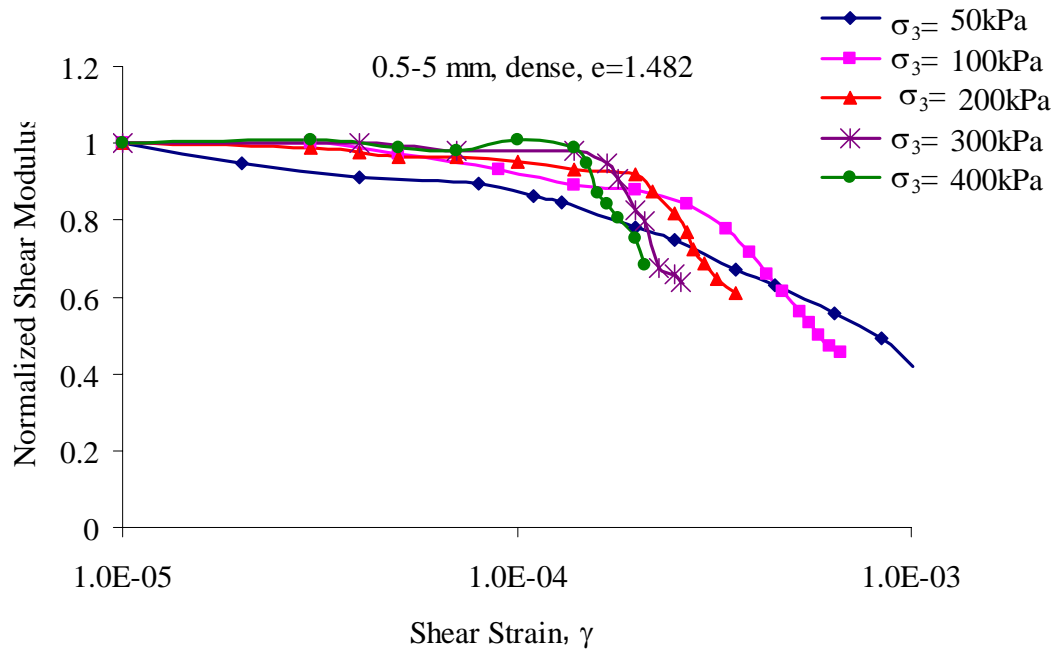


Figure 4.9. Normalized Shear Modulus Degradation with Shear Strain for a 0.5-5 mm Dense Silica Gel Sample under Different Confining Pressures

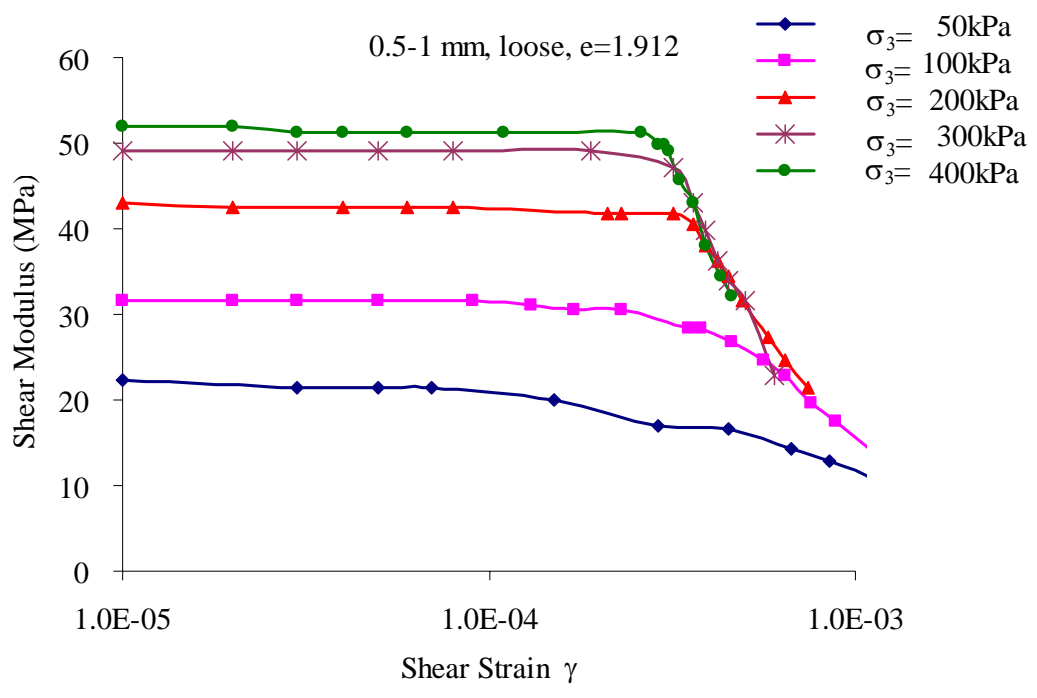


Figure 4.10. Shear Modulus Degradation with Shear Strain for a 0.5-1 mm Loose Silica Gel Sample under Different Confining Pressures

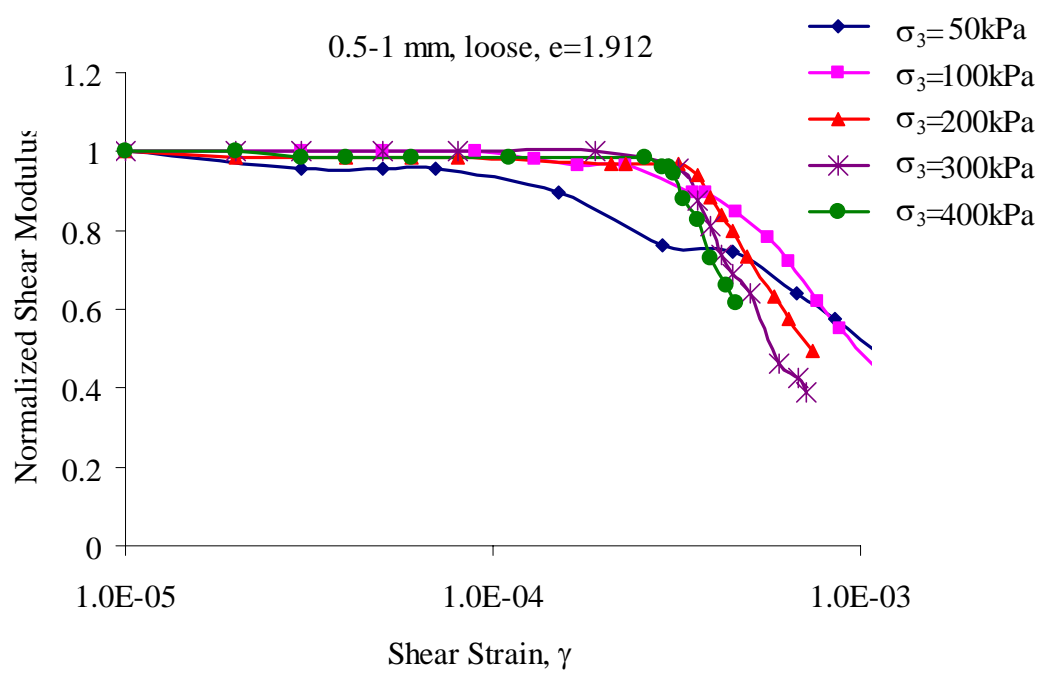


Figure 4.11. Normalized Shear Modulus Degradation with Shear Strain for a 0.5-1 mm Loose Silica Gel Sample under Different Confining Pressures

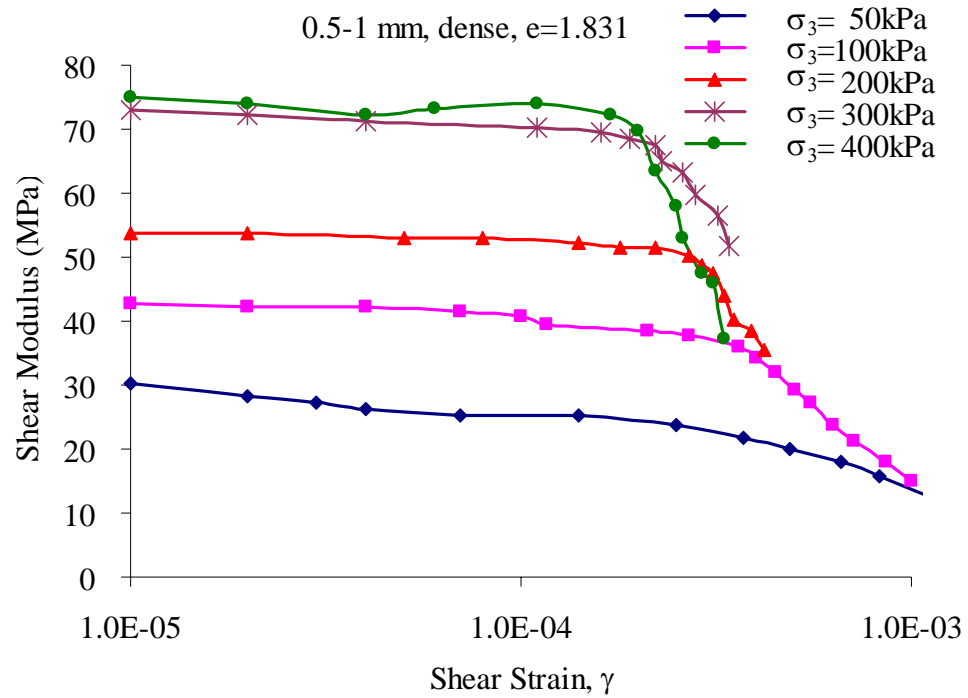


Figure 4.12. Shear Modulus Degradation with Shear Strain for a 0.5-1 mm Dense Silica Gel Sample under Different Confining Pressures

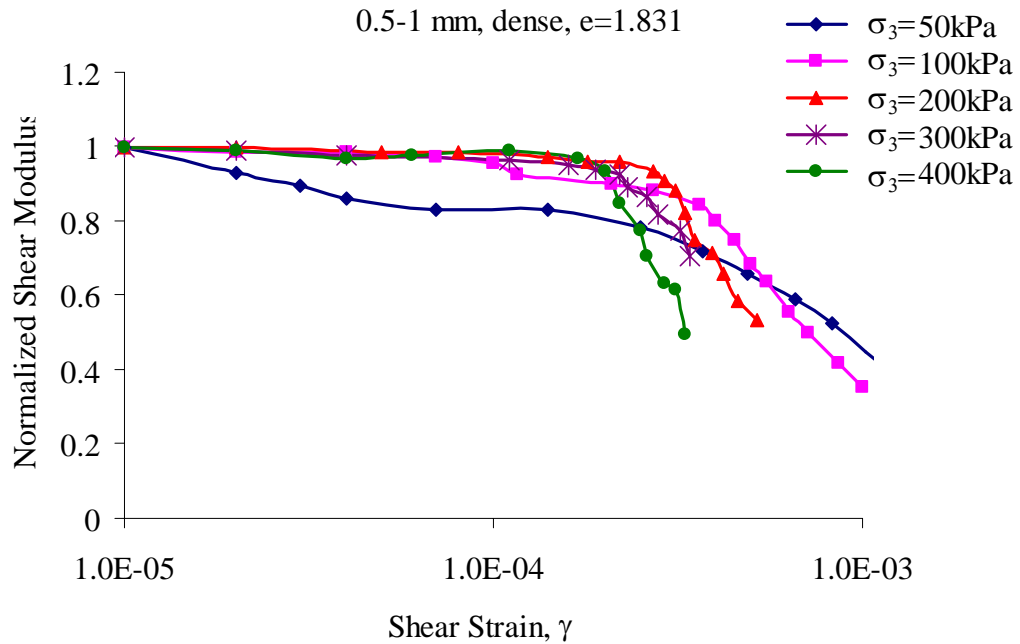


Figure 4.13. Normalized Shear Modulus Degradation with Shear Strain for a 0.5-1 mm Dense Silica Gel Sample under Different Confining Pressures

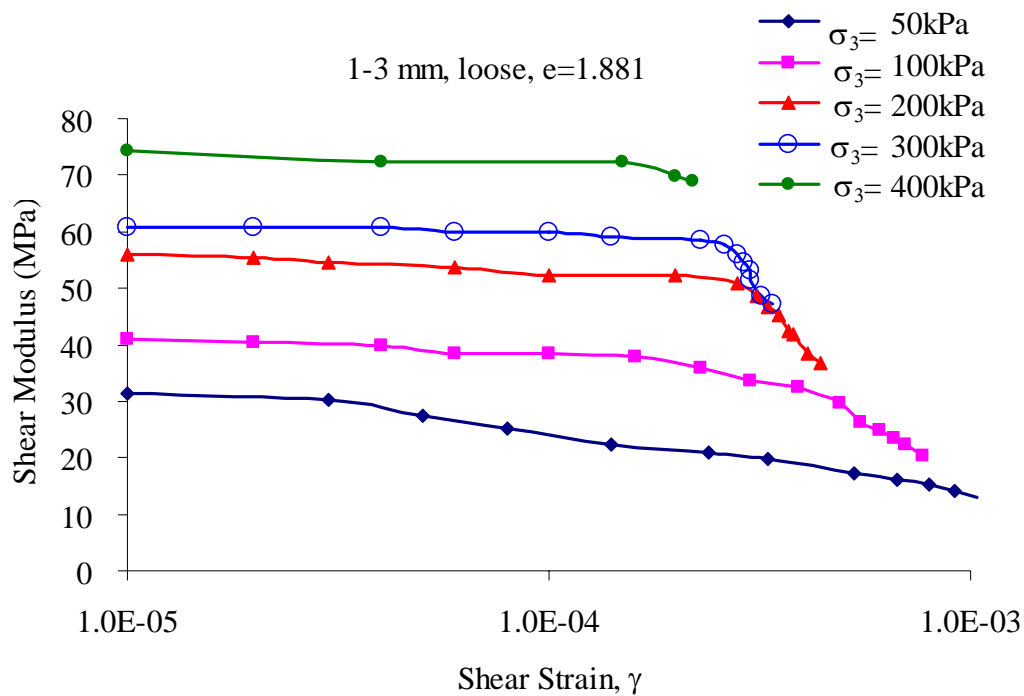


Figure 4.14. Shear Modulus Degradation with Shear Strain for a 1-3 mm Loose Silica Gel Sample under Different Confining Pressures

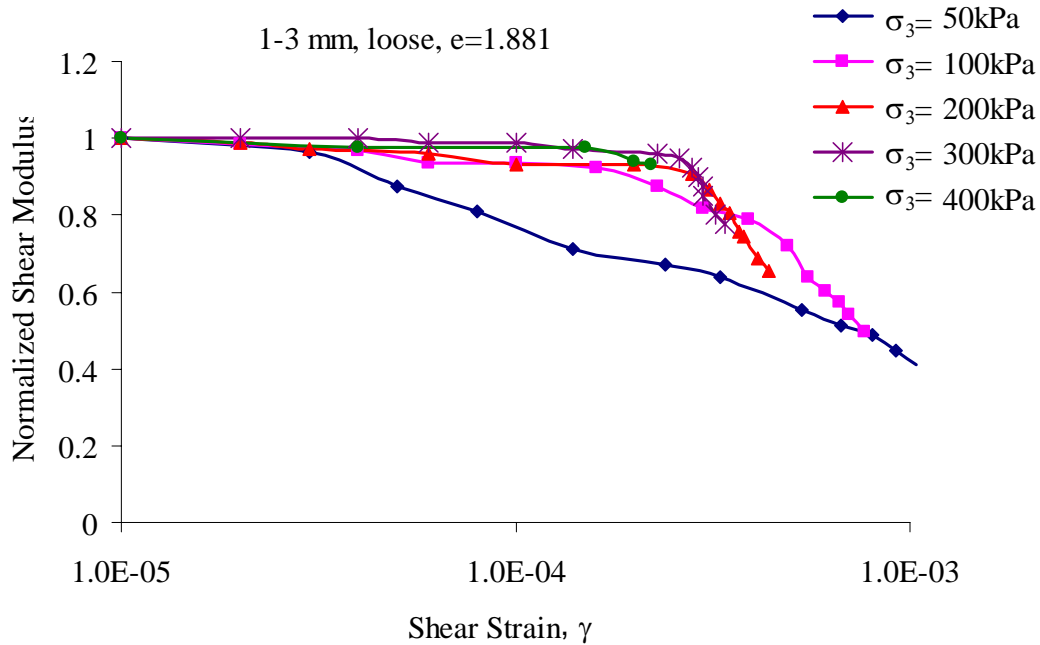


Figure 4.15. Normalized Shear Modulus Degradation with Shear Strain for a 1-3 mm Loose Silica Gel Sample under Different Confining Pressures

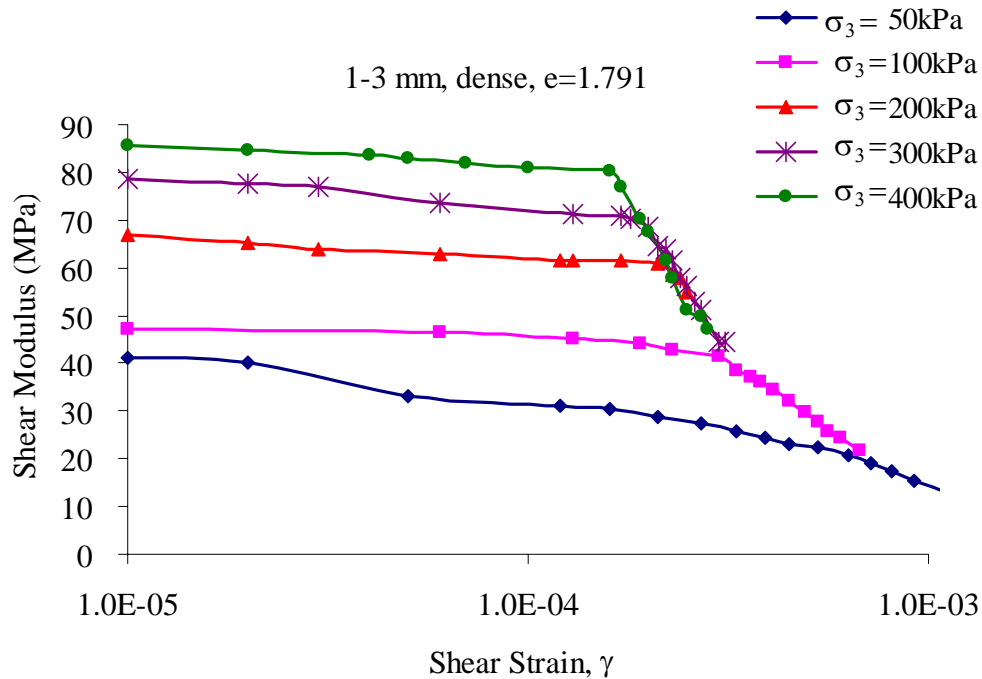


Figure 4.16. Shear Modulus Degradation with Shear Strain for a 1-3 mm Dense Silica Gel Sample under Different Confining Pressures

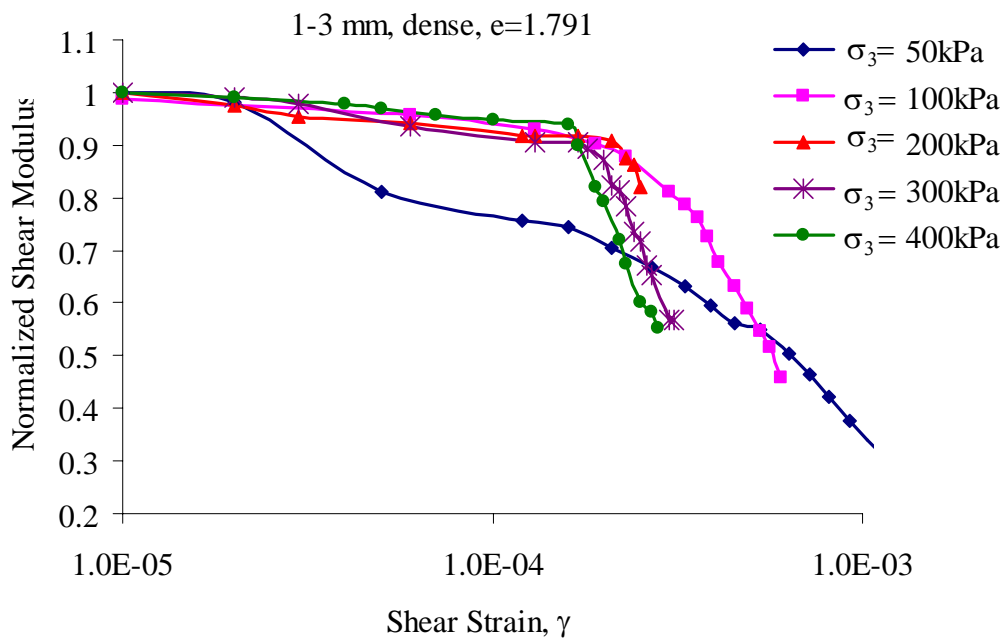


Figure 4.17. Normalized Shear Modulus Degradation with Shear Strain for a 1-3 mm Dense Silica Gel Sample under Different Confining Pressures

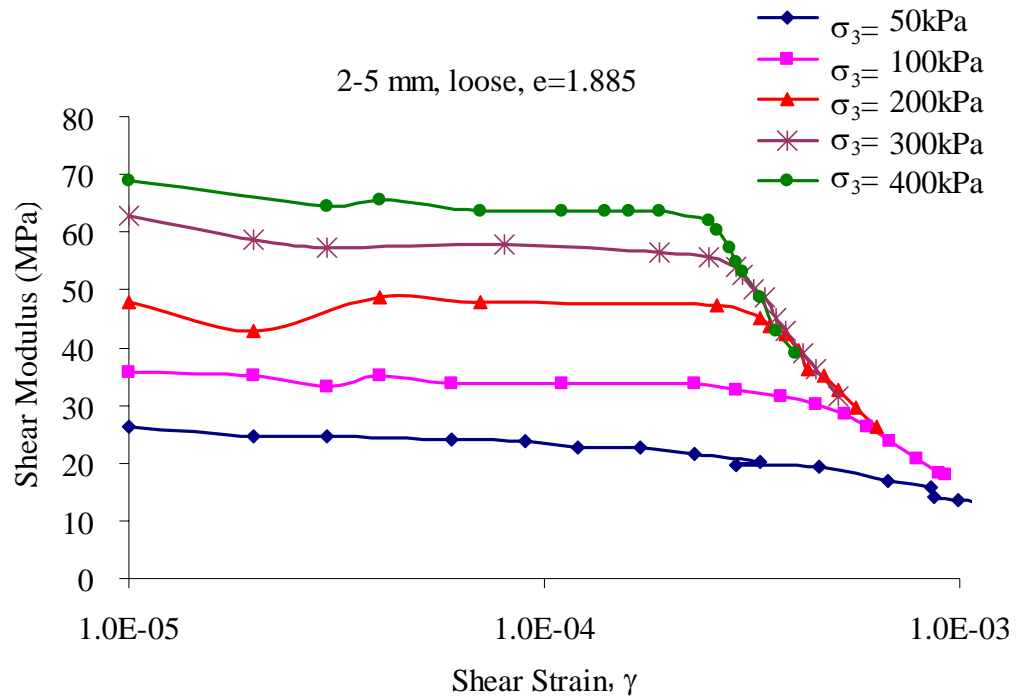


Figure 4.18. Shear Modulus Degradation with Shear Strain for a 2-5 mm Loose Silica Gel Sample under Different Confining Pressures

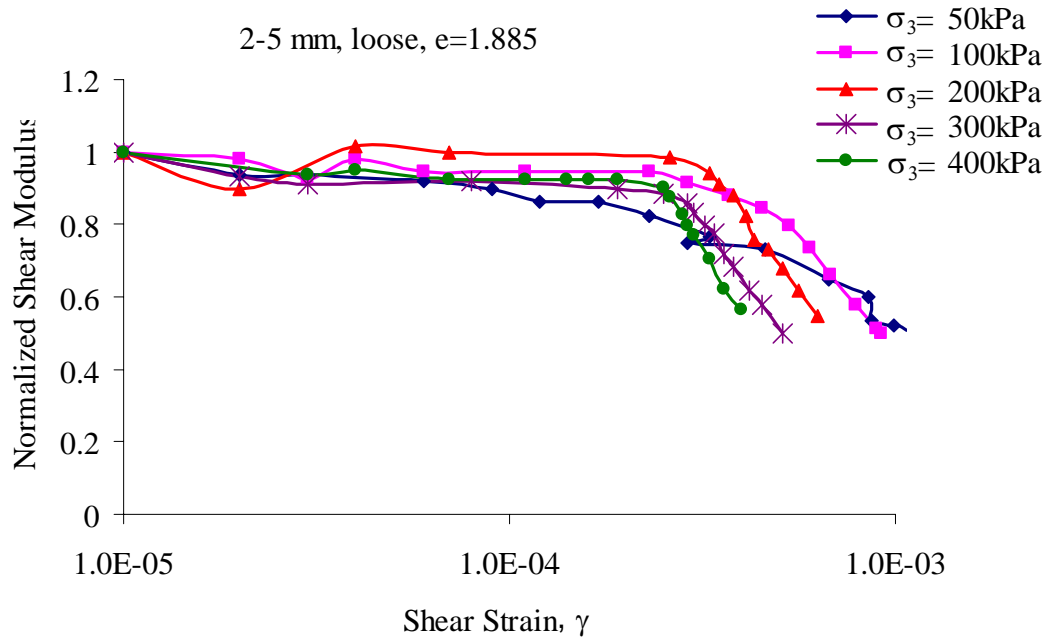


Figure 4.19. Normalized Shear Modulus Degradation with Shear Strain for a 2-5 mm Loose Silica Gel Sample under Different Confining Pressures

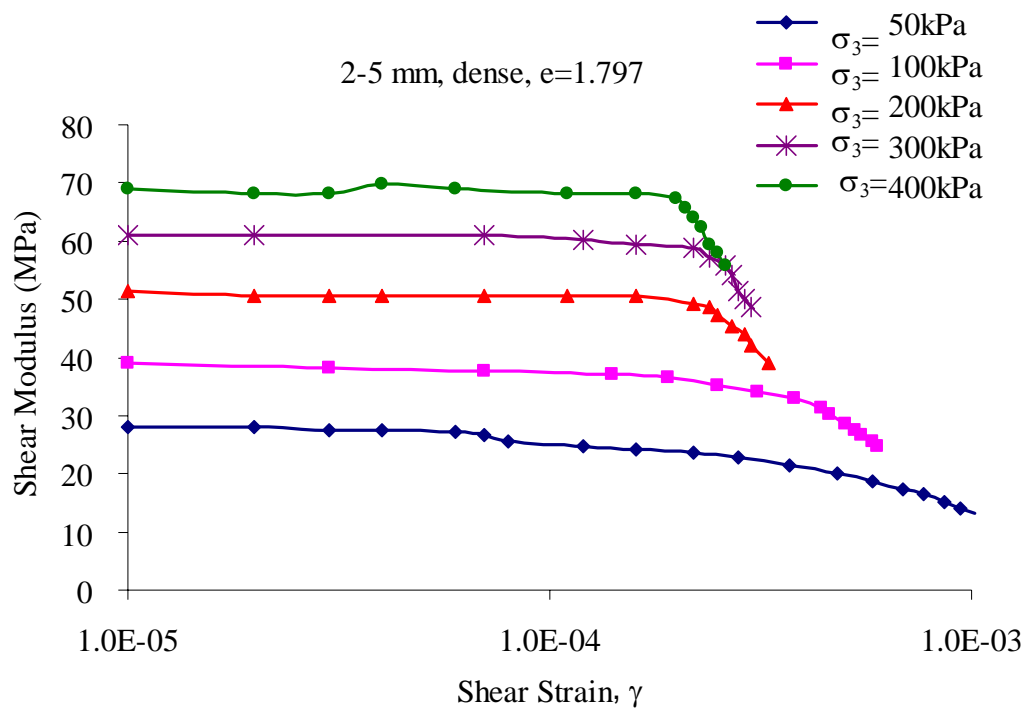


Figure 4.20. Shear Modulus Degradation with Shear Strain for a 2-5 mm Dense Silica Gel Sample under Different Confining Pressures

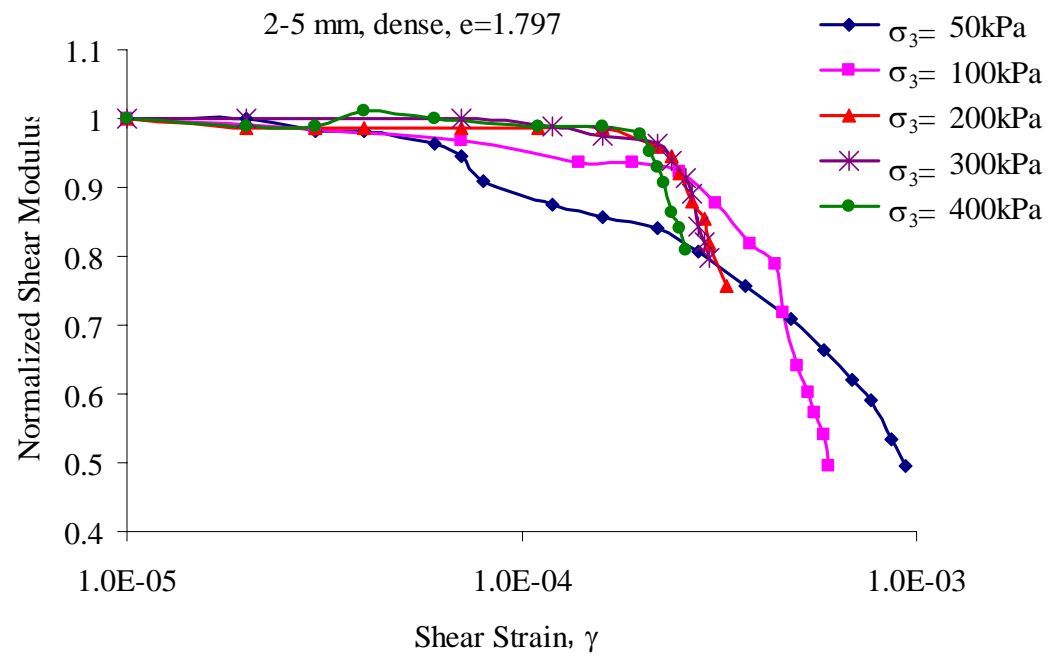


Figure 4.21. Normalized Shear Modulus Degradation with Shear Strain for a 2-5 mm Dense Silica Gel Sample under Different Confining Pressures

Figures 4.23 to 4.30 show the damping ratio variation with the shear strain. Even though the data are scattered, a general trend can still be observed. For both loose and dense silica gel specimens of different grain sizes, the damping ratio increases slowly at a low strain level and then increases quickly with increasing strain level. Investigations carried out by Seed and Idriss (1970), Hardin and Drnevich (1972a, b), and others have shown that the shear strain level and confining pressure are the main factors affecting the damping ratio behavior of sand. For a confining pressure greater than 24 kPa (500 psf), the effect of pressure is very small compared with the effect of shear strain. The same conclusions can be drawn for silica gel. For sand at the same strain level, increasing the confining pressure causes the damping ratio to decrease. However, for silica gel, an opposite trend was observed.

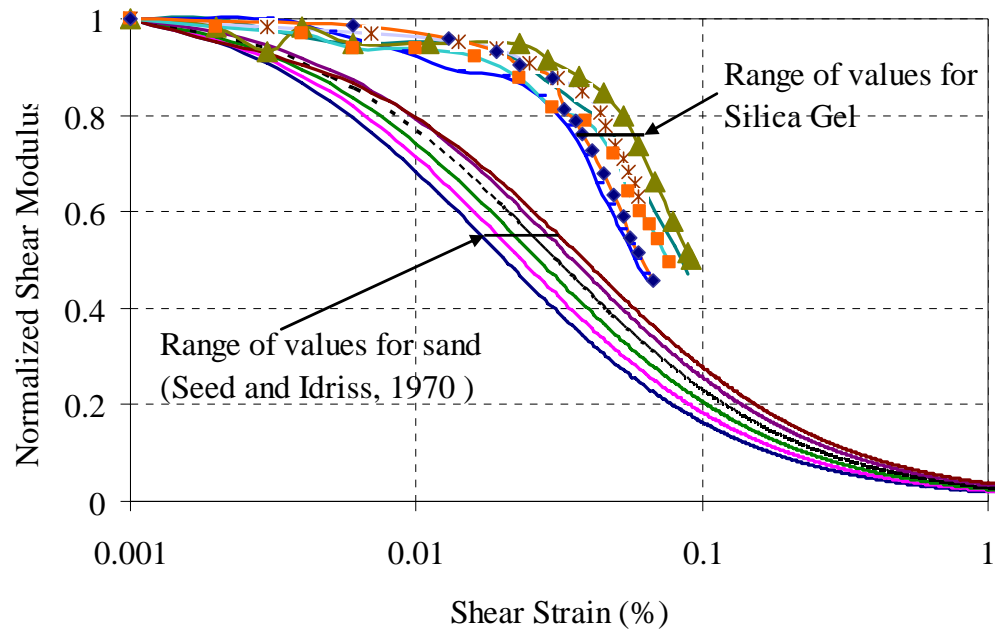


Figure 4.22. Variation of Shear Modulus for Sand and Silica Gel with Shear Strain at the Confining Pressure of 100 kPa

Damping is induced in sand due to the friction between the sand grains, viscous drag between the pore fluid and sand grains, and plastic deformation of the sand grains. The sand grains are very stiff and tend to keep their elasticity at a high confining pressure, and thus very little energy dissipates through plastic deformation. However, the silica gel grains are much easier to yield compared with sand grains as indicated by Iskander (1998). Under low confining stress, silica gel grains experience very small deformation; energy dissipates primarily through friction between the silica gel grains, and thus it displays similar damping behavior as sand. When the confining pressure becomes large, yielding of silica gel is the dominant energy dissipation mechanism, so silica gel exhibits a different damping behavior from sands. Dense specimens are more difficult to yield than the loose ones. Thus, an increase of the damping ratio for dense specimens was not as quick as that for the loose ones.

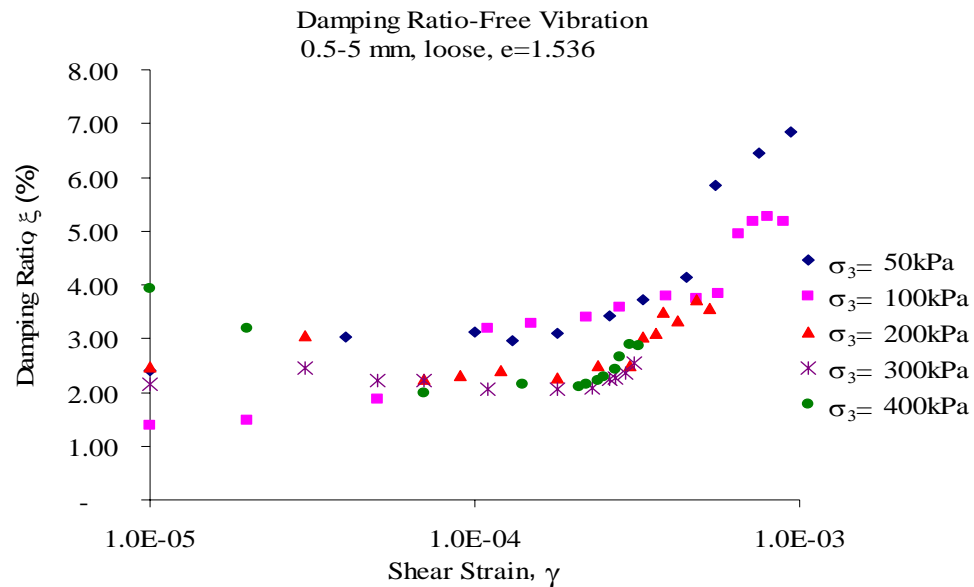


Figure 4.23. Damping Ratio Variation of 0.5-5 mm Loose Silica Gel with Shear Strain

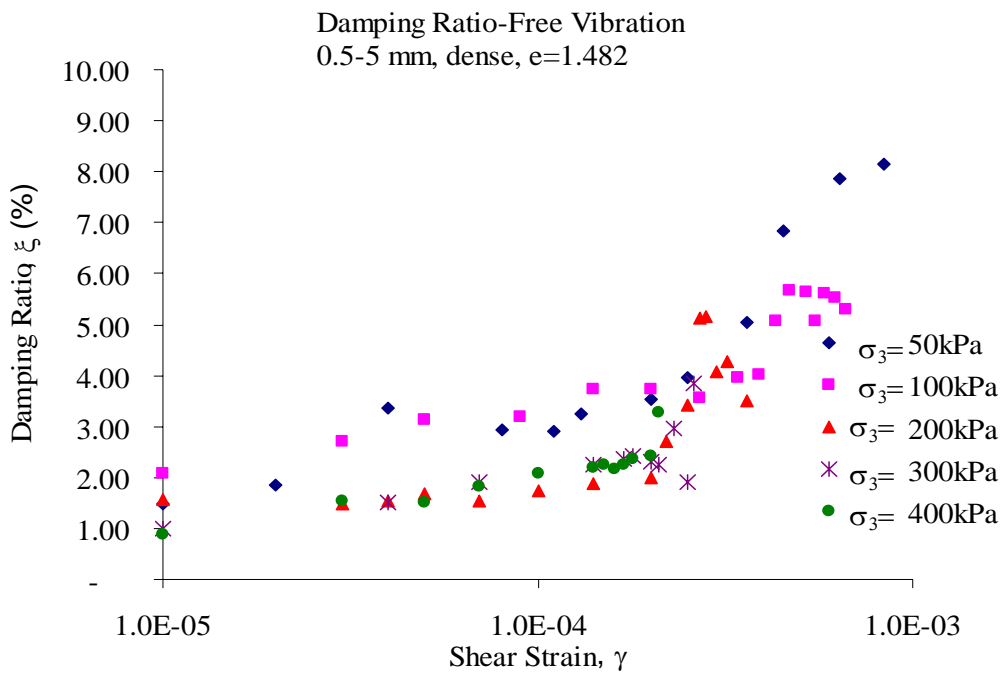


Figure 4.24. Damping Ratio Variation of 0.5-5 mm Dense Silica Gel with Shear Strain

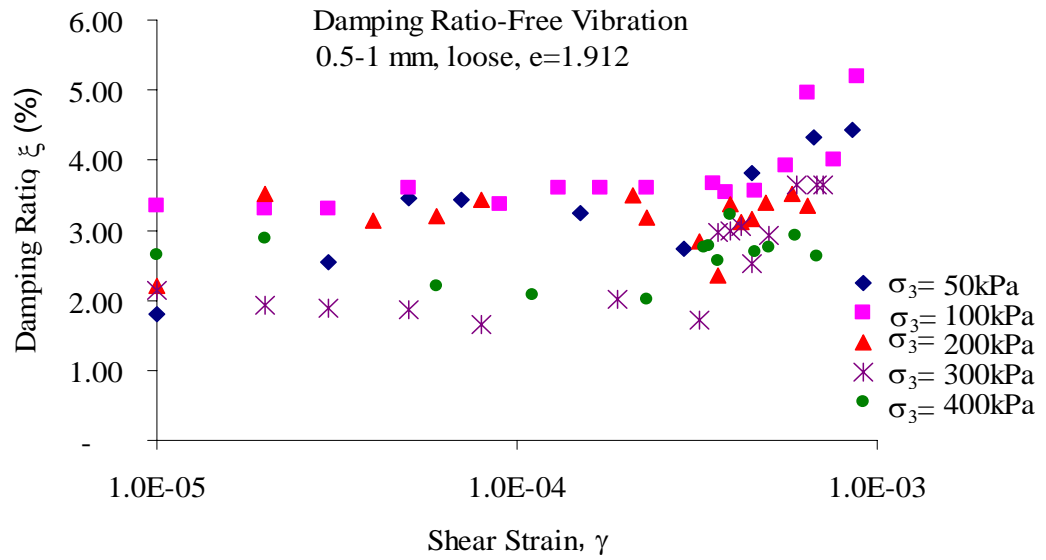


Figure 4.25. Damping Ratio Variation of 0.5-1 mm Loose Silica Gel with Shear Strain

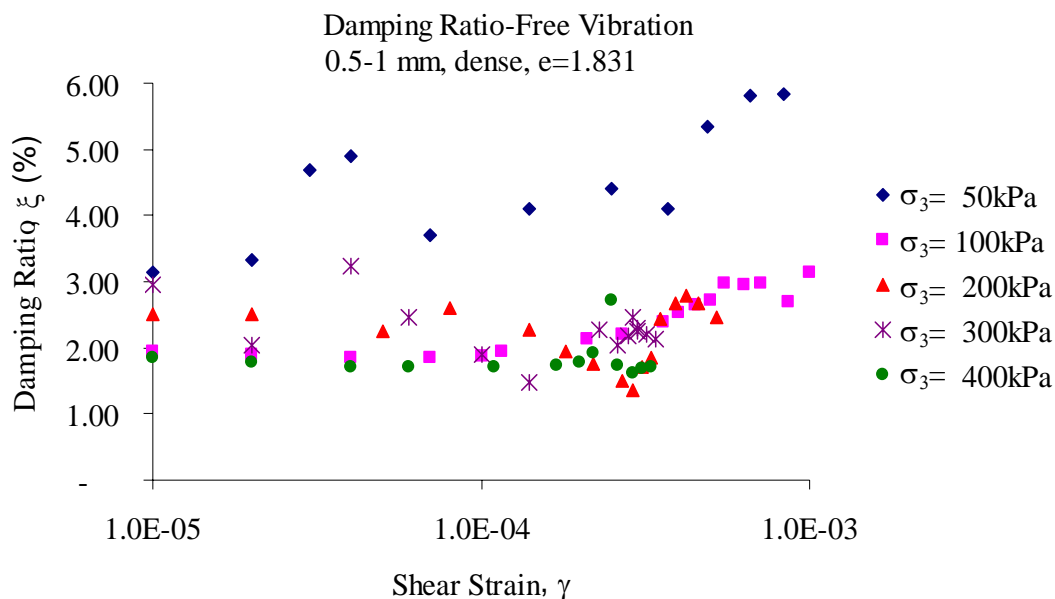


Figure 4.26. Damping Ratio Variation of 0.5-1 mm Dense Silica Gel with Shear Strain

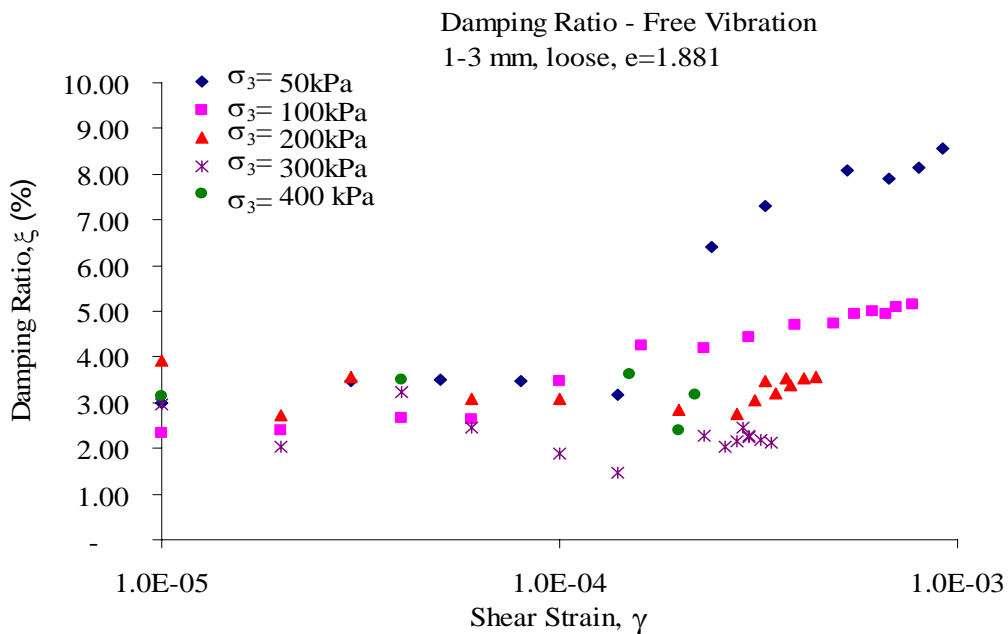


Figure 4.27. Damping Ratio Variation of 1-3 mm Loose Silica Gel with Shear Strain

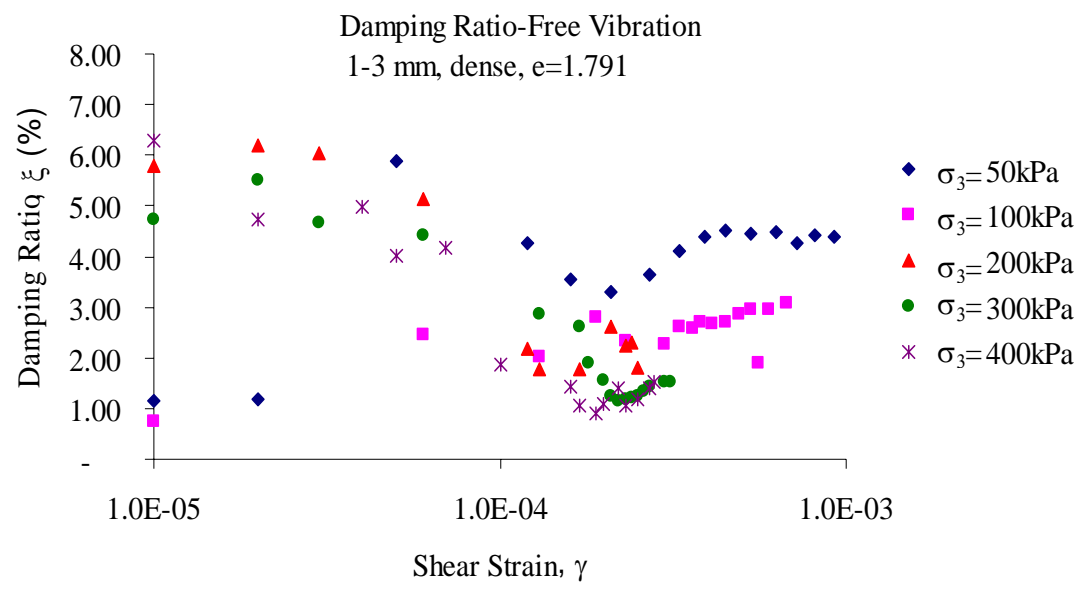


Figure 4.28. Damping Ratio Variation of 1-3 mm Dense Silica Gel with Shear Strain

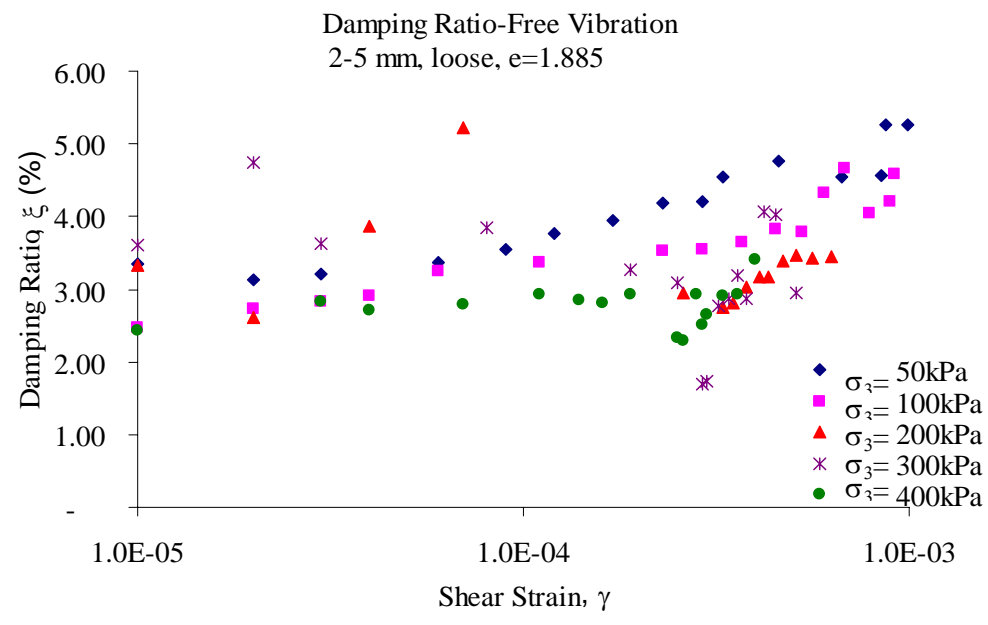


Figure 4.29. Damping Ratio Variation of 2-5 mm Loose Silica Gel with Shear Strain

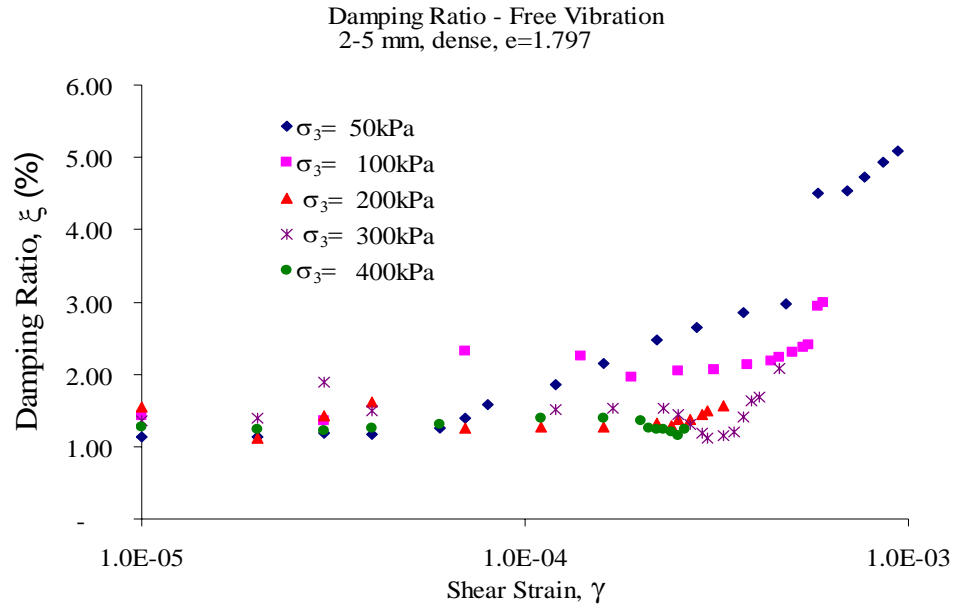


Figure 4.30. Damping Ratio Variation of 2-5 mm Dense Silica Gel with Shear Strain

4.4.3. Discussion on Damping Ratio Determination by the Half-Power Method and Free Vibration Method. In the GCTS resonant column device, two methods can be used to determine the damping ratio of a specimen— the free vibration and the half-power method. The free-vibration decay curve is obtained by turned off the excitation force after the specimen is vibrating steadily. The logarithmic decrement can be determined by Equation (4.2),

$$\delta = \frac{1}{n} \ln(z_i / z_{i+n}) \quad (4.2)$$

where z_i and z_{i+n} are the amplitudes of the decay curve at i cycle and $(i + n)$ cycles. The damping ratio, D , can be determined from δ by Equation (4.3)

$$D = [\delta^2 / (4\pi^2 + \delta^2)]^{1/2} \quad (4.3)$$

The half-power bandwidth method is based on measurement of the width of the dynamic response curve around the resonance peak. For small values of material damping, the damping can be estimated by Equation (4.4)

$$D = (f_2 - f_1) / 2f_r \quad (4.4)$$

where f_1 and f_2 are the two frequencies at which the amplitude is 0.707 times the amplitude at the resonant frequency, f_r .

To examine the effectiveness of the two methods, a comparison was made in this research. Figure 4.31 (a) through (e) illustrates the damping ratio determined from the two methods for a 0.5-5 mm loose silica gel specimen. When the shear strain is in the linear range (small strain range), the two methods give almost the same damping ratio data. However, the half-power method gives a higher damping ratio value than the free vibration method when the shear strain becomes nonlinear (large strain range).

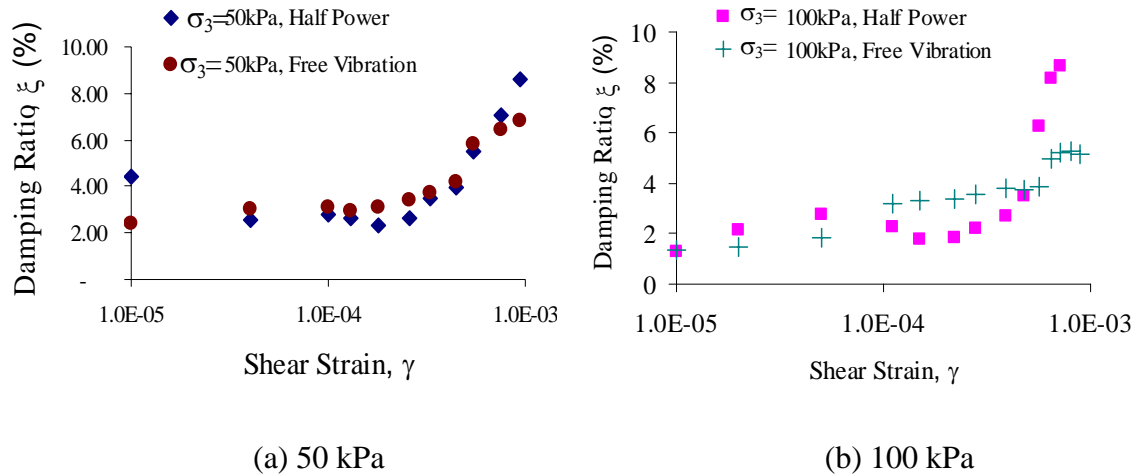


Figure 4.31. Damping Ratio versus Shear Strain for a 0.5-5 mm Loose Silica Gel Sample under Confining Pressures (a) 50 kPa, (b) 100 kPa, (c) 200 kPa, (d) 300 kPa, and (e) 400 kPa

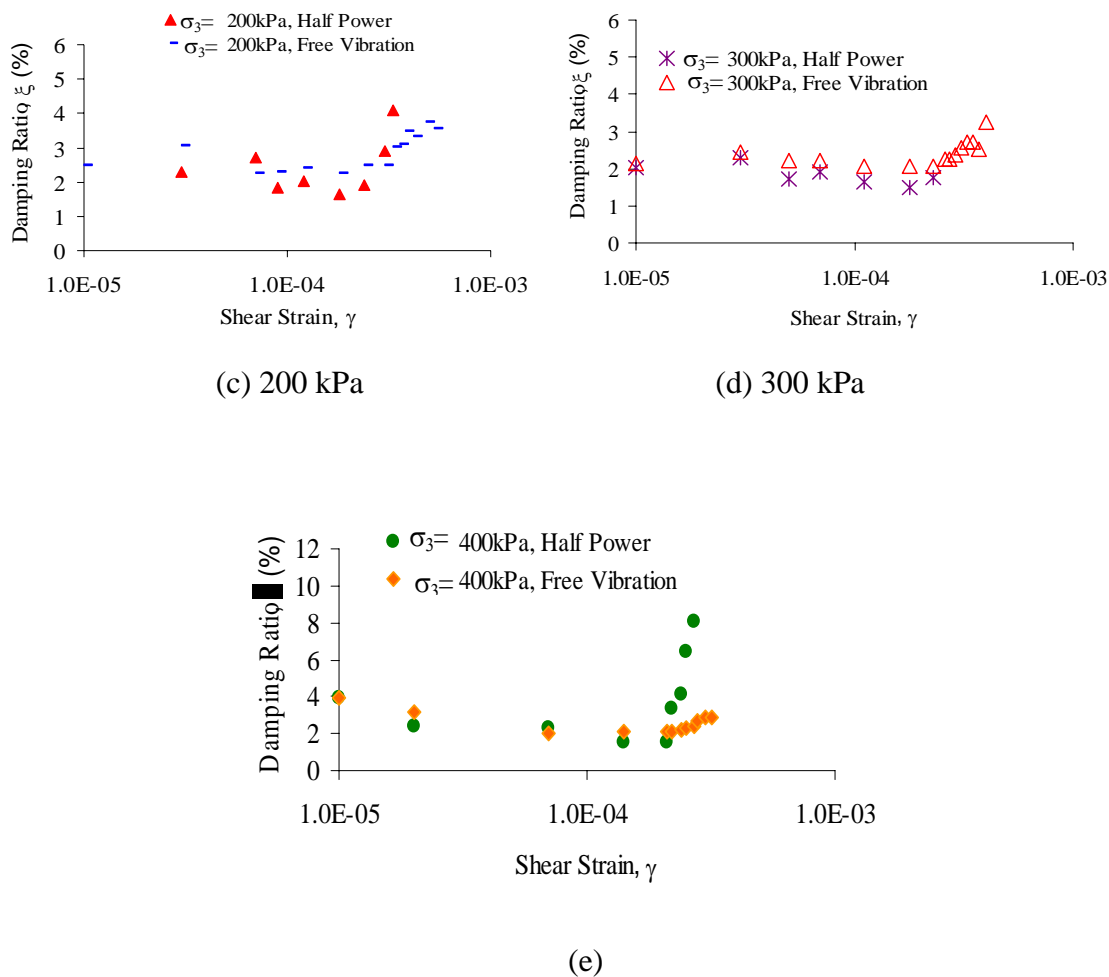


Figure 4.31. Damping Ratio versus Shear Strain for a 0.5-5 mm Loose Silica Gel Sample under Confining Pressures (a) 50 kPa, (b) 100 kPa, (c) 200 kPa, (d) 300 kPa, and (e) 400 kPa Cont'

4.5. SUMMARY

This section presented the dynamic properties of dry silica gel. Resonant column tests were conducted on both loose and dense dry silica gel specimens. It was observed that the shear modulus of silica gel was strongly influenced by the confining stress and the void ratio at a low strain level. The grain size had a secondary influence on the dynamic properties of the silica gel. The small-strain shear modulus of silica gel with a smaller void ratio was higher than that of silica gel with a large void ratio. However, once the confining pressure was higher than 400 kPa, silica gel tended to have a constant

small-strain shear modulus irrespective of the initial void ratio and confining pressure. By comparing the behavior of sand from the previous researcher's work, it was found that silica gel had a different dynamic behavior compared with sand. The maximum shear modulus of silica gel tended to slow its increase when the confining stress became higher. Normalized shear modulus variation with shear strain showed that the linear threshold shear strain, γ_{tl} , was greater for silica gel at low confining stress than at high confining stress, while sand exhibited the contrary behavior. The damping behavior of the silica gel was different from the damping behavior of sand. The damping ratio of silica gel increased with the increasing confining pressure, which was opposite to that of sand. The highly yielding characteristics of the silica gel grains might explain this behavior. This study also made a comparison of two different damping ratio determination method—the free vibration and half-power method. At the low strain level, the two methods gave consistent damping ratio data; however, the half-power method gave higher damping ratio data when the shear strain became higher. When using the half-power method to determine the damping ratio data, it was limited to the low strain level.

5. THE CAMERA CALIBRATION AND APPLICATION INTO PIV

5.1. INTRODUCTION

It has been reviewed in the literature that there are several methods currently available to carrying out the camera calibration. However, an alternative camera calibration method still needs to be developed to facilitate the measurement. In this paper, a neural network based calibration algorithm was proposed and examined by the calibration data. An application example of this calibration algorithm integrated with particle image velocimetry code-MatPIV (Sveen, J.K., 2004) was illustrated with a rectangular footing model.

5.2. CAMERA CALIBRATION DATA

The first task in calibration is to get a set of calibration data, $P(X, Y)$ and its corresponding image point, $p(u, v)$. To get these calibration control points, a calibration check board with white and black grids with known spacing was prepared. The calibration control points are the corner points of those grids. First, set up the calibration check board exactly the same plane the subject area located. Take the image of the check board, and then extract the corner points from the image using Harris' corner finder method (1998). Before doing the corner point extraction, the coordinate system in the object plane was set up first. Then the coordinates of images points $p(u, v)$ were obtained as well as control points in the object plane. Figure 5.1 shows the image of check board, and Figure 5.2 shows the extracted corners and the coordinates system in both object plane and image plane. This corner point extraction procedure was also used by Bouguet and Perona (1998).

5.3. THE NEURAL NETWORK CALIBRATION MODEL

The neural network trained in this study is a three-layer, feed-forward neural network (2– 15–2 NN). The input layer consists of $n_1 = 2$ input nodes, and the output layer consists of $n_2 = 2$ output nodes. The hidden layer consists of 15 neurons.

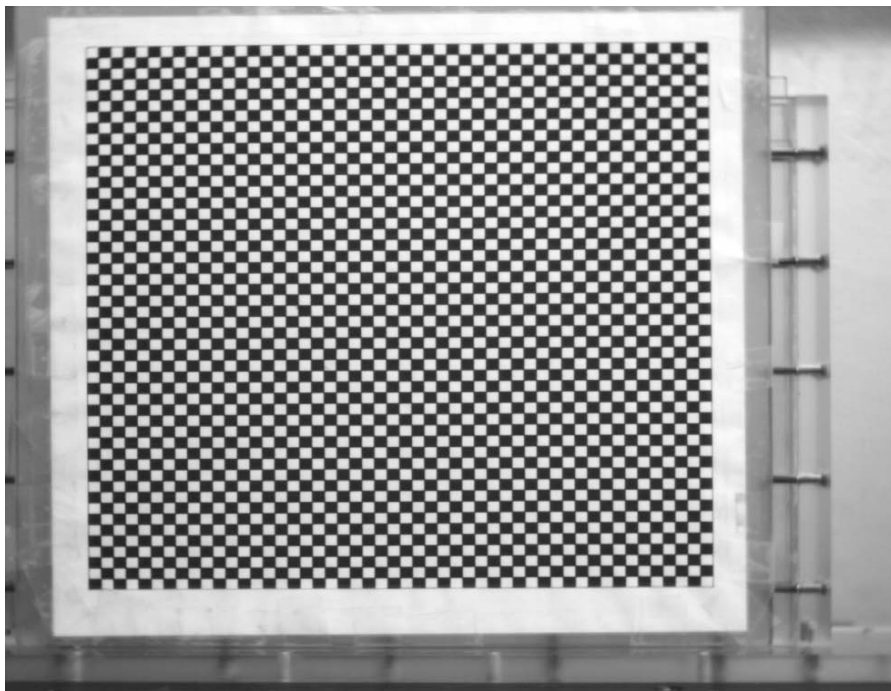


Figure 5.1. Camera Calibration Check Board with 2.5 mm Spacing Grids

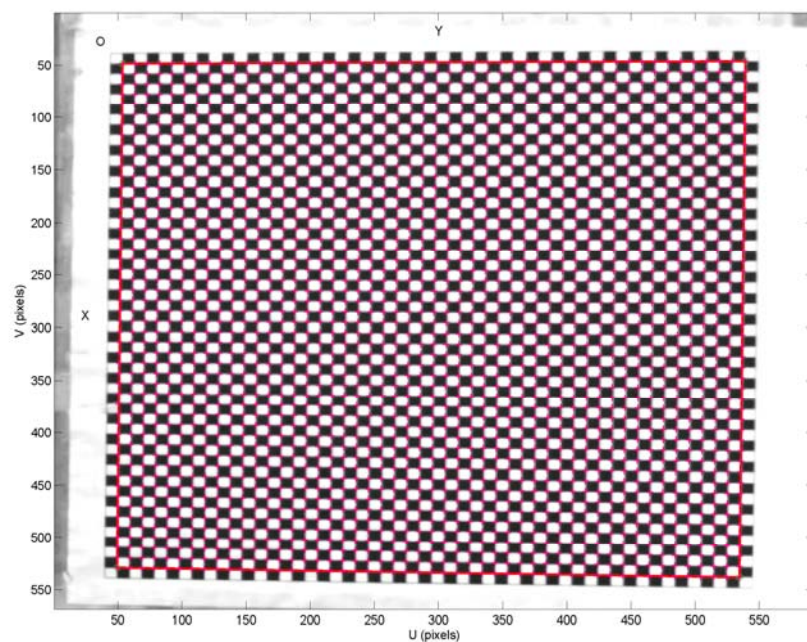


Figure 5.2. Corner Points Extraction and Coordinate Systems in the Object Plane and Image Plane

Input data are the image points $p(u,v)$ obtained from the corner points extraction. Target data were the corner points $P(X,Y)$ from the calibration plane. Training data were from half of the calibration points. The other half calibration data are used as testing data to test the neuron network. A total of 2500 data points were used in this study.

5.3.1 Training Function. The neural network training algorithm used is a backpropagation function, which updates weight and bias values according to Levenberg-Marquardt optimization method. In the training process, the input layer takes an input vector of size $n1 = 2$ and passes it to the hidden layer. Next, the hidden layer maps this input vector to a vector of size $n3 = 2$, by a tangent sigmoid transfer function $\text{tansig}(\zeta)$ as expressed in Equation (5.1):

$$a = \frac{2}{1 + e^{-2\zeta}} - 1 \quad (5.1)$$

where ζ is an activation function, the sum of the weighted inputs and biases. This vector from the hidden layer is then mapped by a pure linear transfer function to an output layer. The performance of the neural network model is defined by the normalized square error MSE, expressed as Equation (5.2):

$$MSE = \frac{1}{2QN} \sum_{q=1}^Q \sum_{h=1}^N (d_{qh} - x_{out,qh})^2 \quad (5.2)$$

where Q is the number of outputs; N is the total number of data sets; d_{qh} is the target data; $x_{out,qh}$ is the network output data. To determine the appropriate number of neurons in the hidden layer, different numbers of neurons (5, 10, 15, and 20) were tested. It was found that 15 neurons in the hidden layer gave the best performance.

5.3.2. The Neural Network Model Validation. The proposed neural network calibration model was verified through the testing data, which were not used in the training process. The maximum absolute residual error for X and Y coordinates are 0.011

mm and 0.014 mm respectively. The residual error for X and Y is shown in Figures 5.3 and 5.4, respectively.

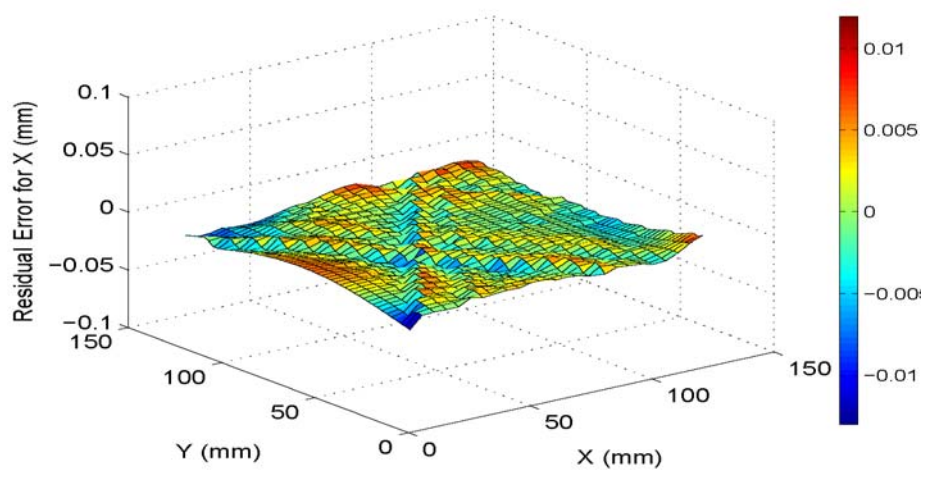


Figure 5.3. Residual Error for X from Neural Network Model

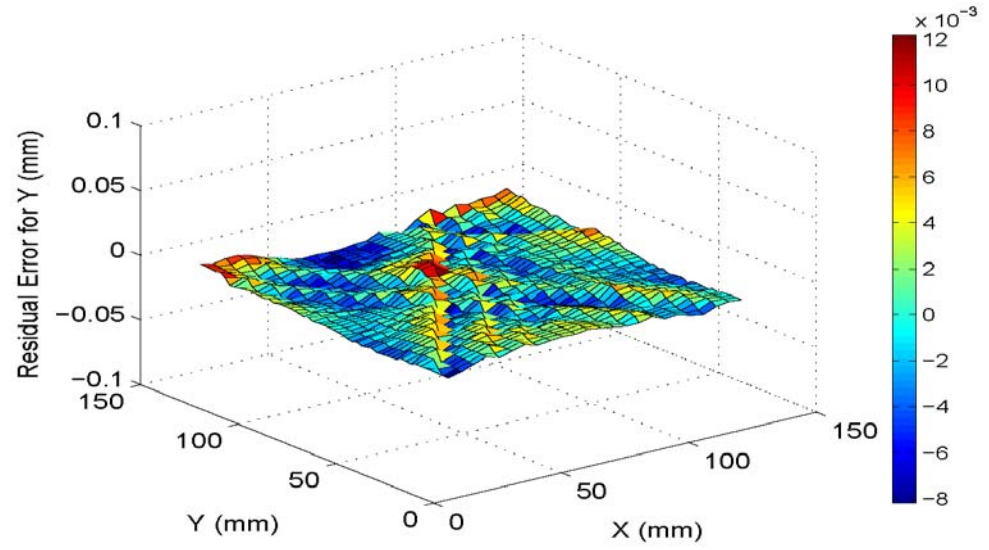


Figure 5.4. Residual Error for Y from Neural Network Model

5.4. COMPARISON OF DIFFERENT CALIBRATION MODELS

To examine the effectiveness of this neural network model, linear and second order polynomial calibration algorithms were also studied in this paper, which are expressed as in Equation (5.3) and Equation (5.4) follows.

$$\begin{cases} X = a_1 + a_2u + a_3v \\ Y = b_1 + b_2u + b_3v \end{cases} \quad (5.3)$$

$$\begin{cases} X = a_1 + a_2u + a_3v + a_4u^2 + a_5v^2 + a_6uv \\ Y = b_1 + b_2u + b_3v + b_4u^2 + b_5v^2 + b_6uv \end{cases} \quad (5.4)$$

where, X, Y are the coordinates of point P in the object plane, u, v are the coordinates of corresponding image points, p in the image plane, and a_i and b_i are the coefficient for these models. They were determined from the normalized least square method using the same training data as used for neural network model. These models were also tested using the same testing data. Figures 5.5, 5.6, 5.7, and 5.8 presented the residual error for the testing data from linear calibration and second order polynomial function. Maximum absolute residual error is 0.672 mm for X and 0.685 mm for Y from the linear calibration algorithm. Maximum absolute residual error is 0.030 mm for X and 0.032 mm for Y from second order polynomial algorithm. These values are much higher than those errors from the neural network calibration algorithm.

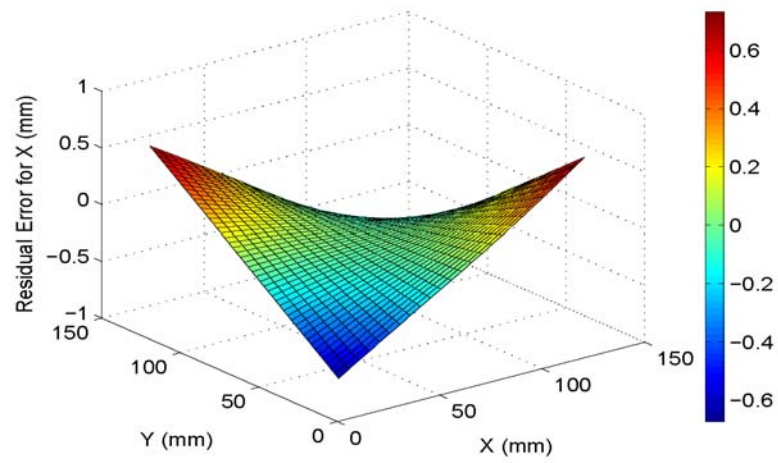


Figure 5.5. Residual Error for X from the Linear Calibration Model

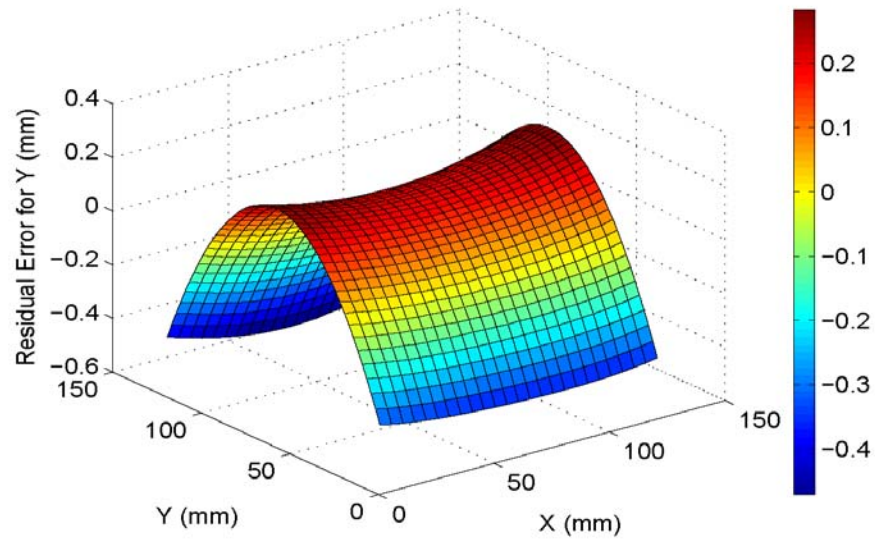


Figure 5.6. Residual Error for Y from the Linear Calibration Model

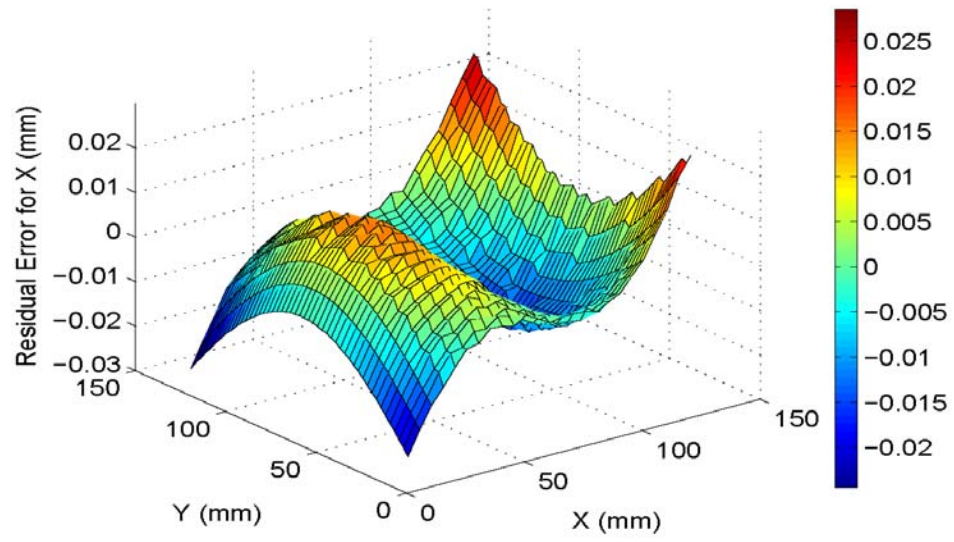


Figure 5.7. Residual Error for X from the Second-Order Polynomial Model

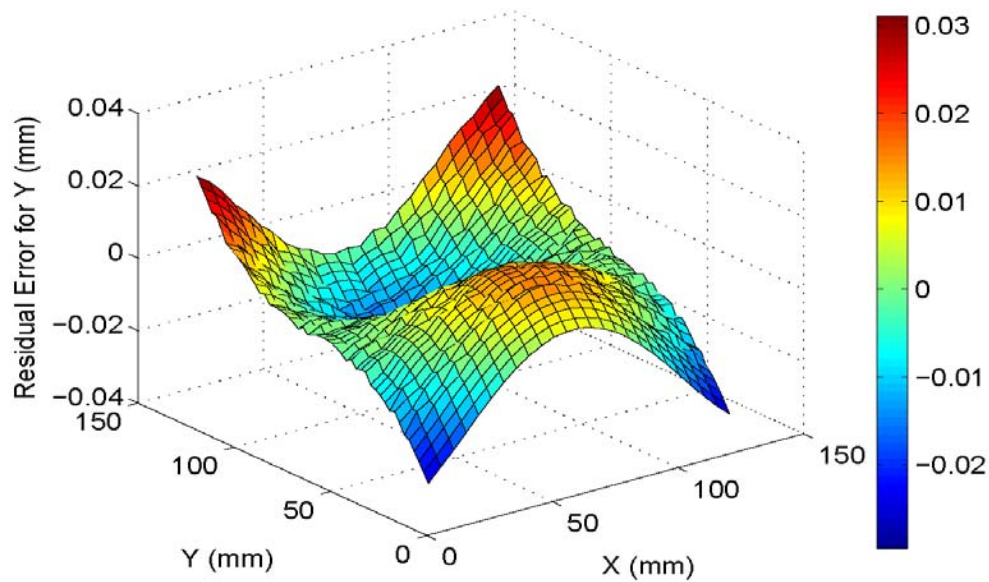


Figure 5.8. Residual Error for Y from the Second-Order Polynomial Model

5.5. THE ANGLE ERROR ANALYSIS

The effects of angle (θ) between the calibration plane and the image sensor plane on the residual error were also investigated in the research. The set up of this experiment is to let the calibration plane align closely to the image sensor plane first. Then rotate the calibration plane to a different angle (θ), as shown in Figure 5.9. Images of calibration plane were taken by the camera while keeping the position of the camera fixed during this process. Three different algorithms were carried on these images. The residual errors obtained are shown in Table 5.1. From Table 5.1, it is found that the linear algorithm gives the largest absolute residual error among the three different calibration algorithms. The second order polynomial is good when the angle is small, which implies the image sensor plane and calibration plane almost parallels to each other. However, the error increases with the angle becoming larger. Neural network calibration algorithm is found to perform the best, which gives the least absolute residual error and also the error does not change much with the angle increase.

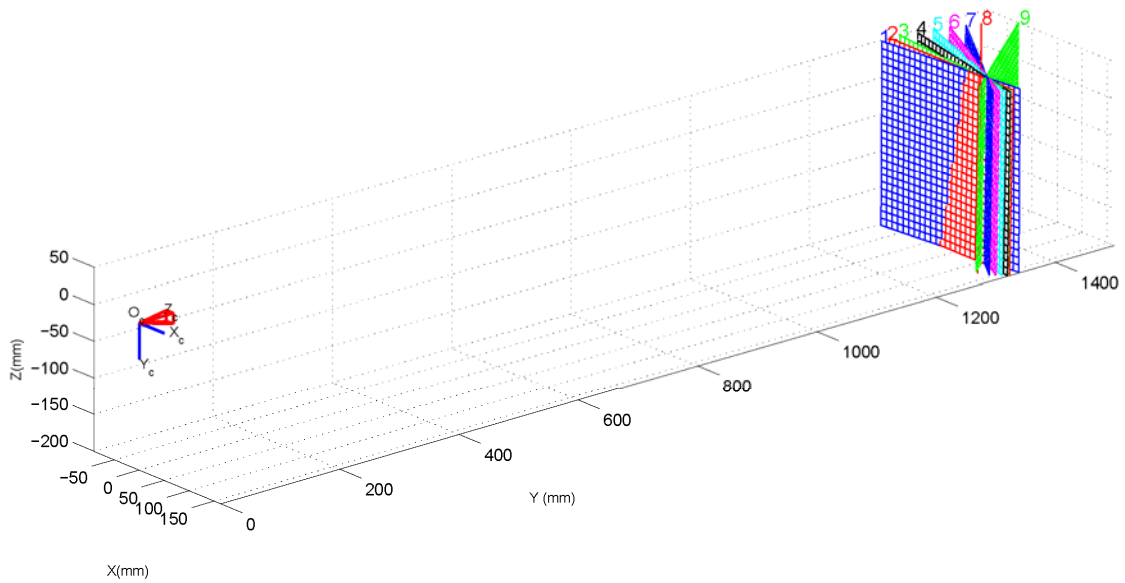


Figure 5.9. The Relative Position of Different Calibration Planes to the Image Plane (Z is the normal direction of the image plane)

Table 5.1. Absolute Error for Nine Planes from Three Calibration Algorithms

Angle $\theta(^{\circ})$	Maximum Absolute Residual Error		
	Linear (mm)	Second-Order (mm)	Neural Network (mm)
7.62	0.685	0.032	0.014
13.61	1.499	0.044	0.025
17.97	1.932	0.057	0.016
25.60	1.932	0.095	0.039
30.87	3.348	0.130	0.038
36.49	3.944	0.199	0.014
39.43	4.427	0.202	0.016
50.66	4.482	0.274	0.056
53.93	4.722	0.303	0.062

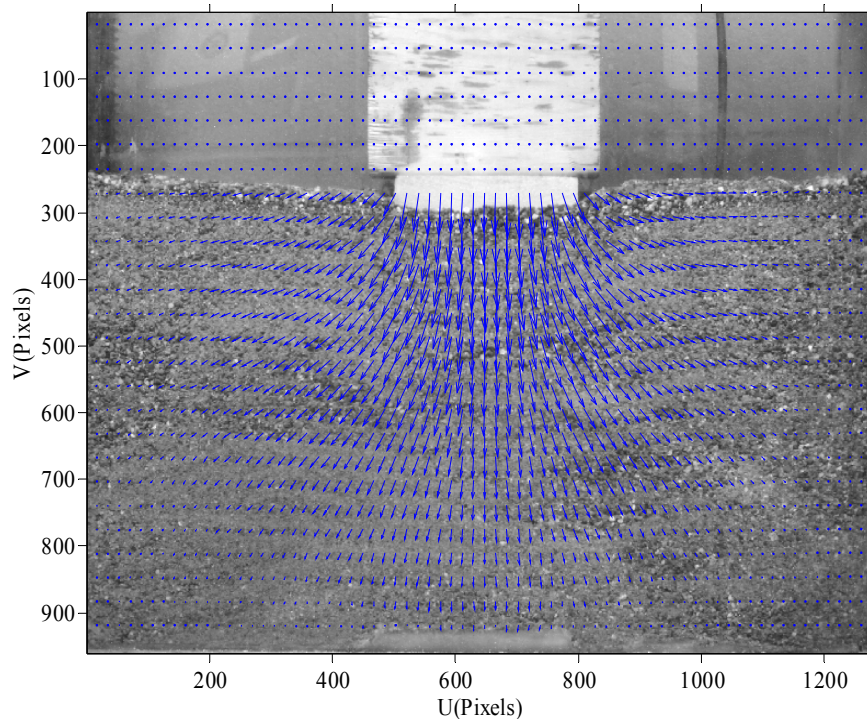
5.6. THE APPLICATION OF THE CALIBRATION IN THE PARTICLE IMAGE VELOCIMETRY

A small-scale wood block (6.35 cm × 7.62 cm × 15.88 cm) was placed on top of the sand in a model container (35.56 cm × 6.60 cm × 35.56 cm), as shown in Figure 5.10. The height of the sand was 18.92 cm (7.45 in.), and a loading frame was used to apply the vertical load to the foundation. The camera was set up to take images of the soil below the footing during the loading. The loading rate was set to 2.54 mm/min (0.1 in/min). The test setup is illustrated in Figure 5.11. A long steel plate was put on the loading platen of the frame, the sand box rested on the steel plate, and the digital camera was set about 2 m from the sand box at the other end of the steel plate. This setup ensured that the digital camera was moving together with the loading platen during the loading process. Images were taken every 30 seconds. The proposed neural network camera calibration algorithm was implemented into MatPIV, a computer code initially developed by Sveen (2004) for PIV, to process the images.

The digital image correlation method was used in MatPIV to analyze the two images to obtain the full-field deformation of the soil surrounding the footing. Figure 5.12 shows the displacement vector field of the soil under the footing at $t = 6$ min, and $P = 0.092$ kN(20.6 lb), Figure 5.13 shows the displacement contour of the sand, and Figure 5.14 shows the normal direction of the sand movement. It was clear that the maximum displacement happened beneath the center of the rectangular footing. The displacement of the soil reduces as the distance of the soil to the center of the footing increases from the center of the footing. It was estimated that the bearing capacity of the footing was 0.065 kN based on Terzaghi's theory (1943) (unit weight, $\gamma = 18.53$ kN/m³; cohesion, $c=0$; angle of friction, $\phi=31^\circ$). At $t = 6$ min, the applied load was already pass the ultimate bearing capacity of the footing. It is clear from Figure 5.13(a) and (b) that the deformation of the sand mass consisted of a triangular zone below the footing, two symmetrically distributed radial shear zones, and two triangular Rankine passive zones. The soil exhibited a failure mode similar to what described by Terzaghi's bearing capacity theory.

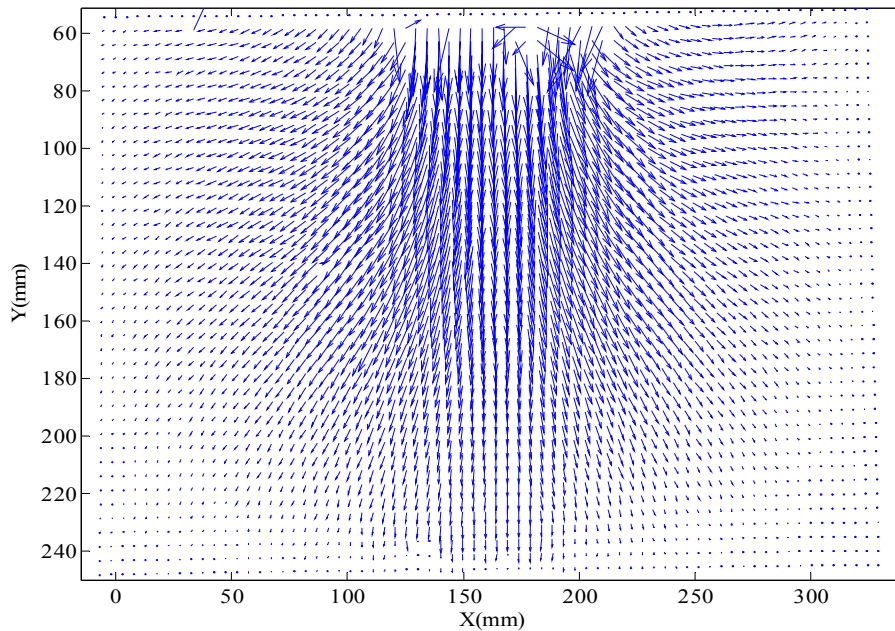


Figure 5.10. Experiment Setup for the Rectangular Footing



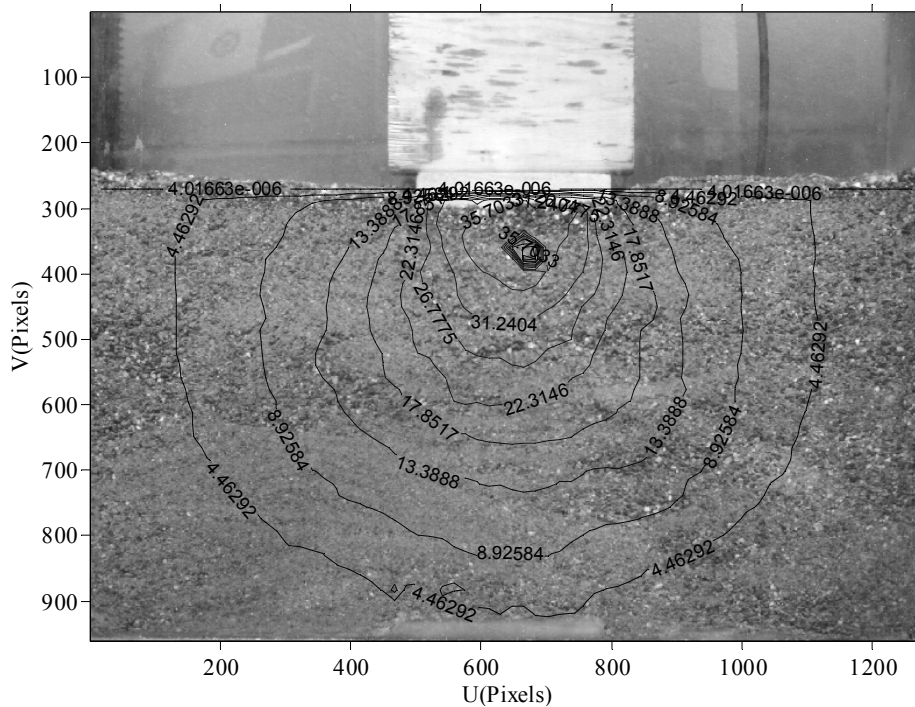
(a) In the Image Space

Figure 5.11. The Deformation Vector Field of Sand under the Rectangular Footing ($t = 6$ min, $P = 0.092$ kN)



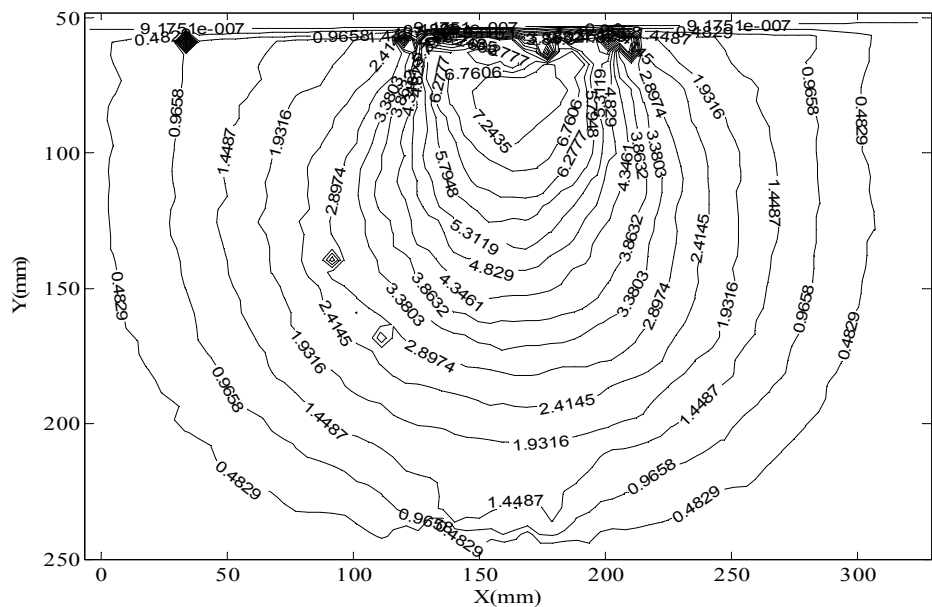
(b) In the Real Space

Figure. 5.11. The Deformation Vector Field of Sand under the Rectangular Footing (t = 6 min, P = 0.092 kN) Cont'



(a) In the Image Space (Contour Label in Unit of Pixels)

Figure 5.12. The Magnitude Contour of Displacement Vector for Sand under the Rectangular Footing (t=6 min, P = 0.092 kN)



(b) In the Real Space (Contour Label in Unit of mm)
Figure 5.12. The Magnitude Contour of Displacement Vector for Sand under the Rectangular Footing ($t = 6$ min, $P = 0.092$ kN) Cont'

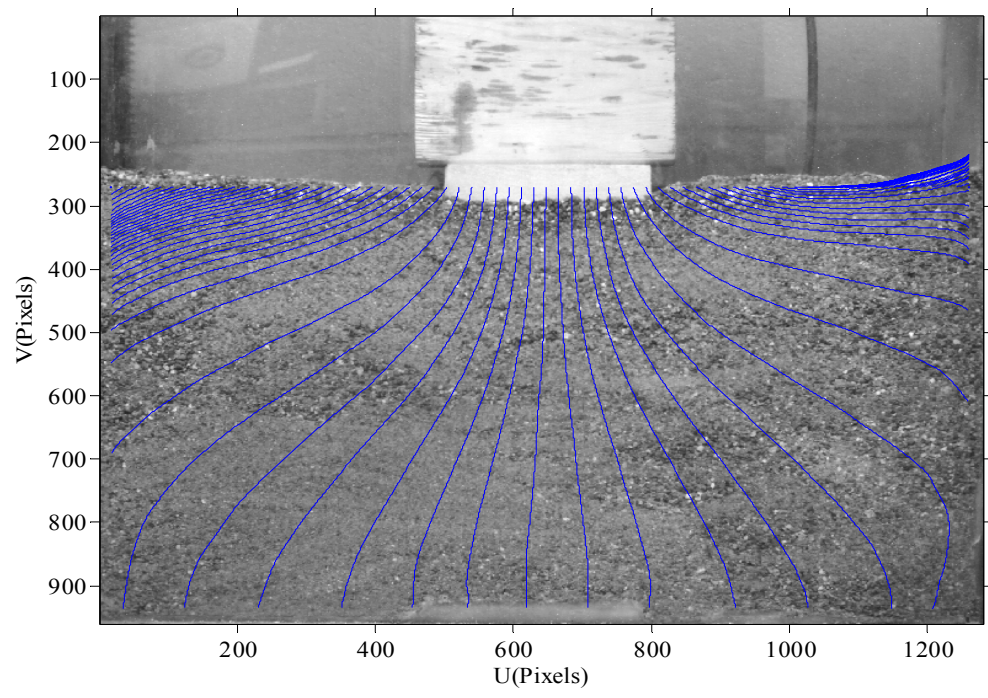


Figure 5.13. The Normal Direction of Flow Line for Sand Particles under the Rectangular Footing ($t = 6$ min, $P=0.092$ kN)

5.7. SUMMARY

The PIV technique was reviewed in this section. A three-layer back-propagation neuron network calibration algorithm was developed for the camera calibration in the image based measurement system. This algorithm was compared with the linear calibration and second-order polynomial calibration algorithm. When the angle between the image plane and object plane becomes large, linear calibration algorithm and second order polynomial calibration algorithm can give a considerable error. The neural network calibration model will give a very accurate result independent of the angle between the image plane and the object plane. This algorithm can be easily integrated with MatPIV to obtain the full-field deformation of the soil below the footing. This fast and accurate calibration method will greatly facilitate the image based measurement system into geomechanics application. This method can be extended to study the soil deformation under various loading conditions, such as pile under lateral loading, strip footing under vertical and lateral load, and the deformation of slope and embankment.

6. VISUALIZATION OF DYNAMIC RIGID-BLOCK AND SOIL INTERACTION

6.1. INTRODUCTION

In Section 1(Introduction), it has been made clear about the major object of the research was explained as visualization of the dynamic rigid-block and soil interaction through the use of transparent soil and PIV techniques. The transparent soil was studied in Section 3 and Section 4. The applicable PIV technique was reviewed and its calibration was studied in Section 5. In this section, the current research will be explained and included the shaking table test conducted to investigate dynamic rigid-block and soil interaction using transparent soil. PIV was used to obtain the behavior of the soil under simulated earthquake shaking. It is important to investigate in detail the motion mode of the rigid block and the soil during the dynamic event.

6.2. 1-G SHAKE TABLE TEST

When the prototype behavior is complex and difficult to understand, model tests are needed to study the prototype problem. In the model test, a small-scale model is introduced with the same boundary conditions as the prototype problem. Model tests can be used to understand the effects of different parameters and the process leading to the failure of the prototype at real time. There are two types of model tests-centrifuge tests and shaking table tests. Centrifuge tests are performed under high gravitation fields ($>1 g$). Shake table tests are performed under a normal gravitation field ($1 g$). Shaking table tests can control large amplitudes, multi-axis input motions and are convenient for experimental measurements. Shaking table tests have provided valuable research information about liquefaction, post-earthquake settlement, foundation response and lateral earth pressure problems. Soils can be placed, compacted in the model and instrumentation is relatively easy to set up in a shaking table test. In the following section, the similitude law for the shake table test, the model container, the shake table system, the rigid-block model, the transparent soil model, test setup, test program, and test results analysis are presented.

6.2.1. The Similitude Law for the Shake Table Test. The relationship between a scale model and the corresponding prototype behavior is described by a theory of scale model similitude. In general, the similitude is needed to interpret the test results of the model tests related with the prototype behavior. The available methods to determine the similitude ratio are dimensional analysis, similitude theory, and the method of governing equations. In dimensional analysis, a dimensionally homogeneous equation containing physical quantities is converted into an equivalent equation consisting of dimensionless products of powers of the physical quantities. Dimensional analysis maybe used to understand the form of the solution without application to the scale modeling. The similitude theory identifies the operating variables in a system and applies the dimensional analysis to construct and equate dimensionless terms for the model and the prototype. The method of governing equations involves the transformation of the differential equations describing the system into a nondimensional form, and the formation of similarity variables which relate the model to the prototype. In order to achieve the same boundary restriction, similarity variables must also be determined for both initial and boundary conditions on the system. Langharr (1951) defined the scale model as the one that has geometric, kinematic, or dynamic similarity to the prototype. Geometric similarity defines a model having the same ratio in terms of the physical dimensions as the prototype. Kinematic similarity satisfies a model and a prototype with homologous particles, at homologous points, at homologous times. Dynamic similarity requires a model and a prototype with homologous parts subjected to homologous net forces. Based on the different degree of similarity, a model can be described as “true”, “adequate”, or “distorted”. A true model fully satisfies all similitude requirements. An adequate model only meets the primary requirements of the similitude requirements. A distorted model deviates from the similitude requirements, and thus the prediction equation is distorted, or compensating distortions are introduced in other dimensionless products in order to preserve the prediction equation.

Iai (1989) derived a similitude law for the shaking table tests on a saturated soil-structure-fluid model in a 1 *g* gravitational field. His derivation was based on the basic equilibrium and the mass balance equations of soil skeleton, pore water, pile and sheet pile structures, and external waters. He adopted the basic equilibrium equations for the

saturated soil given by Zienkiewicz et al. (1990). The behavior of water was governed by the equations given by Lamb (1932). The equations for structures were either for the solid or for the beam. In addition, he also assumed that the stress-strain relation was determined irrespective of the confining pressure, if appropriate scaling factors are introduced for the stress and the strain, taking the effect of the confining pressure into account. Table 6.1 list the general similitude for models tests in 1 g gravitational field and Table 6.2 list the special case for $\lambda_\rho = 1$ and $\lambda_\varepsilon = \lambda^{0.5}$.

Table 6.1. The Similitude Law for Model Tests in 1 g Gravitational Field

Items	Scaling factors (prototype/model)
x length	λ
ρ density of saturated soil	λ_ρ
ε strain of soil	λ_ε
t time	$(\lambda\lambda_\varepsilon)^{0.5}$
ε^0 strain of soil due to creep, temperature, etc.	λ_ε
σ total stress of soil	$\lambda\lambda_\rho$
σ' effective stress of soil	$\lambda\lambda_\rho$
D tangent modulus of soil, which generally depends on histories of effective stress, strain, etc.	$\lambda\lambda_\rho / \lambda_\varepsilon$
K_s bulk modulus of the solid grain of soil	$\lambda\lambda_\rho / \lambda_\varepsilon$
p pressure of pore water and/or external water	$\lambda\lambda_\rho$
k permeability of soil	$(\lambda\lambda_\varepsilon)^{0.5} / \lambda_\rho$
u displacement of soil and/or structure	$\lambda\lambda_\varepsilon$
\dot{u} velocity of soil and/or structure	$(\lambda\lambda_\varepsilon)^{0.5}$
\ddot{u} acceleration of soil and/or structure	1
w average displacement of pore water relative to the soil skeleton	$\lambda\lambda_\varepsilon$
\dot{w} rate of pore water flow	$(\lambda\lambda_\varepsilon)^{0.5}$
n porosity of soil	1
K_f bulk modulus of pore water and/or external water	$\lambda\lambda_\rho / \lambda_\varepsilon$
EI flexural rigidity (per unit breadth of the beam)	$\lambda^4\lambda_\rho / \lambda_\varepsilon$
EA longitudinal rigidity (per unit breadth of the beam)	$\lambda^2\lambda_\rho / \lambda_\varepsilon$
θ inclination of the beam	λ_ε

Table 6.1. The Similitude Law for Model Tests in 1 g Gravitational Field Cont'

M bending moment of the beam (per unit breadth of the beam)	$\lambda^3 \lambda_\rho$
S shear force of the beam (per unit breadth of the beam)	$\lambda^2 \lambda_\rho$
F axial force of the beam (per unit breadth of the beam)	$\lambda^2 \lambda_\rho$
ρ_i density of pore water and/or external water	λ_ρ
ρ_b density of the beam (mass per unit length and breadth of the beam)	$\lambda \lambda_\rho$
\bar{T} traction acting on the soil specified on the boundary	$\lambda \lambda_\rho$
\bar{u} displacement of the soil and/or the beam specified on the boundary	$\lambda \lambda_\varepsilon$
\bar{w} average displacement of pore water, specified on the boundary, relative to the soil skeleton, often specified as rate of flow on the boundary	$\lambda \lambda_\varepsilon$
$\bar{\theta}$ inclination of the beam specified at the boundary	λ_ε
\bar{M} bending moment of the beam specified at the boundary (per unit breadth of the beam)	$\lambda^3 \lambda_\rho$
\bar{S} shear force of the beam specified at the boundary (per unit breadth of the beam)	$\lambda^2 \lambda_\rho$
\bar{F} axial force of the beam specified at the boundary (per unit breadth of the beam)	$\lambda^2 \lambda_\rho$
\bar{i} hydraulic gradient of external water specified at the boundary	λ_ρ

Table 6.2. Similitude for Model Tests in 1 g Gravitational Field in the Special Case in which $\lambda_\rho = 1$ and $\lambda_\varepsilon = \lambda^{0.5}$

Items	Scaling factors (prototype/model)
x length	λ
ρ density of saturated soil	1
ε strain of soil	$\lambda^{0.5}$
t time	$\lambda^{0.75}$
ε^0 strain of soil due to creep, temperature, etc.	$\lambda^{0.5}$
σ total stress of soil	λ
σ' effective stress of soil	λ
D tangent modulus of soil, which generally depends on histories of effective stress, strain, etc.	$\lambda^{0.5}$
K_s bulk modulus of the solid grain of soil	$\lambda^{0.5}$
p pressure of pore water and/or external water	λ
k permeability of soil	$\lambda^{0.75}$
u displacement of soil and/or structure	$\lambda^{1.5}$
\dot{u} velocity of soil and/or structure	$\lambda^{0.75}$
\ddot{u} acceleration of soil and/or structure	1

Table 6.2. Similitude for Model Tests in 1 g Gravitational Field in the Special Case
in which $\lambda_\rho = 1$ and $\lambda_g = \lambda^{0.5}$ Cont'

w average displacement of pore water relative to the soil skeleton	$\lambda^{1.5}$
\dot{w} rate of pore water flow	$\lambda^{0.75}$
n porosity of soil	1
K_f bulk modulus of pore water and/or external water	$\lambda^{0.5}$
EI flexural rigidity (per unit breadth of the beam)	$\lambda^{3.5}$
EA longitudinal rigidity (per unit breadth of the beam)	$\lambda^{1.5}$
θ inclination of the beam	$\lambda^{0.5}$
M bending moment of the beam (per unit breadth of the beam)	λ^3
S shear force of the beam (per unit breadth of the beam)	λ
F axial force of the beam (per unit breadth of the beam)	λ^2
ρ_t density of pore water and/or external water	1
ρ_b density of the beam (mass per unit length and breadth of the beam)	λ
\bar{T} traction acting on the soil specified on the boundary	λ
\bar{u} displacement of the soil and/or the beam specified on the boundary	$\lambda^{1.5}$
\bar{p} pressure of pore water and/or external water on the boundary	λ
\bar{w} average displacement of pore water, specified on the boundary, relative to the soil skeleton, often specified as rate of flow on the boundary	$\lambda^{1.5}$
$\bar{\theta}$ inclination of the beam specified at the boundary	$\lambda^{0.5}$
\bar{M} bending moment of the beam specified at the boundary (per unit breadth of the beam)	λ^3
\bar{S} shear force of the beam specified at the boundary (per unit breadth of the beam)	λ^2
\bar{F} axial force of the beam specified at the boundary (per unit breadth of the beam)	λ^2
\bar{i} hydraulic gradient of external water specified at the boundary	1

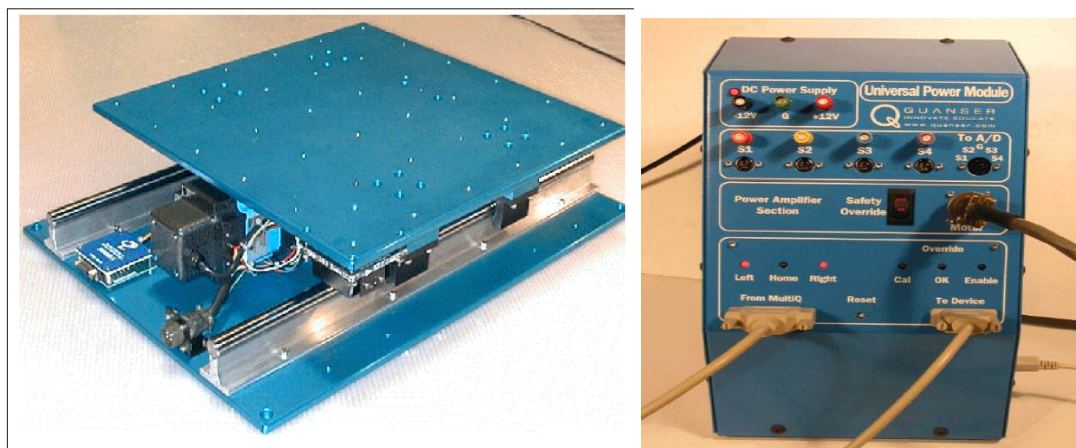
Wartman (1996) derived a similitude for 1-g shaking table tests based on the theory of the dimensional analysis which is shown in Table 6.3. In his research, he conducted extensive investigation of the effects of fly ash on the geotechnical properties of the model clay soil. The artificial material made of kaolinite, bentonite and type C fly ash was then used to investigate the pile response under two-directional lateral loading.

Table 6.3. Scaling Relations for Primary Soil Properties

Items	Scaling factor
ρ mass density	1
F force	λ^3
EI stiffness	λ^2
E Modulus	λ
a acceleration	1
V_s shear wave velocity	$\lambda^{1/2}$
t time	$\lambda^{1/2}$
f frequency	$\lambda^{-1/2}$
l length	λ
σ stress	λ
ε strain	1

6.2.2. The Model Container. A small-scale glass container was manufactured for the shaking table test. The glass material was used because of the corrosion properties of the solvent used in manufacturing the transparent soils. The container was fixed to the shaking table. The internal dimension of the container was 7.62 cm (3 inch) wide, 35.56 cm (14 inch) long and 30.48 cm (12 inch) tall. The thickness for the wall of the container is 0.635 cm (0.25 inch). A special sealant was used to seal the junction parts of the container to prevent leaking of the pore fluid.

6.2.3. The Shake Table System. The shaking table system used in this research is UCIST Shake Table from Quanser Consulting Inc. It consists of a shake table, a power module to drive the shaker table, a data acquisition board to collect data and drive the power amplifier, a microcontroller based safety circuit with safety limits and auto-calibration built into the power module, a portable pendant controller which can generate 4 pre-programmed earthquakes and a function generator as well as other data download to it. The whole shake table system was shown in Figure 6.1. The shake table consists of a 1 Hp brushless servo motor driving a 1.27 cm (0.5 inch) lead screw. The lead screw drives a circulating ball nut which is coupled to the 45.72 cm x 45.72 cm (18" x 18") table. The table itself slides smoothly on the low friction linear ball bearings on two ground hardened shafts. The specification for the shake table was shown in Table 6.4.



(a) The Shake Table

(b) The Power model

Figure 6.1. The UCIST Shake Table System

Table 6.4. Shake Table Specifications

Parameter	Value	Units
Table dimensions	18 x 18	Inches
Maximum payload	33	Lbs
Operational bandwidth	20	Hz
Peak velocity	33	Inch/sec
Ball screw efficiency	90	%
Maximum force	158	Lbs(force)
Peak acceleration	2.5	g
Stroke	± 3	Inches
Weight	60	Lbs
Encoder/ Leadscrew resolution	0.000125	Inches
Motor maximum torque	1.65	Nm
Ball nut dynamic loading capacity	2698	Lbs(force)
Ball nut life expectancy at full load	25e9	Inches
Linear bearing life expectancy	25e7	Inches
Linear bearing load carrying capability	290	Lbs

6.2.4. The Rigid-Block Model. A wood block was adopted in this research as the rigid-block model. The dimension of the wood block is 3.81 cm x 3.81 cm x 15.24 cm (1.5 in. x 1.5 in. x 6 in.). The total mass of the wood block is 122.95 g. Its density is 0.555 g/cm³. The wood block is illustrated in Figure 6.2. The toppling angle $\phi = 14^\circ$. It's a

type of slender rigid block. The wood block was chosen based on the scale law given by Wartman(1996). The corresponding prototype model is a typical residential building (8-story high). The scale ratio λ is 150. The corresponding density scaled down was estimated to be 0.5 g/cm^3 by assuming that the building is a typical reinforce concrete building.

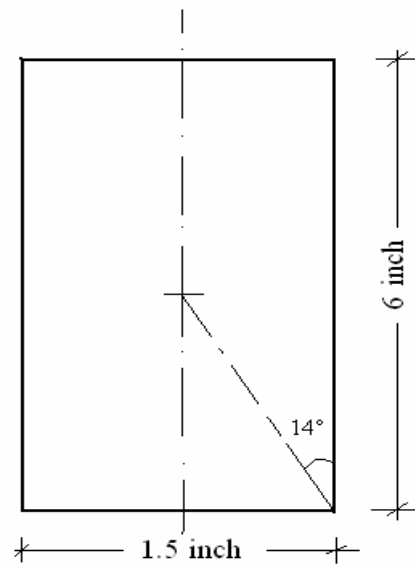


Figure 6.2. Dimensions of the Rigid Wood Block
(The toppling angle $\phi=14^\circ$)

6.2.5. The Transparent Soil Model. The transparent soil model used in this research was manufactured by mixing the 1-3 mm diameter dry silica gel and the pore fluid of 2 Propanol and Toluene. The unit weight of the transparent soil is 13 kN/m^3 . The total height of the transparent soil model is 13.335 cm (5.25 inch). The transparent soil was compacted for each layer of 30 mm with a light weight hammer. This compaction also helps to reduce the air bubble entrapped in the transparent soil.

6.2.6. The Shake Table Test Setup. The transparent soil model with the container was sitting on the shaking table and firmly confined between two wood blocks

fixed to the shaking table. The shaking motion from the shaking table container was transferred to the soil model through the shaking table container and then propagated upward through the bottom of the transparent soil to the soil surface. A high speed digital camera Troubleshoot 250 from Fastec with a resolution of 640 x 480 pixels was used to capture the images of the transparent soil model. The complete testing system setup is shown in Figure 6.3.

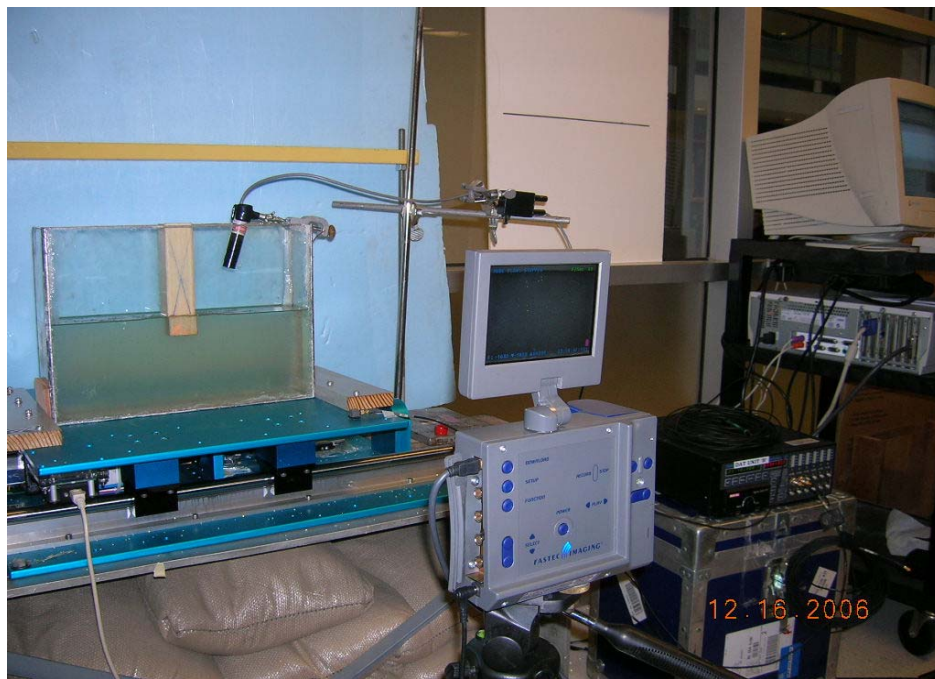


Figure 6.3. The Shake Table Test Setup for the Rigid-Block and Soil Interaction

6.2.7. The Shake Table Test Program. Three shake table tests were performed in this research. The first shake table test was designed to investigate the accuracy of the PIV technique. The second shake table test was aimed to investigate the free field motion of the transparent soil model. The third shake table test program was designed to investigate the rigid-block and transparent soil interaction.

6.2.7.1. Examination of the PIV algorithm. There is a concern about how accurate the PIV technique can capture the motion of the soil particles. To answer this question, the first shaking table test was set up to check the accuracy of the PIV technique. A transparent soil model was set up with several aluminum mark points embedded into the soil. Seven aluminum balls were identified as the mark points. The aluminum mark ball has the density close to that of silica gel. The motion of the mark points with time was tracked through tracking the position of the mark points in each image, and the displacement data at the mark points obtained from the PIV analysis were compared with the tracking data. The tracking data was obtained from each image using Matlab image processing technique. The testing setup was shown in Figure 6.4. A 1.5 Hz sinusoidal wave with 0.635 cm (0.25 inch) amplitude was input to the shaking table. The camera frame rate was set 30 frames/second. The comparison of the tracking data and the PIV data for tracking points A, B, C, D, E, F, and G were shown in Figure 6.5. It was clear that the PIV data and the tracking data are very close to each other for points A, B, C, D, and E. The PIV data is a little bit off from the tracking data for points F and G. This might be caused by the low quality of image surrounding the area of F and G. From this comparison, it can be concluded that PIV can closely capture the motion of the soil particles. Therefore, PIV tracking algorithm can be used to study the motion of soil during the shaking event effectively. In the MatPIV code, the displacement was calculated between the subsequent two images. In order to track the displacement of the same small patch of the soil, a slight modification was made in the program. The calculation was performed between the image obtained at time t_0 and the image obtained at any other time t_i . It was found out that the sub-window size used in the research was dependent on the largest displacement that the particles might have in the test. The sub-window should be able to cover the maximum displacement of the soil particles. For example, the particle has moved 10 pixels in both direction, the smallest sub-window size is required to be no smaller than 10 pixels. Otherwise, there is no matching image pattern found. The data is invalid.

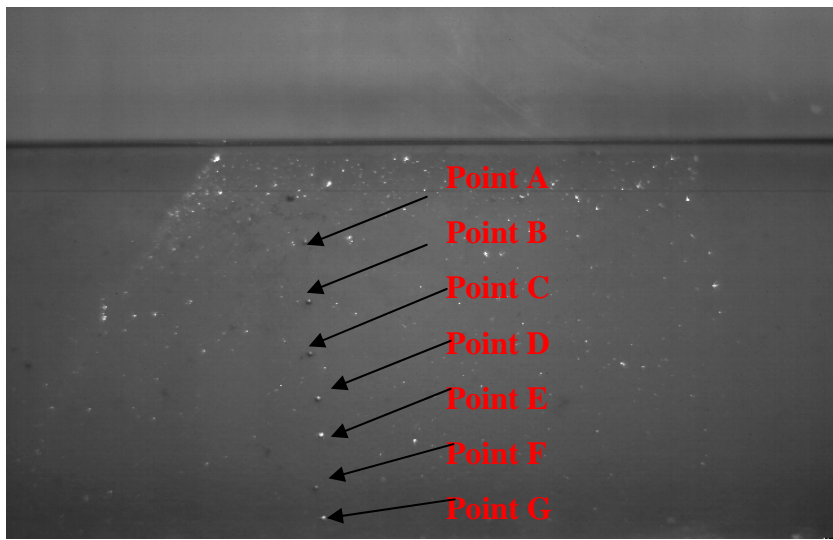
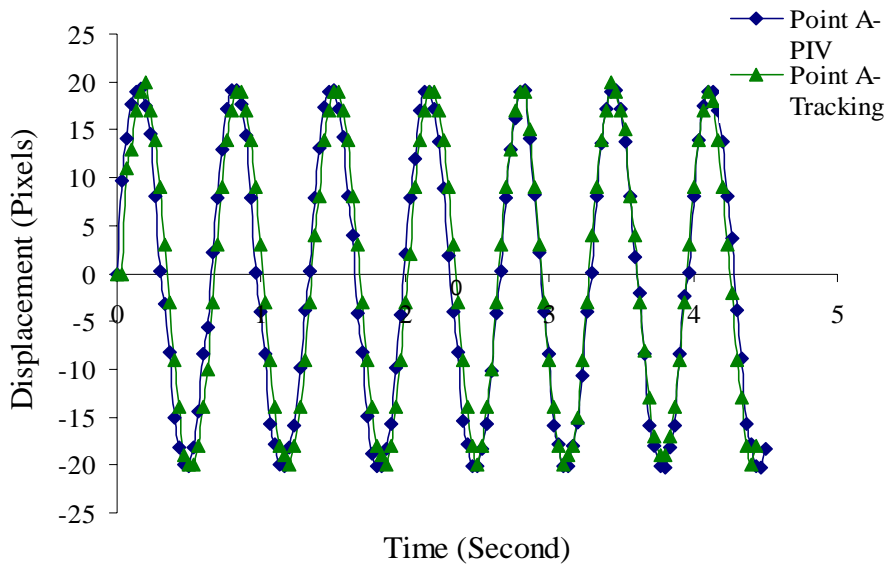
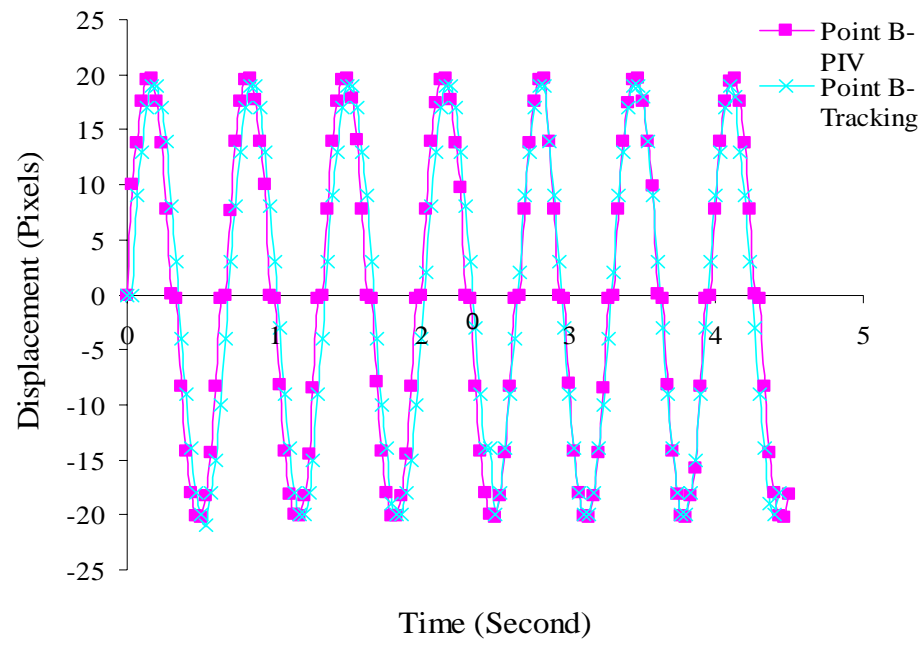


Figure 6.4. Mark Points Setup in the Transparent Soil Model

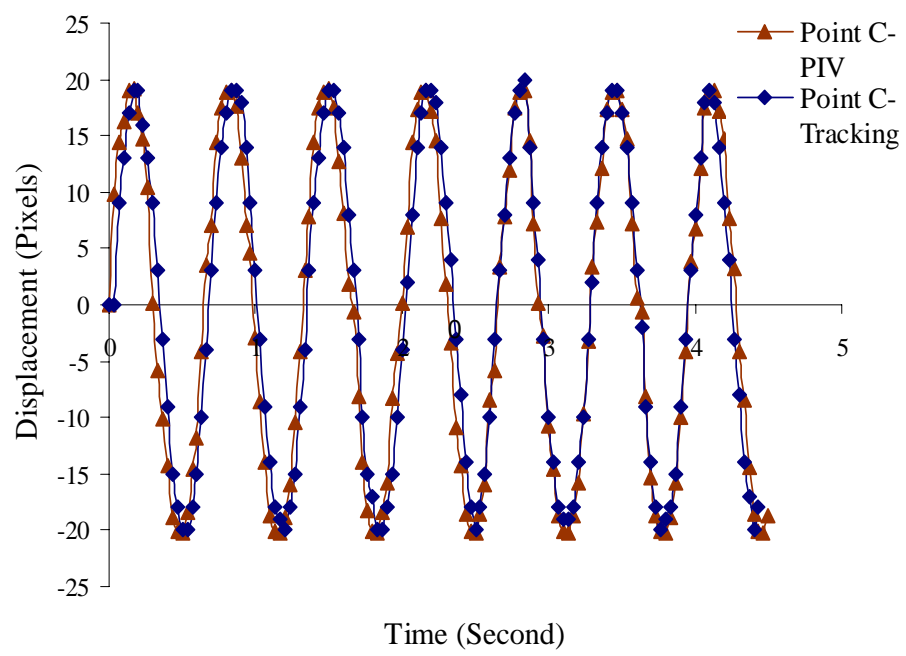


(a) Point A

Figure 6.5. Displacement vs Time Data from PIV and Tracking for Points A, B, C, D, E, F, and G

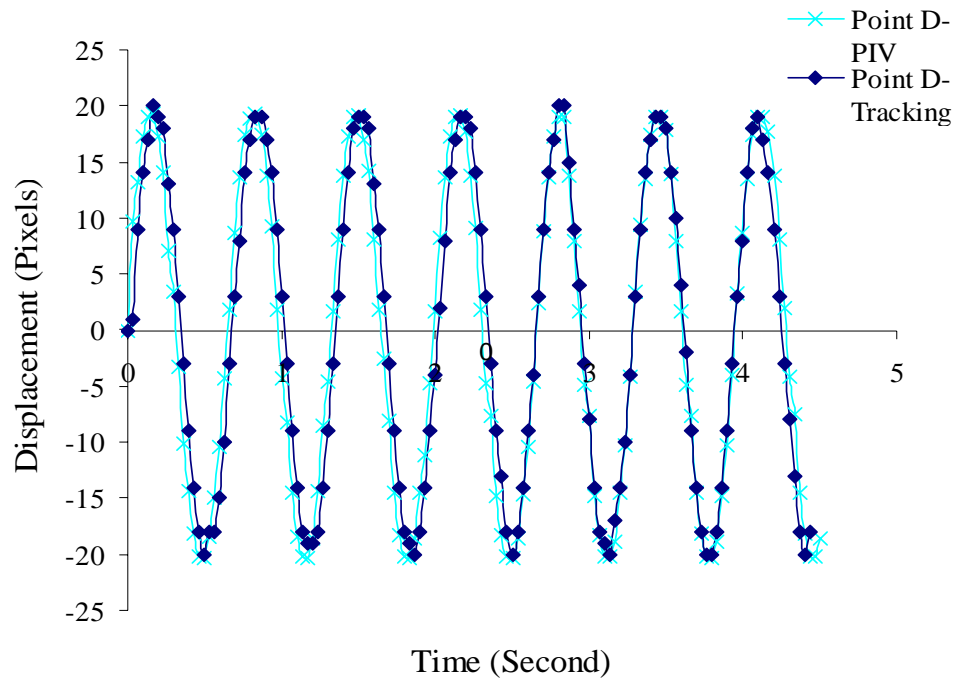


(b) Point B

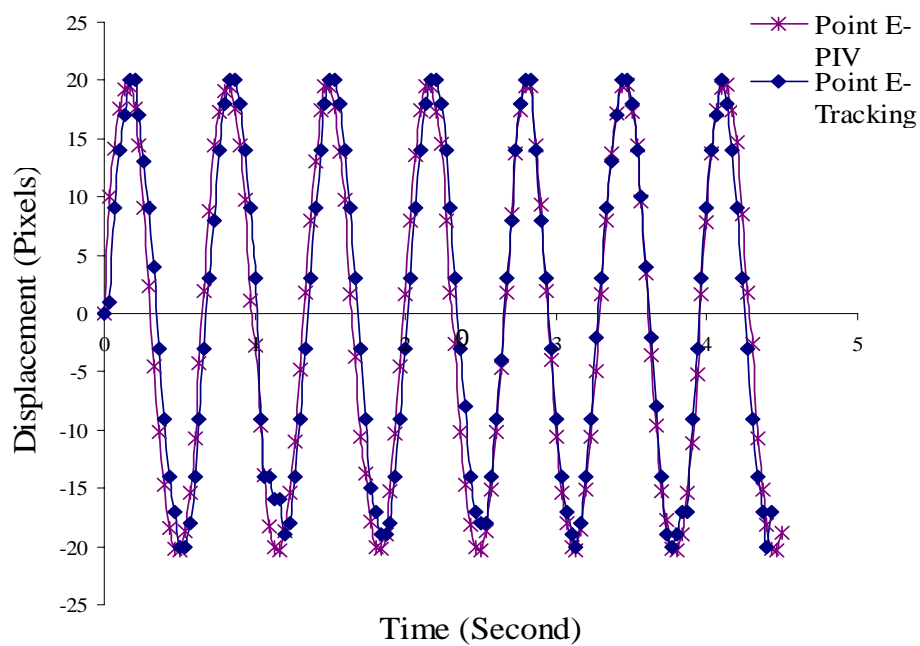


(c) Point C

Figure 6.5. Displacement vs Time Data from PIV and Manual Tracking for Points A, B, C, D, E, F, and G Cont'

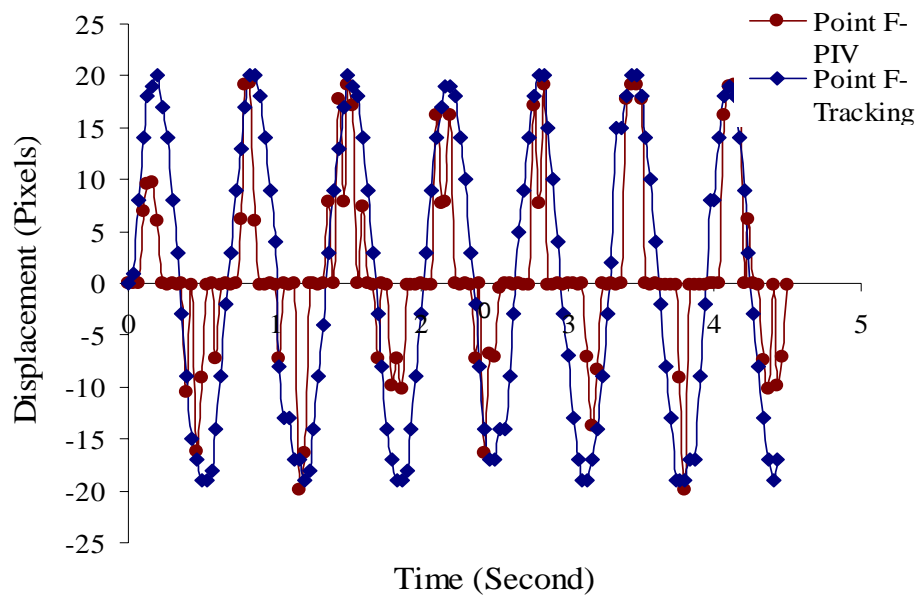


(d) Point D

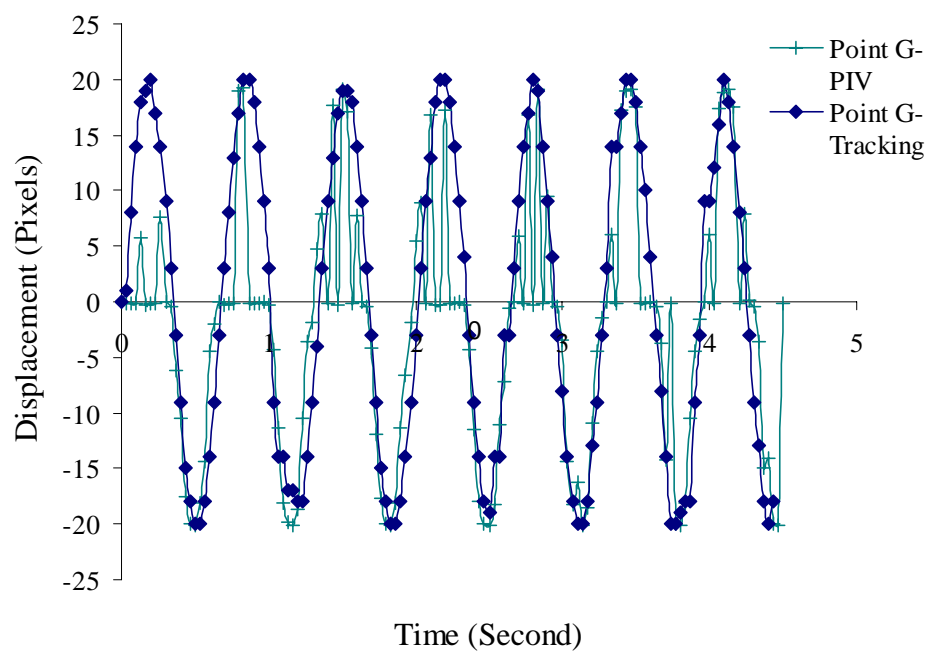


(e) Point E

Figure 6.5. Displacement vs Time Data from PIV and Manual Tracking for Points A, B, C, D, E, F, and G Cont'



(f) Point F



(g) Point G

Figure 6.5. Displacement vs Time Data from PIV and Manual Tracking for Points A, B, C, D, E, F, and G Cont'

6.2.7.2. The free-field motion of transparent soil model. A shake table test was set up to investigate the free-field motion of the transparent soil model. The input motion was a simple sine wave with 3 Hz frequency and 0.762 cm (0.3 in.) amplitude generated by the shaking table. The velocity field of the soil model is presented in Figure 6.6. Figure 6.6(a) shows the velocity field of the soil mass at $t=1/15$ seconds. At $t=1/15$ seconds, the transparent soil was moving in the right direction. Figure 6.6(b) shows the velocity field at $t=3/15$ seconds. At that time, the transparent soil was moving in the left direction, the velocity was reversed. Figure 6.6(c) shows the velocity field at $t=1/3$ seconds. At $t=1/3$ seconds, the transparent soil entered the second cycle. The velocity field was in the right direction again. However, due to the low power of the laser used in the research, the refraction points (white points) were not dense enough to get the high quality data. In the low light density area (the image pattern was not clear), and there were not many velocity vectors.

The motion of the center point of each small interrogation window can be obtained through the PIV analysis. Points A, B, C, and D at the different locations were selected as the representative points to study the free-field motion of the transparent soil model, as shown in Figure 6.7. Figure 6.8(a)-(f) shows the displacement time history of points A, B, C, and D at different locations of the soil mass. Point B was located at the center close to the bottom of the container. Point A was located in the middle depth of the soil model on the right side. Point C was located close to the soil surface at the middle part of the transparent soil model. Figure 6.8(a) shows the horizontal displacement-time history for points A and B. It was clear that the amplitude of displacement for point A was almost two times of the magnitude for point B. The ground motion was magnified when it propagated upward towards the soil surface. Figure 6.8(b) shows the vertical displacement-time history for Points A and B. The vertical displacement for Point B was very small. It was reasonable because Point B was located close to the bottom of the soil mass. The input horizontal motion does not produce much vertical motion in the bottom of the soil mass. The vertical displacement for Point A was higher than that of Point B. However, the vertical displacement data for Point B was more scattered. Figure 6.8(c) shows the horizontal displacement-time data for Point B and Point C. Figure 6.8(d) shows the vertical displacement-time data for Point B and Point C. Figure 6.8(e) shows

the horizontal displacement-time data for Points B and Points D. Figure 6.8(f) shows the vertical displacement-time data for Point B and Point D. Similar conclusions can be obtained for Points C and D as Point A from Figures 6.8(c) ~ (f). Points C and D were located at the same height above the bottom of the container. Their motion data closely match each other.

The scattered data in these figures possibly were due to the poor image quality. The time history data obtained through PIV analysis was not very smooth due to the low frame rate of the camera and the relatively high frequency of the signal.

The obtained testing data showed that PIV can capture the free-field motion of the transparent soil model pretty well. The free-field motion exhibited the amplification effects as the wave propagates upward from the bottom of the soil model. For the pure input horizontal shear wave, it will induce the vertical vibration of the soil particles.

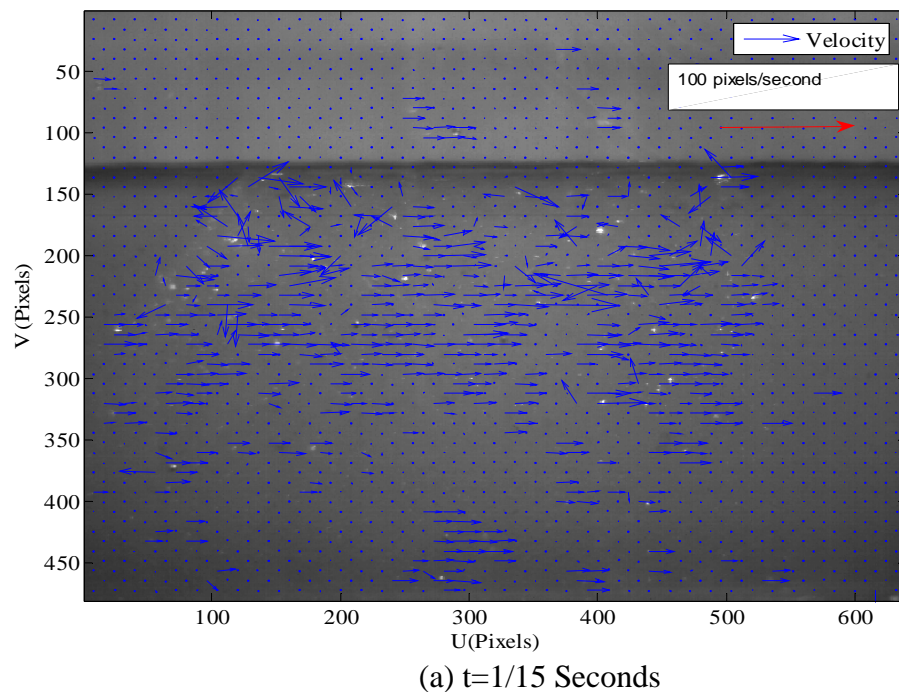


Figure 6.6. Instantaneous Velocity Field of Transparent Soil Mass (a) $t=1/15$ Seconds, (b) $t= 3/15$ Seconds, and (c) $t= 1/3$ Seconds under the Input Motion of 3 Hz, 0.3 inch Sinusoidal Wave (Magnification Factor =4)

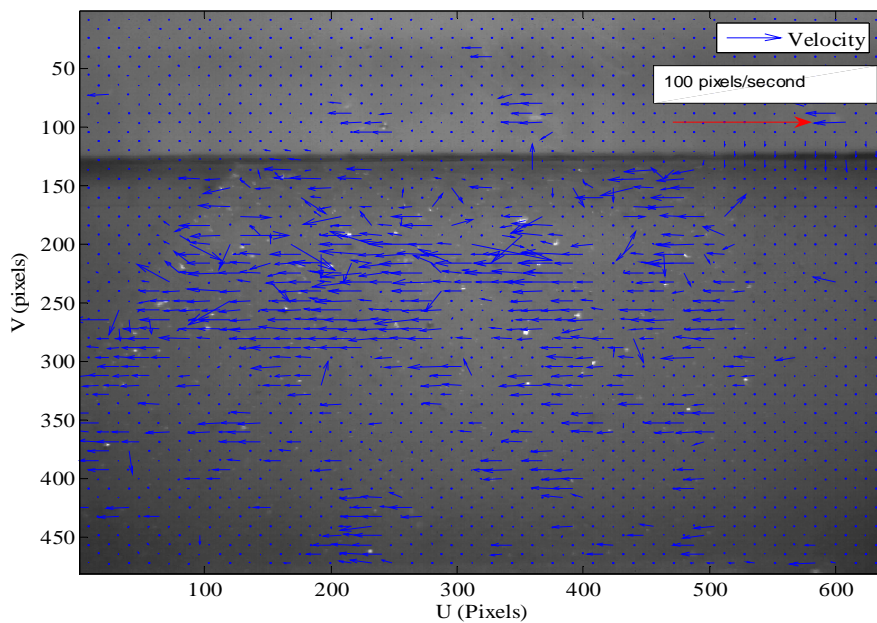
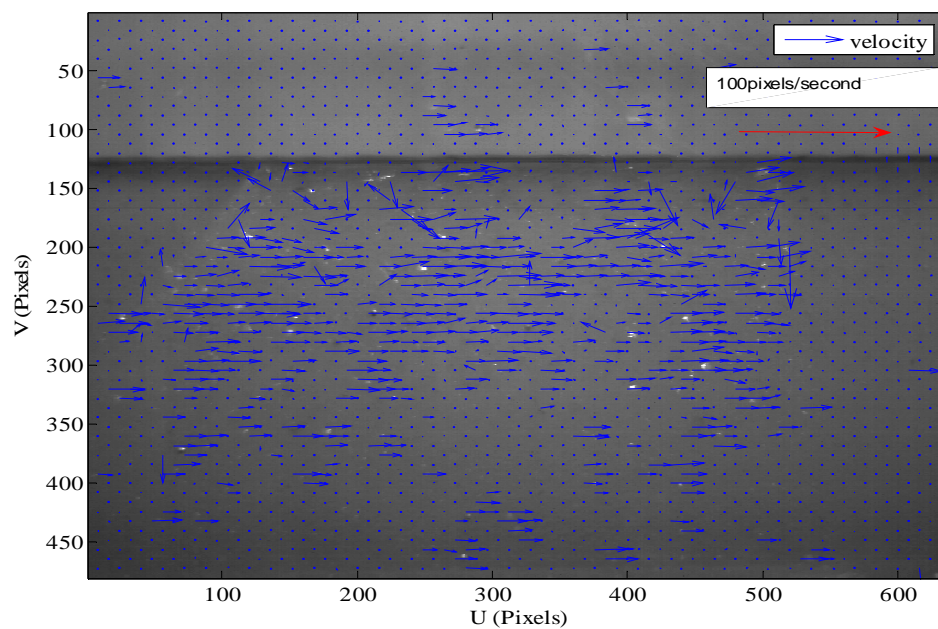
(b) $t = 3/15$ Seconds(c) $t = 1/3$ Seconds

Figure 6.6. Instantaneous Velocity Field of Transparent Soil Mass (a) $t = 1/15$ Seconds, (b) $t = 3/15$ Seconds, and (c) $t = 1/3$ Seconds under the Input Motion of 3 Hz, 0.3 inch Sinusoidal Wave (Magnification Factor =4) Cont'

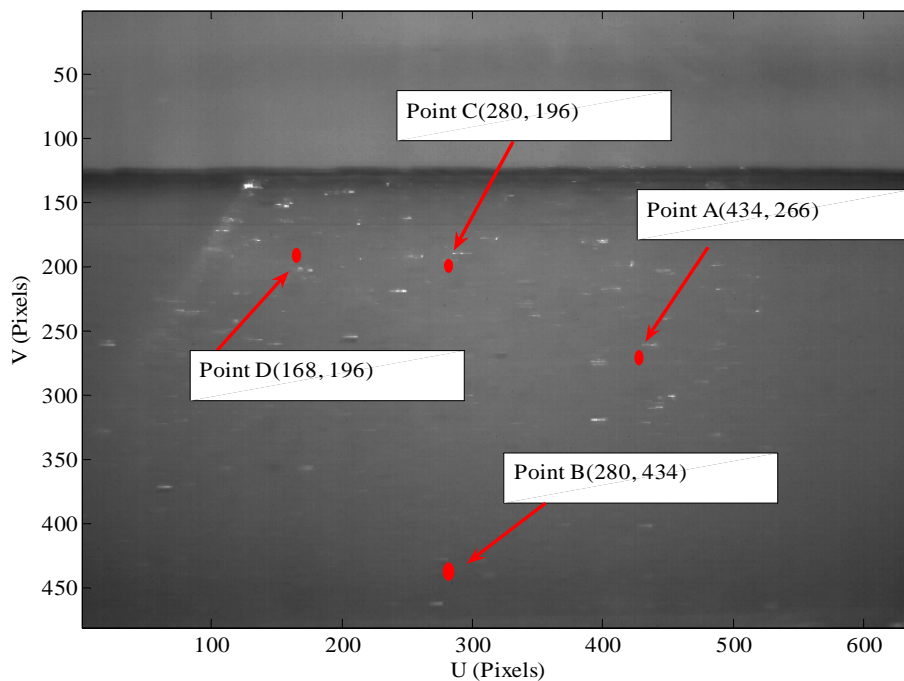
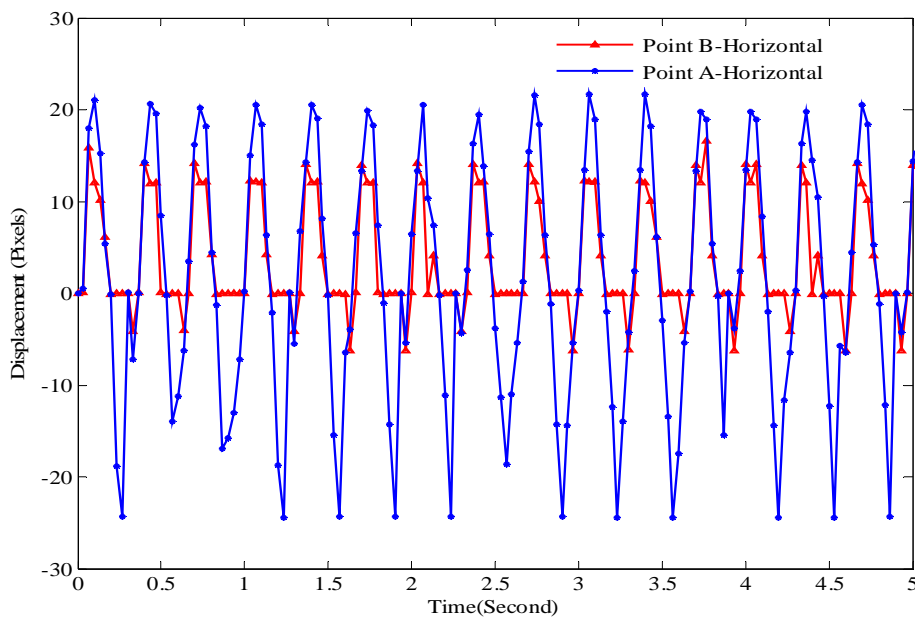
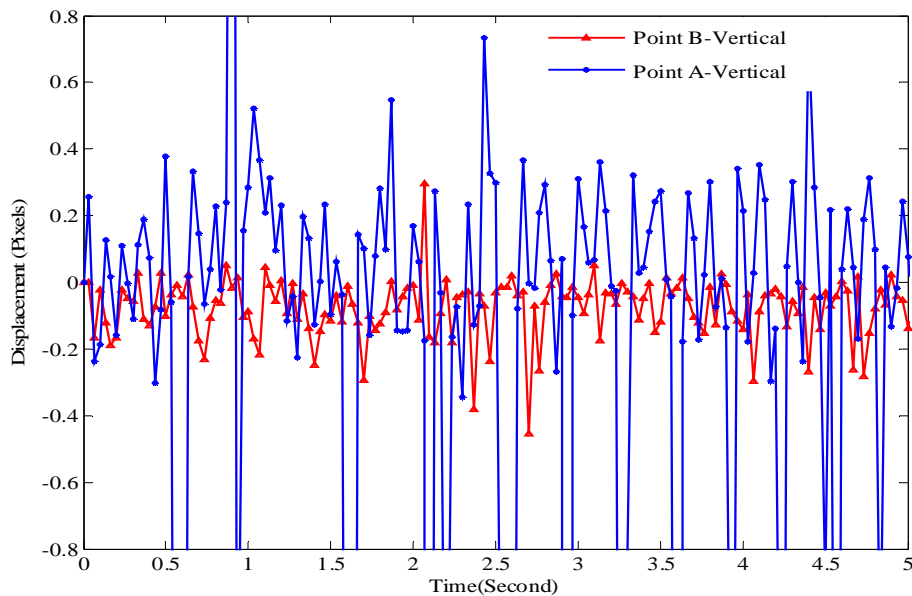


Figure 6.7. The Locations of Points A, B, C, and D in the Soil Model

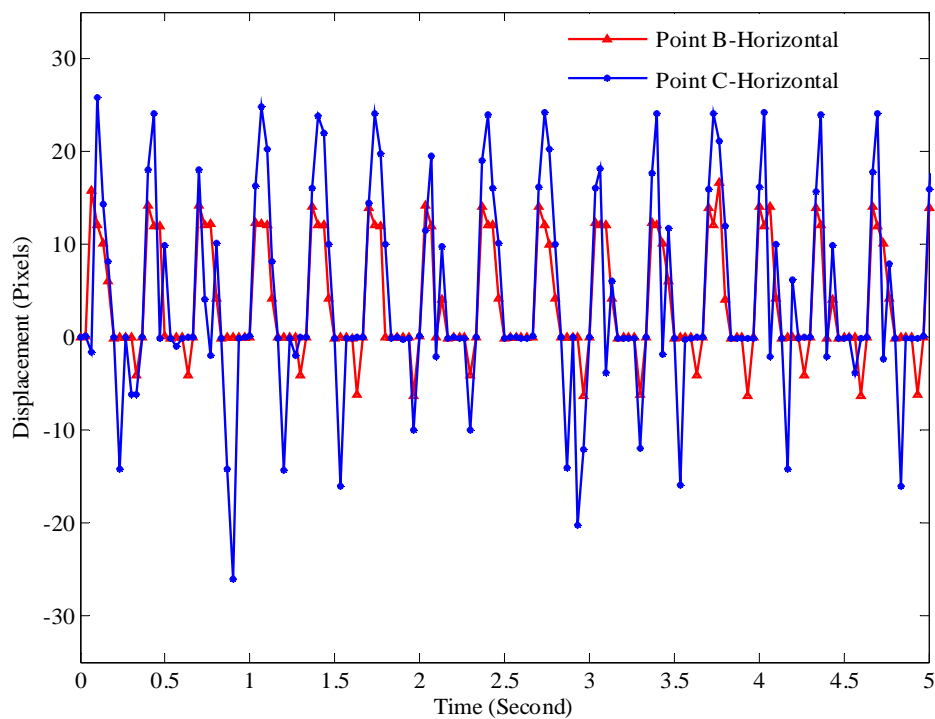


(a) The Displacement-Time History of Point A and Point B in the Horizontal Direction

Figure 6.8. The Displacement History of Points A, B, C, and D

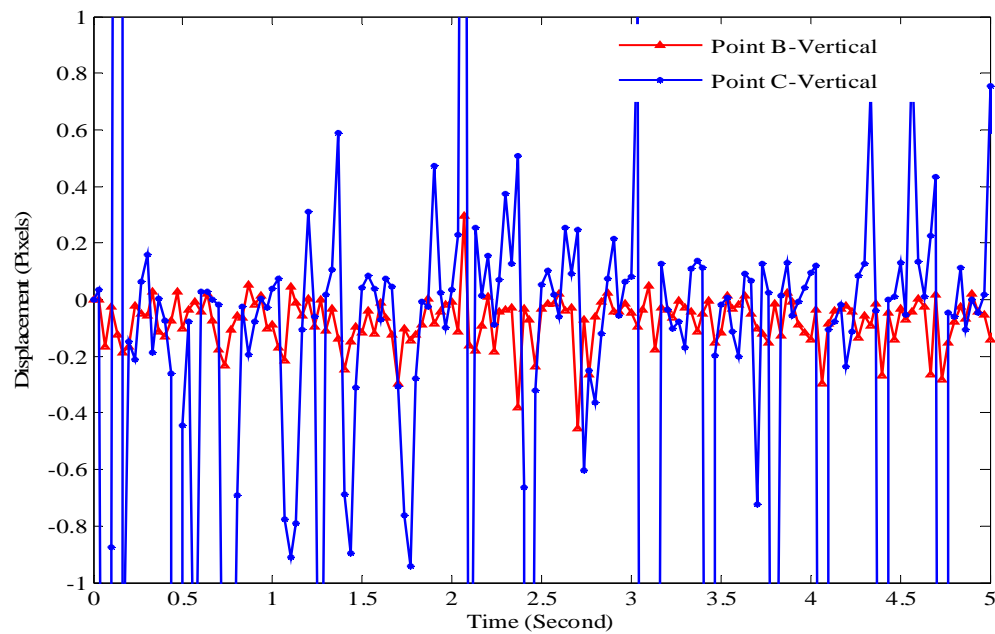


(b) The Displacement-Time History of Point A and Point B in the Vertical Direction

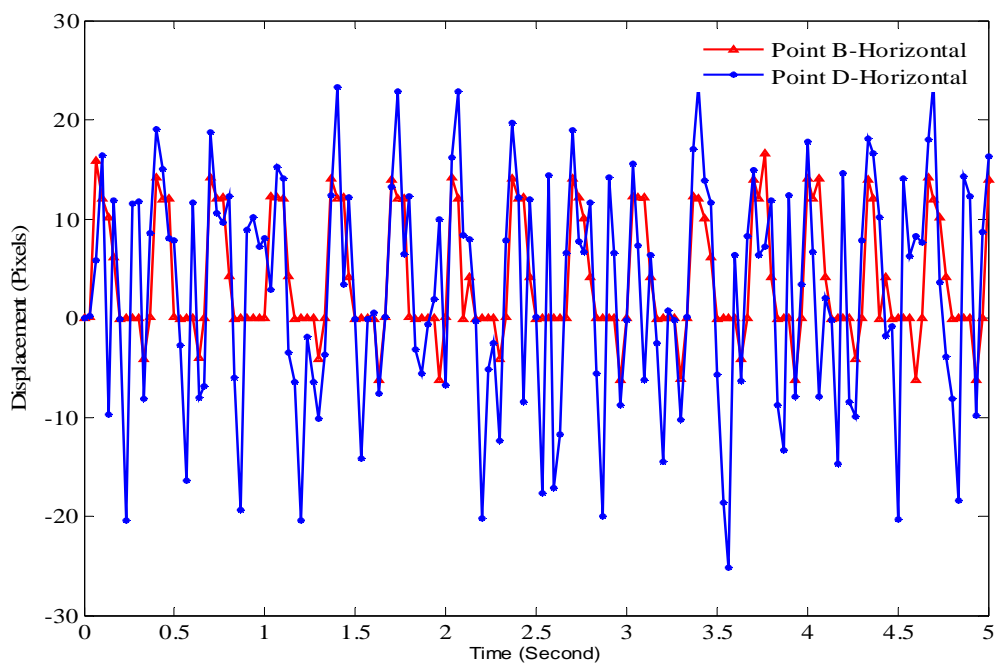


(c) The Displacement History of Point B and Point C in the Horizontal Direction

Figure 6.8. The Displacement History of Points A, B, C, and D Cont'

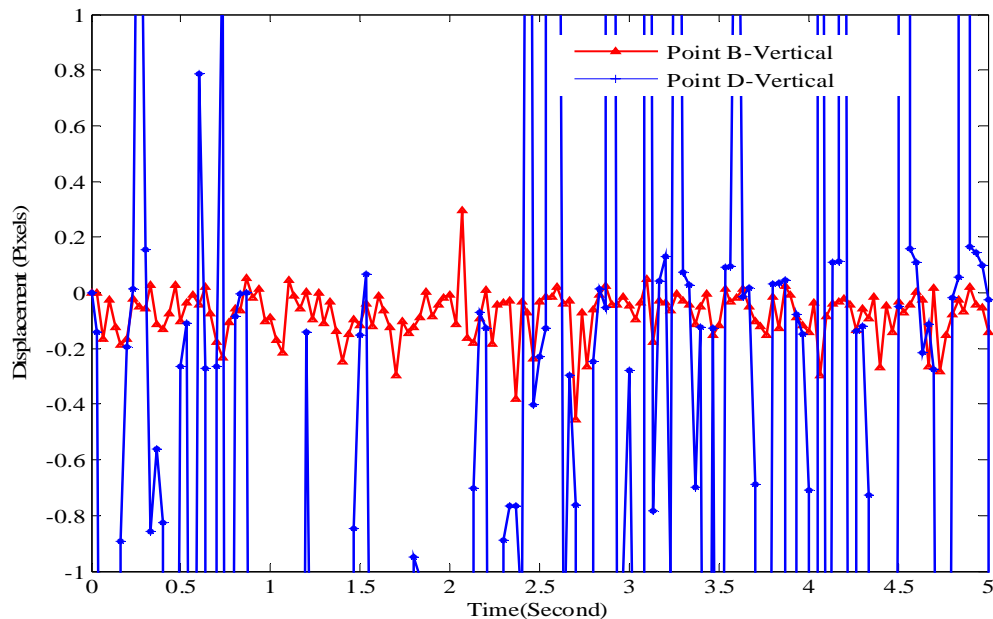


(d) The Displacement History of Point B and Point C in the Vertical Direction



(e) The Displacement History of Point B and Point D in the Horizontal Direction

Figure 6.8. The Displacement History of Points A, B, C, and D Cont'



(f) The Displacement History of Point B and Point D
In the Vertical Direction

Figure 6.8. The Displacement History of Points A, B, C, and D Cont'

6.2.7.3. The shake table tests on the rigid-block and soil interaction. To investigate the rigid-block and soil interaction, two shake table tests were carried out on the small wood block model. The rigid wood block was embedded 2.54 cm (1 in.) deep into the transparent soil. The test setup was the same as shown in Figure 6.3. In the first shake table test, a 2 Hz, 0.635 cm (0.25 in.) sinusoidal wave was generated from the shaking table and as an input to the shake table container. This sinusoidal wave was then transferred to the bottom of the soil model and propagated upward to the soil surface. The PIV system was used to capture the motion images of the rigid wood block and the soil surrounding the wood block during the shaking period. Figure 6.9 shows the wood block position at $t = 0$ second, 0.1 second, 1.5 second, and 1.8 second in the shaking event, respectively. It was observed that when the excitation started, the shaking table was moving in the right direction, the portion of the wood block embedded into the soil was moving together with the soil mass surrounding it; however, the top portion above the soil surface tended to move in the opposite direction of the ground due to its inertial mass

effect; this led to the tilting of the block in the opposite direction of the ground after the excitation started in the first $\frac{1}{4}$ cycle. As soon as the shaking table was moving in the reverse direction, the rigid wood block would tilt back slightly to its resting position in the second and third $\frac{1}{4}$ cycle because of the ground motion in the reverse direction. However, the excitation was not strong enough to bring the wood block completely back to its resting position. In the fourth $\frac{1}{4}$ cycle, the shake table was moving in the right direction again, the wood block rotated to the left direction and the tilting angle was becoming larger this time. At now, the wood block finished the first complete cycle of the vibration. For the second cycle and the third cycle, the above described behavior repeated. With the number of the cycles increasing, the rotating angle was increasing each time. The reverse motion of the ground can still sustain the rotating motion of the wood block without overturning. Once the wood block entered the fourth cycle, the accumulated moment was so large that the inverse motion of the ground could not sustain the rotation of the rigid block, the soil surrounding the rigid block were mobilized and displayed a large plastic deformation, the wood block overturned with a bearing capacity type failure of the soil foundation. The red line in Figure 6.11 showed the time history of the rotation angle for the wood block for the input sine wave motion of 2Hz, 0.25 inch (0.635 cm).

In the second shake table test on the block and soil interaction, the experiment setup was kept the same; the embedment depth of the wood block was still set as 1 inch (2.54 cm). The frequency of the input sine wave motion was kept still at 2 Hz, the amplitude of the input sine wave was increased to 0.5 inch (1.27 cm). Figure 6.10 shows the position of the wood block at $t = 0$ second, 0.1 second, 0.5 second, and 0.7 second during the shaking event, respectively. At the start of the excitation, the shaking table was moving in the right direction. The portion of the wood block embedded into the soil was moving together with the surrounding soil mass in the right direction, the top portion of the wood block above the soil surface moving towards the left direction, thus, this resulted the tilting of the wood block to the left. The tilting angle was increasing with the shaking table continually moving in the right direction until the end of the first $\frac{1}{4}$ cycle. The shaking table started to move in the left direction after entering the second and third $\frac{1}{4}$ cycle. The reverse motion of the soil mass was bringing the wood block tilting back to

the right direction. In this case, the ground motion was so strong that it took the wood block back to the resting position and the block tilting slightly towards the left comparing to the initial resting position at the end of the third $\frac{1}{4}$ cycle. For the fourth $\frac{1}{4}$ cycle, the shaking table was moving in the right direction again, the wood block was rotating toward the left with a larger rotating angle. The soil particles were mobilized and a relatively large deformation was induced in the soil mass. As the shaking table continued moving in the right direction for the first $\frac{1}{4}$ cycle for of the second period, the rotation angle of the wood block kept increasing. After the wood block entering the second $\frac{1}{4}$ cycle of the second period, the shaking table was moving reversely in the left direction; however, this reverse ground motion did not have any influence on the motion of the block, the wood block overturned in the second $\frac{1}{4}$ cycle of the second period of shaking. The rotation angle with time was plotted as the green line in Figure 6.11.

It was interesting to notice that there was no uplift and gap between the rigid block base and the soil beneath it, because the soil was very flexible. For both cases, the rigid block rotated back and forth at the beginning of the shaking event. However, the rigid block never rotated back to its resting position. Once the rotating angle reached 6.86° (close to $\frac{1}{2}$ of toppling angle $\phi=14^\circ$), the rigid block overturned and failed with a bearing capacity failure. From Figure 6.11, when the amplitude of the input wave was increased to 0.5 inch (1.27 cm), the wood block overturned in a much less time than the case of the 0.25 inch (0.635 cm) amplitude of the input motion, which indicates that large amplitude of the input motion can more easily turn the rigid block over than the input motion with the low amplitude. The time history of the rotating angle obtained from this research has the similar characteristics as the simulation results by Gazetas et al (2004) as shown in Figure 6.12. In their simulation, the rigid block was resting the soil surface, when the foundation is very flexible (the case of $E_s = 10MPa$), once the excitation started, the rigid block rotated towards one direction; the rigid block overturned within the first cycle of the shaking motion. The very flexible soil was mobilized by the rigid block and experienced a large deformation. The rigid block failed with the bearing capacity type of failure. In this research, there was 2.54 cm (1 in.) embedment depth for the wood block, the surrounding soil mass would try to bring the block to move together with it. The bearing capacity type of failure was mobilized until the moment of the block

was large enough. This was the reason why the result obtained from this research was slightly different from the data by Gazetas et al (2004).

For the two shake table tests, there was a slight sliding of the rigid wood block observed during the shaking event. There was no impact observed during the shaking event under both 2.5 Hz, 0.25 inch (0.635 cm) and 2.5 Hz, 0.5 inch (1.27 cm) input sinusoidal wave. This behavior was different from the rigid block on rigid foundation as reviewed earlier.

6.2.7.4. The motion of the transparent soil and the rigid-block during the shaking. A PIV analysis was performed on the captured images to obtain the instantaneous velocity field of the transparent soil model. Figure 6.13 shows the instantaneous velocity field of the rigid block and the transparent soil at time $t = 0.1$ second, 1 second, and 1.6 second, respectively. Due to the low power of the laser sheet used in the research program, there were not enough velocity vectors at the places far from the laser beam.

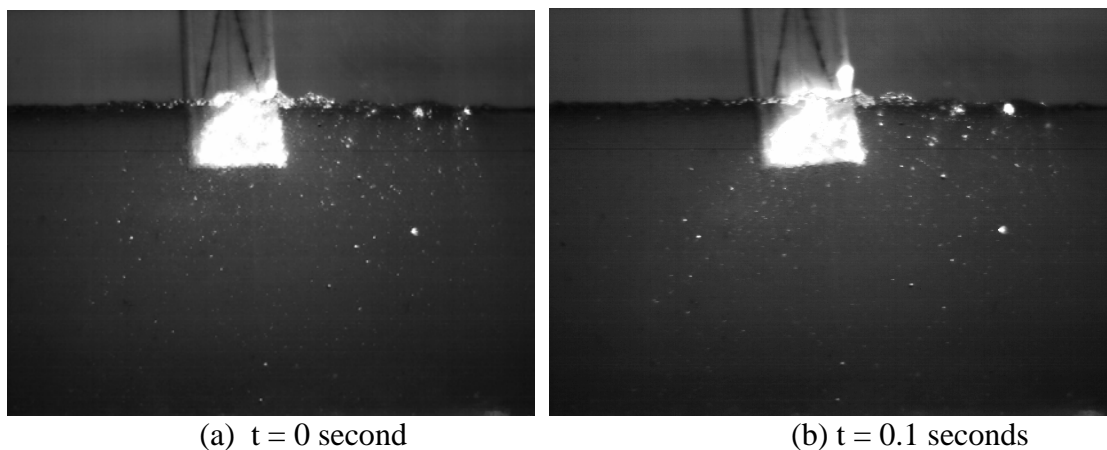


Figure 6.9. The Motion of the Rigid-Block at Different Time under the Input Motion of 2 Hz, 0.25 inch (0.635 cm)

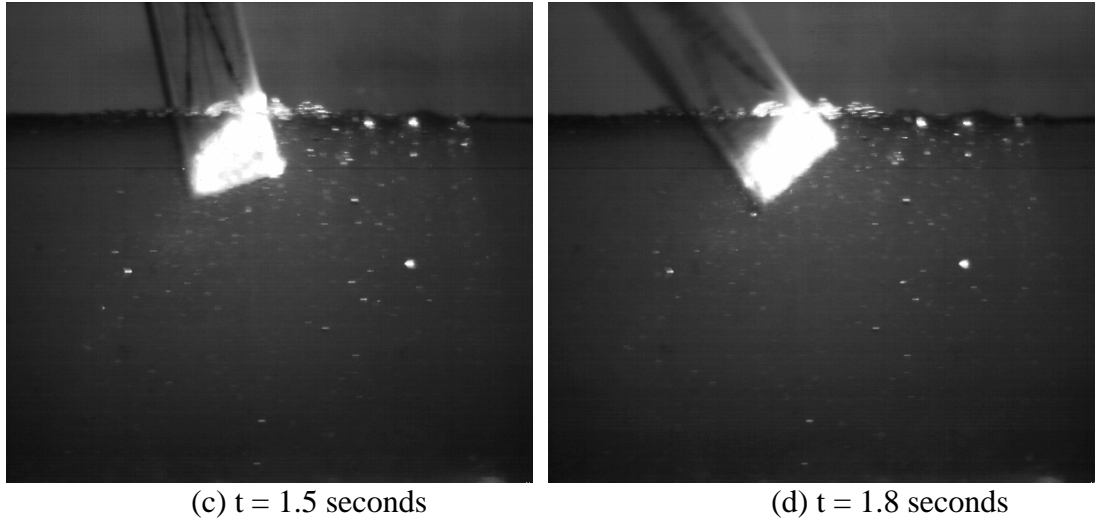


Figure 6.9. The Motion of the Rigid-Block at Different Time under the Input Motion of 2 Hz, 0.25 inch (0.635 cm) Cont'

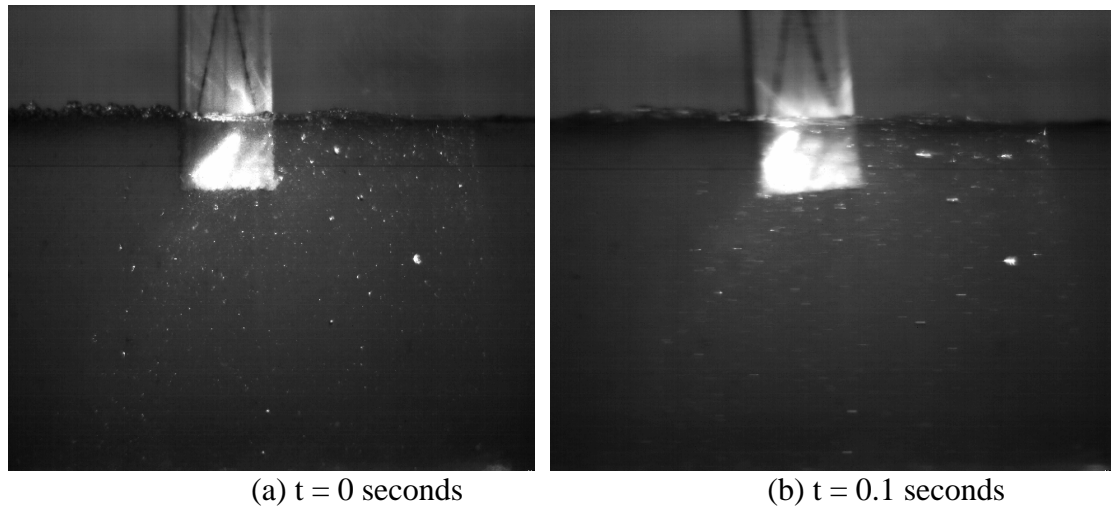


Figure 6.10. The Motion of the Rigid-Block at Different Time under the Input Motion of 2 Hz, 0.5 inch (1.27 cm)

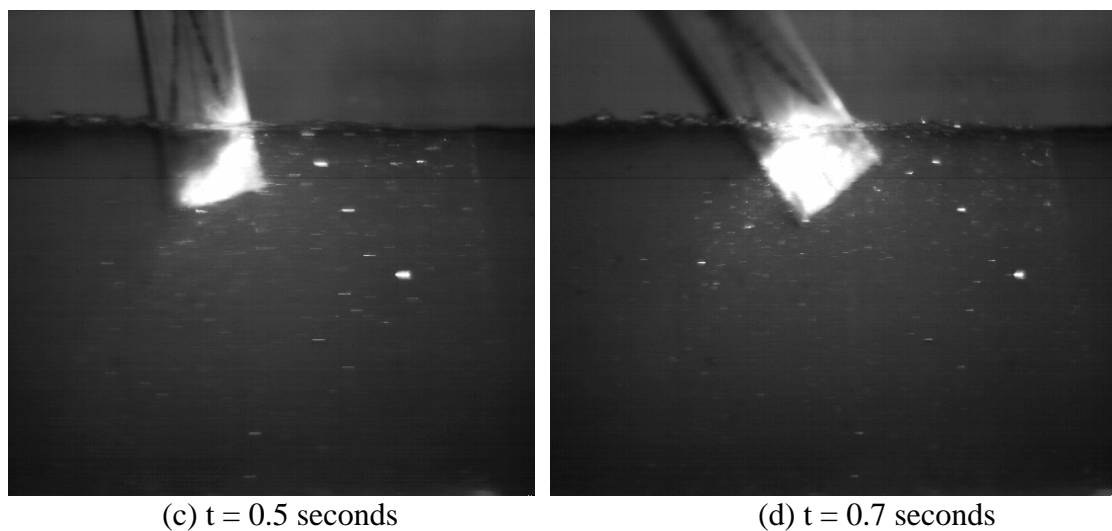


Figure 6.10. The Motion of the Rigid-Block at Different Time under the Input Motion of 2 Hz, 0.5 inch (1.27 cm) Cont'

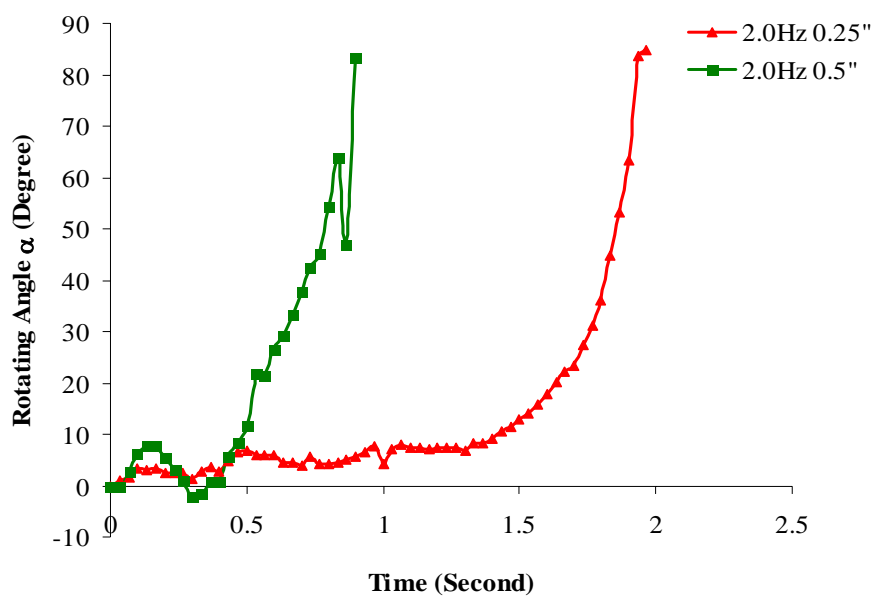


Figure 6.11. The Time History of the Rotating Angle α

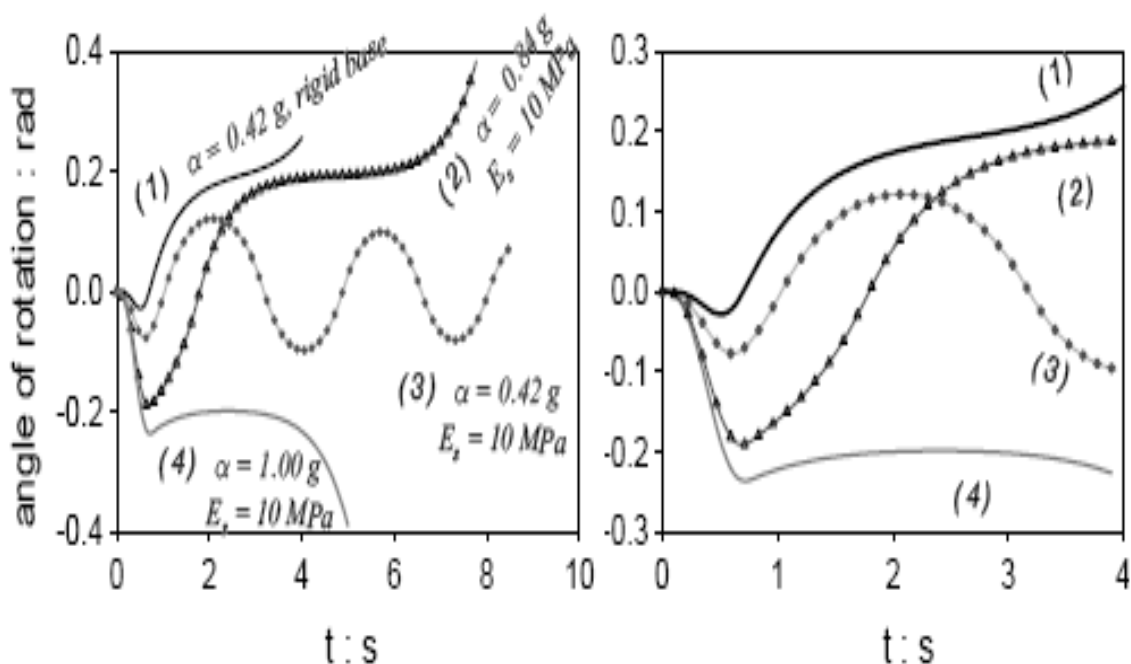
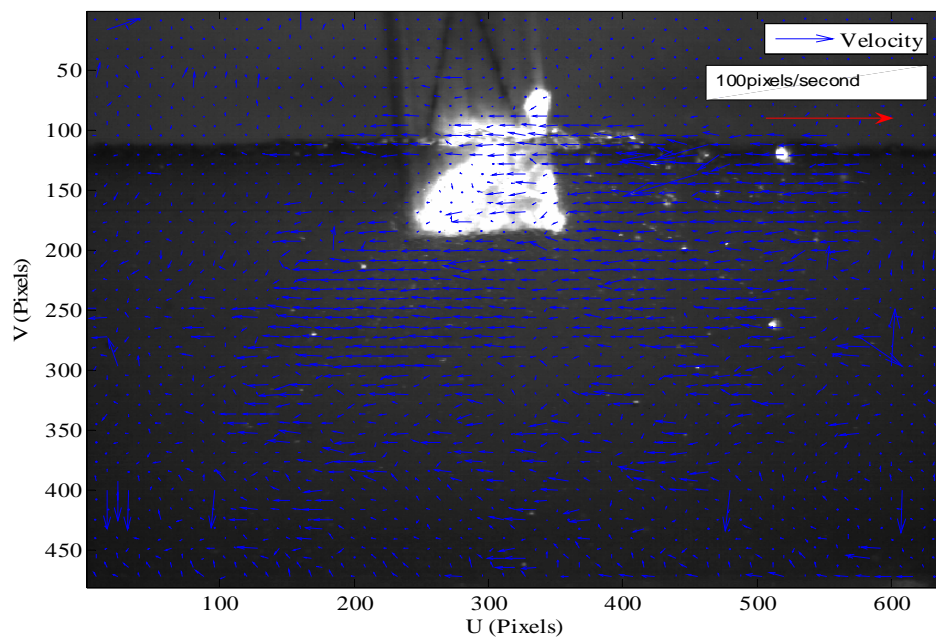
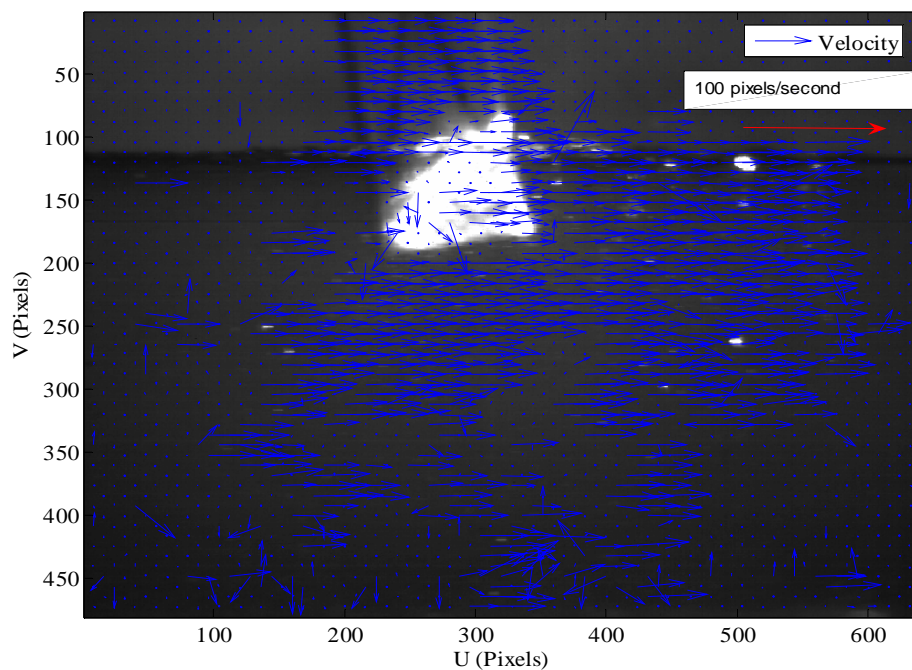


Figure 6.12. The Time History of Rotation of a Slender Rigid-Block with $B = 1$ m and $H = 5$ m (The toppling angle $\alpha = 11.46^\circ$ and $R = 2.5$ m, supported on elastic soil with E_s as an independent parameter. The excitation is a one-cycle sinusoidal pulse with frequency of 1.25 Hz but with different peak acceleration the first for each curve. The right figure is merely an enlargement of 4 seconds of motion shown on the left figure) (Gazetas et al., 2004)

For the case where a 2.5 Hz, 0.25 inch (0.635 cm) sinusoidal wave was applied, to investigate the motion of the rigid block and the motion of the transparent soil model, points A1, B1, C1, and D1 at the different locations of the transparent soil model were selected as study points as shown in Figure 6.14. Point A1 was located on the right and close to the rigid block. Point B1 was located at the same elevation level as A1, but far from the rigid block. Point C1 was located at the right bottom of the transparent soil model. Its motion can represent the motion at the bottom of the soil. Point D1 was located at the top very close to the surface of the soil. Points A1 and B1 were chosen to study the near field and far field effects of soil-structure interaction. Points C1 and D1 were chosen to investigate the amplification effect of the wave as it propagated upward.

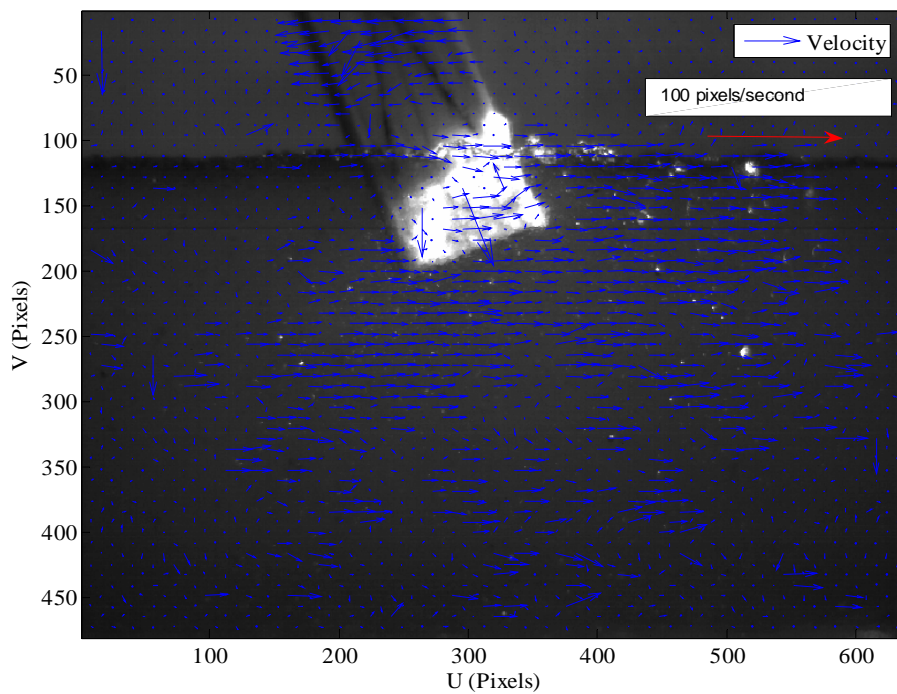


(a) $t = 0.1$ second (magnification factor =4)



(b) $t = 1.0$ seconds (magnification factor =4)

Figure 6.13. Instantaneous Velocity Field of the Testing Model at (a) $t = 0.1$ Second, (b) $t = 1.0$ Second, and (c) $t = 1.6$ Second (Input motion: 2.0 Hz, 0.25 inch sinusoidal wave)



(c) $t = 1.6$ seconds (magnification factor = 4)

Figure 6.13. Instantaneous Velocity Field of the Testing Model (a) $t = 0.1$ Second, (b) $t = 1.0$ Second, and (c) $t = 1.6$ Seconds (Input motion: 2.0 Hz, 0.25 inch sinusoidal wave) Cont'

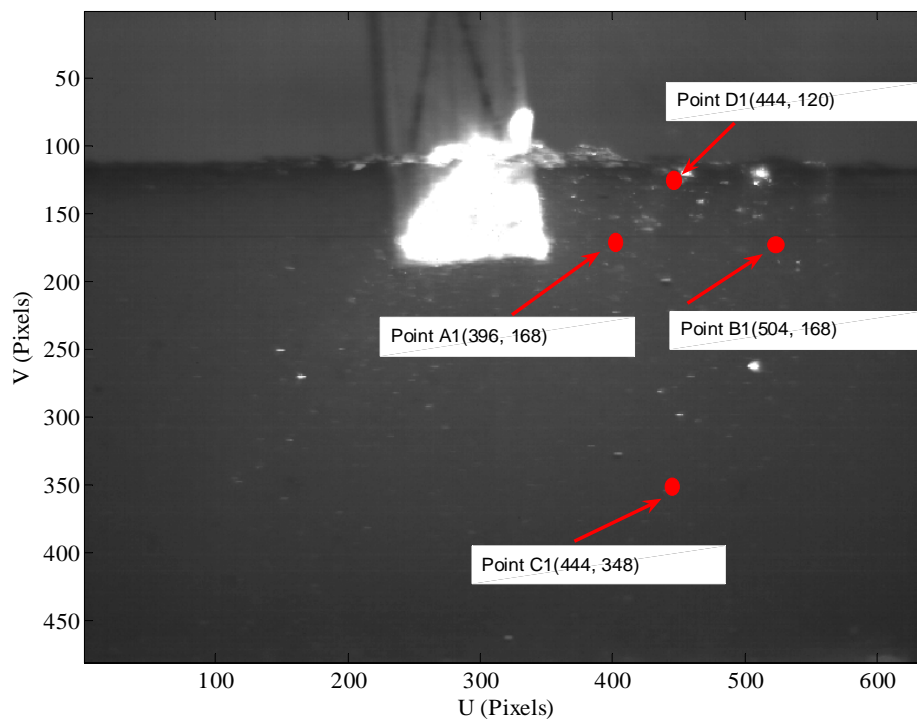


Figure 6.14. The Locations of Points A1, B1, C1, and D1

The displacement-time data for Points A1, B1, C1, and D1 are plotted in Figures 6.15~6.18. The data showed that the two points (A1, B1) had similar motion at the beginning of the shaking. With the time increasing, Point A1 was affected by the motion of the rigid block; the displacement of Point A1 became larger than that of Point B1. Point B1 was not affected much by rigid block motion. These phenomena were commonly called the near field and far filed effects in the dynamic soil-structure interaction. This effect was more significant when looking at the vertical displacement data for A1 and B1. Point A1 had a more significant vertical vibration than Point B1. Point C1 and Point D1 were selected to investigate the propagation of the earthquake wave from the bottom of the transparent soil model upward to the soil surface. Point C1 was located in the right above the bottom of the soil mass. Point D1 was located right near to the soil surface. Their displacement time history relationship is plotted in Figure 6.17 and Figure 6.18. It can clearly be seen that both the horizontal motion and the vertical motion were magnified as the wave propagating upwards. There was almost no vertical vibration at the bottom of the soil. At the surface of the soil, the vertical vibration was much more significant.

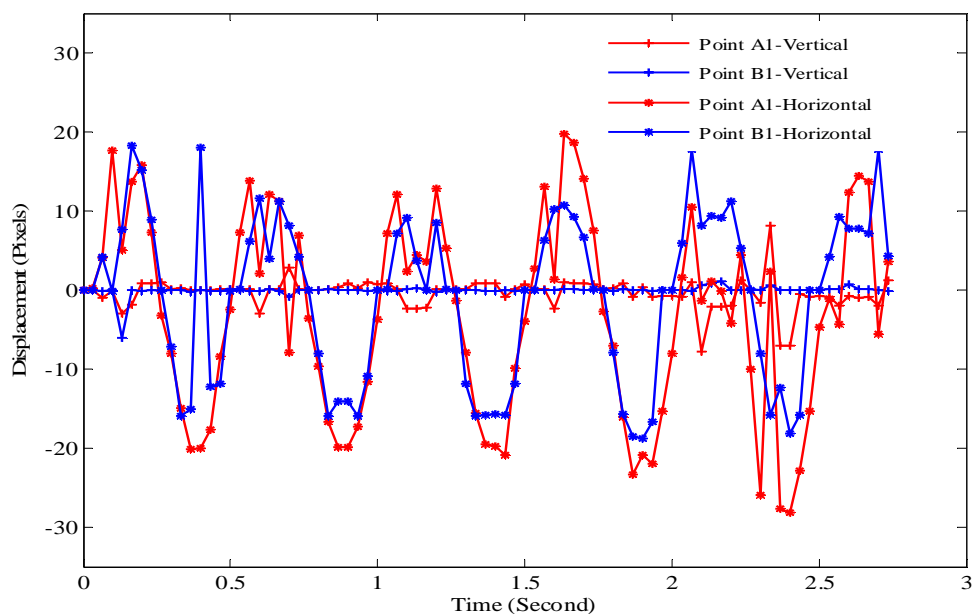


Figure 6.15. Displacement – Time History for Points A1, B1 in both the Vertical Direction and the Horizontal Direction in the Image Space

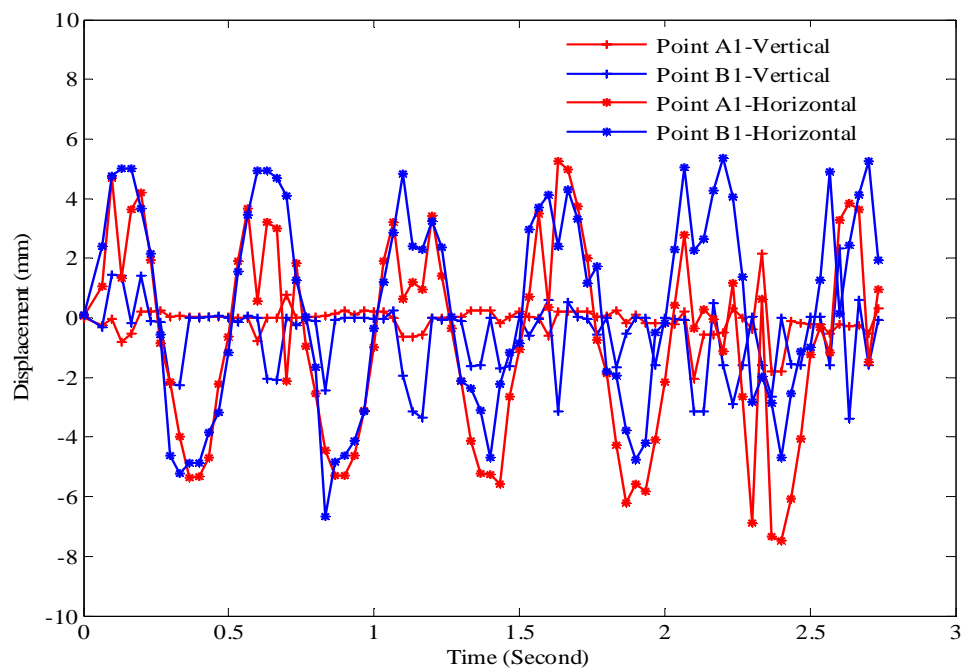


Figure 6.16. Displacement – Time History for Points A1, B1 in both the Vertical Direction and the Horizontal Direction in the Real Space

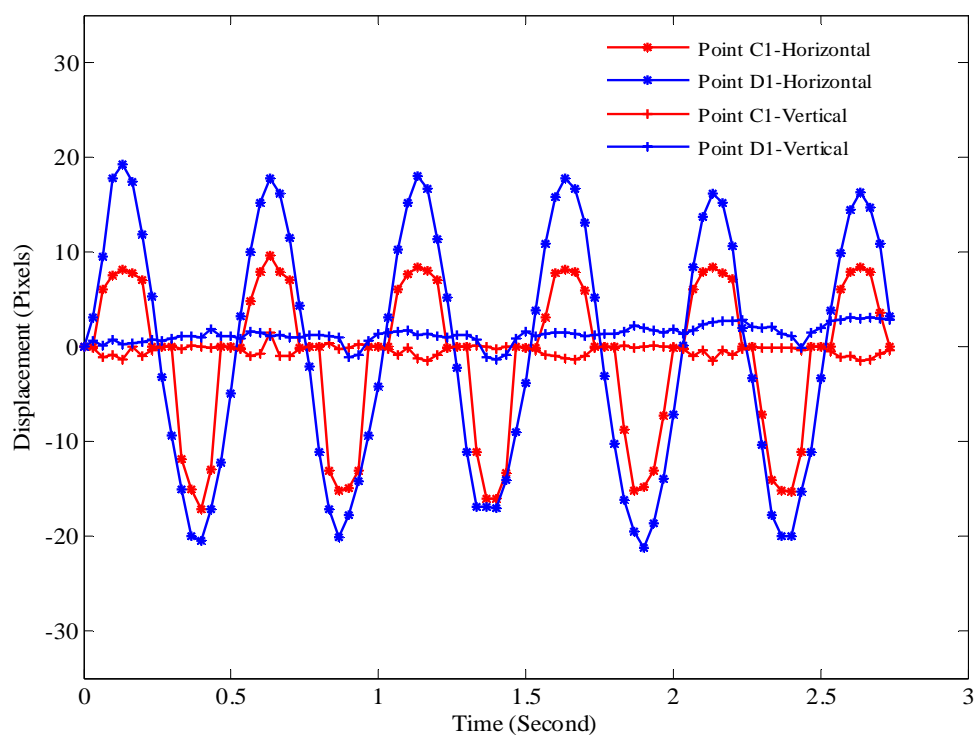


Figure 6.17. Displacement – Time History for Points C1, D1 in both the Vertical Direction and the Horizontal Direction in the Image Space

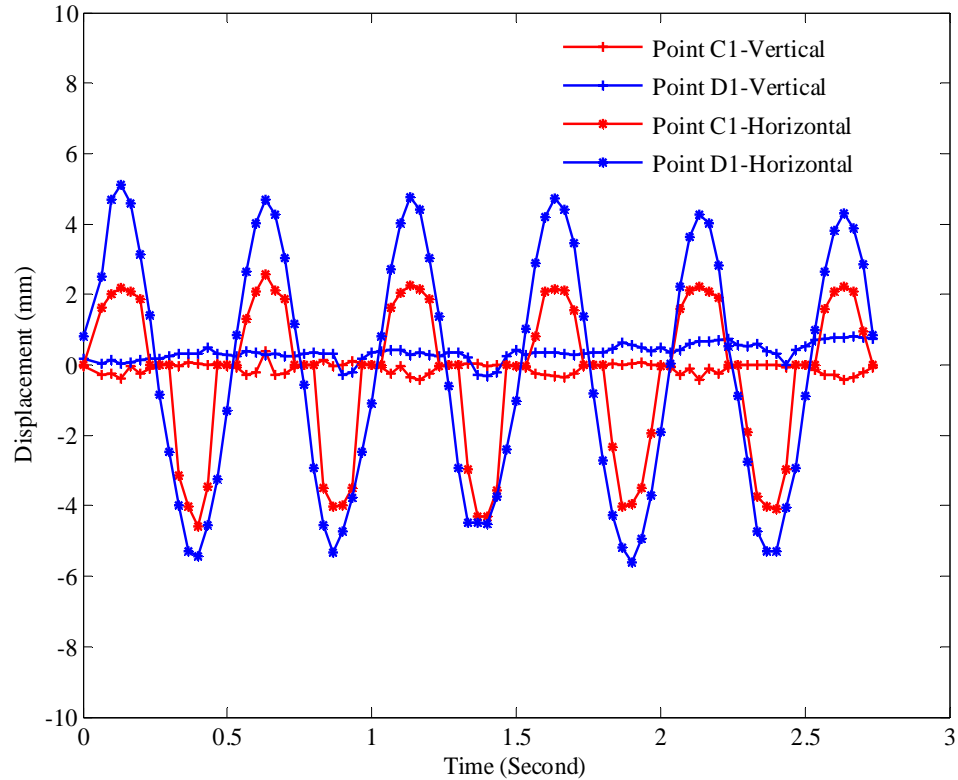


Figure 6.18. Displacement – Time History for Points C1, D1 in Both the Vertical Direction and the Horizontal Direction in the Real Space

6.6. SUMMARY

This section presented the application of the PIV technique and transparent soil to visualize the rigid block-soil interaction under simulated earthquake motion from the shake table test. The PIV algorithm has been proved to be an effective method to capture the motion of the transparent soil and the rigid block. The biggest advantage of the PIV algorithm is that it can capture the full-field motion of the soil mass which is impossible for traditional instrumentation methods. The free-field motion shake table test clearly showed the amplification effects as the wave propagated upward from the bottom. Two shake table tests conducted on the small scale rigid wood model were investigated in more details in this section with the same frequency but different amplitudes. The testing results from the shake table test showed that the rigid wood block failed by a bearing capacity failure. The larger amplitude of the input motion at the same frequency would

more easily topple the rigid block (the time for the wood block to overturn is less). The shake table test has also showed the near field effect and far field effects. The near field soil motion was significantly influenced by the motion of the rigid block. The far field soil motion was not affected by the motion of the rigid block.

7. CONCLUSIONS AND FUTURE RESEARCH RECOMMENDATIONS

7.1. CONCLUSIONS

From the series of resonant column tests conducted, transparent silica gel was found to have similar dynamic properties as natural sand under relatively low confining pressure. Transparent silica gel can be used as an effective substitute when studying the dynamic related problems in geomechanics such as the wave propagation, structure-soil interaction, and liquefaction.

Extensive research work was conducted, searching for a low viscosity pore fluid with the least interaction with the latex membrane. 12 different types of chemical solvents were investigated in this research. Their refractive indexes and viscosities were tested under different temperatures. The research discovered that both the refractive index and the viscosity of all the chemical solvents tested linearly varied with the temperature in the range of 15°C-35 °C. Three chemical fluids (Toluene, Lamp Oil, and Pyridine) were taken as the base pore fluid in this research. The testing results discovered that Toluene and Lamp Oil can mix with certain chemical solvents to make the refractive index matching pore fluid for manufacturing the transparent soil. Pyridine was unable to make the transparent soil with any of the chemical solvents tested. The immersion tests conducted on the latex membrane with all the candidate pore fluids showed that a strong interaction occurred between the latex membrane and the Lamp Oil-based pore fluid. Lamp Oil was unsuitable for manufacturing the matching pore fluid for the transparent soil. The pore fluids of Toluene mixed with 2 Propanol and Toluene mixed with Methyl Ethyl Ketone were recommended to be used to manufacture the transparent soil since they have the least interaction with the latex membrane from the immersion test. The matching refractive index with the dry silica gel was 1.447 at 25°C. The matching ratios were 1.07:1 and 0.95:1, respectively. Toluene mixed with Acetonitrile, Ethyl Acetate, and Iso-Butanol was found to cause a strong degradation of the latex membrane. Hence, they are not recommended for manufacturing the transparent soil, especially for triaxial tests.

Resonant column tests were conducted on both loose and dense dry silica gel specimens. It was discovered that the confining stress and the void ratio strongly

influence the dynamic properties of the dry silica gel at a low strain level. The grain size had a secondary influence on the dynamic properties of the silica gel. The small-strain shear modulus of silica gel with a smaller void ratio was higher than that of silica gel with a large void ratio. However, once the confining pressure was higher than 400 kPa, silica gels tended to have a constant small-strain shear modulus irrespective of the initial void ratio and the confining pressure. By comparing the behavior of sand from the previous researcher's work, it was found that silica gel had a very similar dynamic behavior as the sand under a low confining pressure. However, the silica gel displayed a different dynamic behavior compared with sand under a high confining pressure. The maximum shear modulus of silica gel tended to slow its increase when the confining stress became higher. The linear threshold shear strain, γ_{ll} , was greater for silica gel at low confining pressure than that at high confining pressure. This is contrary to the behavior of natural sand. The damping behavior of silica gel was different from the damping behavior of sand. The damping ratio of silica gel increased with increasing confining pressure, which was opposite to that of sand. In Iskander's work, it was noticed that the silica gel would have to experience a much higher deformation than natural sand to reach the peak shear strength; and the elastic modulus of silica gel is also lower than that of sand. These highly nonlinear yielding characteristics of silica gel grains might explain why the dynamic behavior of silica gel is different from that of sand under high confining pressure. This research compared two different damping ratio determination methods—the free vibration and half-power method. At a low strain level, the two methods gave consistent damping ratio data; however, the half-power method gave higher damping ratio data when the shear strain became higher. When using the half-power method to determine the damping ratio data, it was limited to the low strain level.

The PIV technique is a sophisticated image pattern matching technique. A neural network camera calibration algorithm was developed in this research and then applied to the PIV technique. This calibration method can also be applied to the image-based measurement system. It does not require the special setup of the camera and the objects. Its accuracy has been compared with the commonly used methods: the linear model and the polynomial model. The comparison proved that the neural network camera calibration

method gives the best accuracy. Its application to PIV has been illustrated in the research through a strip footing on the sand model.

The combination of the PIV technique and transparent soil was applied successfully to visualize the dynamic interaction between the rigid block and the transparent soil. The PIV technique can capture the instantaneous velocity field of the transparent soil at any time during a shaking event. The PIV technique can give the full field information for the interaction of the rigid block and the soil. The displacement-time history for any interesting point in the soil mass can be obtained through this analysis. The free-field motion shake table test performed in this research clearly showed the amplification effects as the wave propagated upward from the soil bottom. Two small-scale shake table tests were carried out on the small wood block-soil model with the input sinusoidal wave at 2Hz frequency with the amplitude 0.25 in. (0.635 cm) and 0.5 in. (1.27 cm). The testing results showed that the rigid wood block failed with a bearing capacity type of failure. The time history of the rotating angle showed that under the same input frequency, a larger amplitude of the input excitation would more easily overturn the rigid block. The block does not exhibit the impact and gap behavior before it starts overturning.

7.2. RECOMMENDATIONS FOR FUTURE RESEARCH WORK

From this research, more research areas have been identified and recommended for future study.

Several types of low viscosity pore fluids for transparent soil were identified in this research. However, these pore fluids are potentially hazardous chemical solvents, and a special handling care is required. New user-friendly and nonhazardous pore fluids need to be discovered to facilitate the use of the transparent silica gel in broader applications. The dynamic properties of dry silica gel have been tested extensively under different densities. The existence of pore fluid would have a very small influence on the dynamic properties of the sand (Hardin and Richart, 1963). However, no such proof exists for the silica gel samples. The silica gel samples with different pore fluid contents need to be tested to get the correct answer to this question.

The low viscosity pore fluid will probably change the permeability of the silica gel samples. The permeability of the silica gel specimens will be higher than the sand samples. The permeability test should be conducted to get the range of the permeability coefficient for the silica gel samples when using the low viscosity pore fluid.

This study found that the laser light could not give a clear image pattern about the studying area in the transparent soil. It was believed that the laser light was too weak to have enough refraction with the silica gel particles. In future research, it is recommended to use the strong laser power light in the testing setup. One alternative way is to use two weak laser power lights in the test. This will also help to enhance the image quality. A good and clear image is the most important aspect of obtaining high quality velocity data. Only a limited number of shake table tests were conducted to investigate the dynamic interaction between the rigid block and the transparent soil. The amplitude influence at the same input frequency was investigated in this research. Many factors affect the interaction behavior between the rigid-block and the transparent soil, such as different embedment depth, the frequency effect of the input motion with the same amplitude, the geometric effect of the building itself, and the different soil conditions. Therefore, future research focusing on the effects of these parameters effect is strongly recommended.

Experimental work on the rigid-block soil interaction is important. In addition, numerical simulation is a necessary part of the investigation. Further numerical simulation on the performed shake table test is encouraged. The numerical simulation can be compared with the experimental results to check the accuracy of the numerical model.

APPENDIX. THE VISCOSITY DATA OF CHEMICAL SOLVENTS USED

Chemical Solvent ---- Heptane

Temperature	Temperature	Time	Viscosity Constant	Viscosity	Density	Dynamic Viscosity
Kelvin	°C	Second	cSt/second	cSt	g/cm ³	mPa.s
288.15	15	270.72	0.00229055	0.620	0.688	0.426
288.15	15	267.93	0.00229055	0.614	0.688	0.422
283.15	10	283.16	0.00229105	0.649	0.694	0.450
283.15	10	281.31	0.00229105	0.644	0.694	0.447
303.15	30	238.72	0.00228905	0.546	0.655	0.358
303.15	30	236.25	0.00228905	0.541	0.655	0.354
298.15	25	245.43	0.00228955	0.562	0.659	0.370
298.15	25	244.37	0.00228955	0.559	0.659	0.369
293.15	20	255.66	0.00229005	0.585	0.675	0.395
293.15	20	253.75	0.00229005	0.581	0.675	0.392

Chemical Solvent ---- 2,2,4-Trimethylpentane

Temperature	Temperature	Time	Viscosity Constant	Viscosity	Density	Dynamic Viscosity
Kelvin	°C	Second	cSt/second	cSt	g/cm ³	mPa.s
288.15	15	338.15	0.00229055	0.775	0.711	0.551
288.15	15	335.23	0.00229055	0.768	0.711	0.546
283.15	10	354.12	0.00229105	0.811	0.677	0.549
283.15	10	353.63	0.00229105	0.810	0.677	0.548
303.15	30	289.84	0.00228905	0.663	0.669	0.444
303.15	30	289.09	0.00228905	0.662	0.669	0.443
298.15	25	303.44	0.00228955	0.695	0.682	0.474
298.15	25	303.12	0.00228955	0.694	0.682	0.473

Chemical Solvent ---- Toluene

Temperature	Temperature	Time	Viscosity Constant	Viscosity	Density	Dynamic Viscosity
Kelvin	°C	Second	cSt/second	cSt	g/cm ³	mPa.s
288.15	15	323.03	0.00229055	0.740	0.886	0.656
288.15	15	317.22	0.00229055	0.727	0.886	0.644
283.15	10	341.37	0.00229105	0.782	0.909	0.711
283.15	10	335	0.00229105	0.768	0.909	0.698
303.15	30	269.38	0.00228905	0.617	0.833	0.514
303.15	30	266.97	0.00228905	0.611	0.833	0.509
298.15	25	280.22	0.00228955	0.642	0.849	0.545
298.15	25	281.56	0.00228955	0.645	0.849	0.548
293.15	20	300.09	0.00229005	0.687	0.864	0.594
293.15	20	317.72	0.00229005	0.728	0.864	0.628

Chemical Solvent ---- Iso-Butanol

Temperature	Temperature	Time	Viscosity Constant	Viscosity	Density	Dynamic Viscosity
Kelvin	°C	Second	cSt/second	cSt	g/cm ³	mPa.s
288.15	15	323.03	0.007991	2.581	0.886	2.288
288.15	15	317.22	0.007991	2.535	0.886	2.247
283.15	10	341.37	0.007994	2.729	0.909	2.481
283.15	10	335	0.007994	2.678	0.909	2.435
303.15	30	269.38	0.007982	2.150	0.833	1.791
303.15	30	266.97	0.007982	2.131	0.833	1.775
298.15	25	525.4	0.007985	4.195	0.877	3.678
298.15	25	523.45	0.007985	4.180	0.877	3.664
293.15	20	300.09	0.007988	2.397	0.864	2.070
293.15	20	317.72	0.007988	2.538	0.864	2.192

Chemical Solvent ---- Ethyl Acetate

Temperature	Temperature	Time	Viscosity Constant	Viscosity	Density	Dynamic Viscosity
Kelvin	°C	Second	cSt/second	cSt	g/cm ³	mPa.s
288.15	15	219.66	0.00229055	0.503	0.893	0.449
288.15	15	221.19	0.00229055	0.507	0.893	0.452
283.15	10	226.28	0.00229105	0.518	0.899	0.466
283.15	10	226.12	0.00229105	0.518	0.899	0.466
303.15	30	201.6	0.00228905	0.461	0.880	0.406
303.15	30	200.4	0.00228905	0.459	0.880	0.404
298.15	25	206.5	0.00228955	0.473	0.889	0.420
298.15	25	205.72	0.00228955	0.471	0.889	0.419
293.15	20	211.84	0.00229005	0.485	0.893	0.433
293.15	20	211.91	0.00229005	0.485	0.893	0.434

Chemical Solvent ---- Methyl Ethyl Ketone

Temperature	Temperature	Time	Viscosity Constant	Viscosity	Density	Dynamic Viscosity
Kelvin	°C	Second	cSt/second	cSt	g/cm ³	mPa.s
288.15	15.00	219.62	0.00229055	0.50	0.66	0.33
288.15	15.00	219.38	0.00229055	0.50	0.66	0.33
283.15	10.00	225.50	0.00229105	0.52	0.68	0.35
283.15	10.00	226.20	0.00229105	0.52	0.68	0.35
303.15	30.00	202.09	0.00228905	0.46	0.64	0.29
303.15	30.00	203.40	0.00228905	0.47	0.64	0.30
298.15	25.00	207.00	0.00228955	0.47	0.65	0.31
298.15	25.00	205.84	0.00228955	0.47	0.65	0.30
293.15	20.00	212.80	0.00229005	0.49	0.65	0.32
293.15	20.00	213.20	0.00229005	0.49	0.65	0.32

Chemical Solvent ---- Cyclohexane

Temperature	Temperature	Time	Viscosity Constant	Viscosity	Density	Dynamic Viscosity
Kelvin	°C	Second	cSt/second	cSt	g/cm ³	mPa.s
288.15	15	579.5	0.00229055	1.327	0.773	1.026
288.15	15	580.1	0.00229055	1.329	0.773	1.027
283.15	10	644.82	0.00229105	1.477	0.782	1.155
283.15	10	642.75	0.00229105	1.473	0.782	1.151
303.15	30	462.13	0.00228905	1.058	0.748	0.791
303.15	30	461.97	0.00228905	1.057	0.748	0.791
298.15	25	499.71	0.00228955	1.144	0.759	0.868
298.15	25	497.91	0.00228955	1.140	0.759	0.865
293.15	20	537	0.00229005	1.230	0.779	0.958
293.15	20	536.69	0.00229005	1.229	0.779	0.958

Chemical Solvent ----2 Propanol

Temperature	Temperature	Time	Viscosity Constant	Viscosity	Density	Dynamic Viscosity
Kelvin	°C	Second	cSt/second	cSt	g/cm ³	mPa.s
288.15	15	323.03	0.007991	2.581	0.886	2.288
288.15	15	317.22	0.007991	2.535	0.886	2.247
283.15	10	341.37	0.007994	2.729	0.909	2.481
283.15	10	335	0.007994	2.678	0.909	2.435
303.15	30	269.38	0.007982	2.150	0.833	1.791
303.15	30	266.97	0.007982	2.131	0.833	1.775
298.15	25	333.6	0.007985	2.664	0.849	2.262
298.15	25	334.1	0.007985	2.668	0.849	2.266
293.15	20	300.09	0.007988	2.397	0.864	2.070
293.15	20	317.72	0.007988	2.538	0.864	2.192

Chemical Solvent ---- Acetonitrile

Temperature	Temperature	Time	Viscosity Constant	Viscosity	Density	Dynamic Viscosity
Kelvin	°C	Second	cSt/second	cSt	g/cm ³	mPa.s
288.15	15	323.03	0.00229055	0.740	0.886	0.656
288.15	15	317.22	0.00229055	0.727	0.886	0.644
283.15	10	341.37	0.00229105	0.782	0.909	0.711
283.15	10	335	0.00229105	0.768	0.909	0.698
303.15	30	269.38	0.00228905	0.617	0.833	0.514
303.15	30	266.97	0.00228905	0.611	0.833	0.509
298.15	25	194.5	0.00228955	0.445	1.096	0.488
298.15	25	193.56	0.00228955	0.443	1.096	0.486
293.15	20	300.09	0.00229005	0.687	0.864	0.594
293.15	20	317.72	0.00229005	0.728	0.864	0.628

Chemical Solvent ---- Pyridine

Temperature	Temperature	Time	Viscosity Constant	Viscosity	Density	Dynamic Viscosity
Kelvin	°C	Second	cSt/second	cSt	g/cm ³	mPa.s
288.15	15	445.59	0.00229	1.021	0.990	1.010
288.15	15	440.87	0.00229	1.010	0.990	1.000
283.15	10	460.94	0.00229	1.056	0.991	1.047
283.15	10	461.31	0.00229	1.057	0.991	1.047
303.15	30	371.88	0.00229	0.851	0.966	0.822
303.15	30	368.72	0.00229	0.844	0.966	0.815
298.15	25	395.09	0.00229	0.905	0.974	0.881
298.15	25	394.84	0.00229	0.904	0.974	0.881
293.15	20	419.78	0.00229	0.961	0.988	0.950
293.15	20	418.91	0.00229	0.959	0.996	0.955

Chemical Solvent ---- Norpar 12

Temperature	Temperature	Time	Viscosity Constant	Viscosity	Density	Dynamic Viscosity
Kelvin	°C	Second	cSt/second	cSt	g/cm ³	mPa.s
288.15	15	323.03	0.00229055	0.740	0.886	0.656
288.15	15	317.22	0.00229055	0.727	0.886	0.644
283.15	10	341.37	0.00229105	0.782	0.909	0.711
283.15	10	335	0.00229105	0.768	0.909	0.698
303.15	30	269.38	0.00228905	0.617	0.833	0.514
303.15	30	266.97	0.00228905	0.611	0.833	0.509
298.15	25	284.738	0.00228955	0.652	0.848	0.551
298.15	25	293.555	0.00228955	0.672	0.848	0.571
293.15	20	300.09	0.00229005	0.687	0.864	0.594
293.15	20	317.72	0.00229005	0.728	0.864	0.628

Chemical Solvent ----Lamp Oil

Temperature	Temperature	Time	Viscosity Constant	Viscosity	Density	Dynamic Viscosity
Kelvin	°C	Second	cSt/second	cSt	g/cm ³	mPa.s
288.15	15	323.03	0.007991	2.581	0.886	2.288
288.15	15	317.22	0.007991	2.535	0.886	2.247
283.15	10	341.37	0.007994	2.729	0.909	2.481
283.15	10	335	0.007994	2.678	0.909	2.435
303.15	30	269.38	0.007982	2.150	0.833	1.791
303.15	30	266.97	0.007982	2.131	0.833	1.775
298.15	25	262.22	0.007985	2.094	0.849	1.778
298.15	25	248.59	0.007985	1.985	0.849	1.686
293.15	20	300.09	0.007988	2.397	0.864	2.070
293.15	20	317.72	0.007988	2.538	0.864	2.192

BIBLIOGRAPHY

Abdel-Aziz Y.I. and Karara H. M. (1971), "Direct Linear Transformation into Object Space Coordinates in Close-Range Photogrammetry." Proc. Symposium on Close-Range Photogrammetry, Urbana, Illinois, pp. 1-18.

Adrian R. (1991), "Particle-Imaging Techniques for Experimental Fluid Mechanics." Annual Review Fluid Mechanics, 23, pp. 261-304.

Bouguet J.-Y., and Perona P. (1998), "Camera Calibration from Points and Lines in Dual-Space Geometry," Fifth European Conference on Computer Vision (ECCV '98), 2-6 June, Freiburg, Germany.

Drnevich V.P., Hardin B.O., and Shippy D.J. (1978), "Modulus and Damping of Soils by the Resonant-Column Method." *Dynamic Geotechnical Testing*. American Society for Testing and Materials, Special Technical Publication STP 654, Philadelphia, PA, pp. 91-125.

Fritz H.M. (2000), "PIV Applied to Landslide Generated Impulse Waves." Proceedings of 10th International Symposium on Applications of Laser Techniques to Fluid Mechanics, Calouste Gulbenkian Foundation, 10-13 July, 2000, Lisbon, Portugal, Eds. Adrian, R.J. et al.

Gazetas G., Apostolou M., and Anastasopoulos J. (2003), "Seismic Uplifting of Foundation Soft Soil, with Examples from Adapazari (Izmit 1999 earthquake)." the International Conference of the British Geotechnical Association: Foundations - Innovations, Observations, Design & Practice, in the University of Dundee, Scotland, September 2-5, 2003.

Gazetas G. and Apostolou M. (2004), "Nonlinear Soil-Structure Interaction: Foundation Uplifting and Soil Yielding." Proceedings Third UJNR Workshop on Soil-Structure Interaction, March 29-30, 2004, Menlo Park, California, USA

GCT Resonant Column Testing Manual, Geotechnical Engineering Testing and Consultants, Inc.

Guler M., Edil T. B., and Bosscher P. J. (1999), "Measurement of Particle Movement in Granular Soils Using Image Analysis," *Journal of Computer Civil Engineering*, Vol. 21, pp. 116–122.

Hardin B.O., and Drnevich P.P. (1972 a), "Shear Modulus and Damping in Soils: Measurement and Parameter Effects." *Journal of Soil Mechanics and Foundations*, ASCE, Vol. 98, No. 6, pp. 603-624.

Hardin B.O., and Drnevich P.P. (1972 b), "Shear Modulus and Damping in Soils: Design Equations and Curves." *Journal of Soil Mechanics and Foundations*, ASCE, Vol. 98, No. 7, pp. 667-692.

Harris C. and Stephens M. (1998), "A Combined Corner and Edge Detector." In *Alvey Vision Conference*, pp. 147–151.

Hayashi Y. (1996), "Damage Reduction Effect due to Basemat Uplift of Buildings." *J. Struct. Constr. Engng*, Vol. 485, pp. 53-62 (in Japanese).

Hayashi Y., Tamura K., Mori M. and Takahashi I. (1999), "Simulation Analyses of Buildings Damaged in the Kobe, Japan, Earthquake Considering Soil-Structure Interaction." *Earthquake Engineering and Structural Dynamics*, Vol. 28, pp. 371-391.

Heikkila J., and Silven O. (1997), "A Four-Step Camera Calibration Procedure with Implicit Image Correction." *IEEE Computer Society Conference on Computer Vision and Pattern Recognition (CVPR'97)*, San Juan, Puerto Rico, pp. 1106–1112.

Housner, G. (1963), "The Behavior of Inverted Pendulum Structure During Earthquakes," *Bulletin of the Seismological Society of America*, Vol. 53, No. 2, pp. 403-417.

Hunt R. (1984), "Geotechnical Engineering Investigation Manual," McGraw-Hill, Inc.

Iai S. (1989), "Similitude for Shaking Table Tests on Soil-Structure-Fluid Model in 1g Gravitation Field," *Soils and Foundations*, Vol. 29, No.1, 105-118, March, 1989.

Iskander M., Lai J., Oswald C., and Mannheimer R. (1994), "Development of a Transparent Material to Model the Geotechnical Properties of Soils." *ASTM Geotechnical Testing Journal*, 17(4), pp. 425-433.

Iskander, M. (1998), "Transparent Soils to Image 3D Flow and Deformation." *Proc., 2nd Int. Conf. on Imaging Technologies: Techniques and Applications in Civil Engineering*, ASCE, New York, pp. 255-264.

Iskander M., Liu J., and Sadek S. (2002a), "Transparent Amorphous Silica to Model clay." *Journal of Geotechnical and Geoenvironmental Engineering*, Vol. 128 (3), pp. 262-273.

Iskander, M., Sadek, S., and Liu, J. (2002b), "Optical Measurement of Deformation Using Transparent Silica Gel to Model Sand." *International Journal of Physical Modeling in Geotechnics*, No. 4 (2002), pp. 27-40.

Iskander M. (1998), "Transparent Soils to Image 3D Flow and Deformation." *Proc., 2nd Int. Conf. on Imaging Technologies: Techniques and Applications in Civil Engineering*, ASCE, New York, pp. 255-264.

Iskander, M., Liu, J-Y, and Sadek, S. (2003), "Modeling 3D Flow & Soil Structure Interaction Using Optical Tomography," *Final Report NSF No. CMS 9733064*, 2003.

Ishibashi, I. and Zhang, X. (1993), "Unified Dynamic Shear Moduli and Damping Ratios of Sand and Clay." *Soils and Foundations*, Vol. 33, No.1, pp. 182-191.

Koh, A.-S., Spanos, D.P., and Roesset, M.J. (1986), "Harmonic Rocking of Rigid Block on Flexible Foundation." *Journal of Engineering Mechanics*, Vol. 112, No. 11, pp. 1165-1180.

Laird, J.P. and Stokoe, K.H. (1993), "Dynamic Properties of Remolded and Undisturbed Soil Samples Tested at High Confining Pressures." *Geotechnical Engineering Report GR93-6*, Electric Power Research Institute, Palo Alto, CA.

Langharr, H. L. (1951), "Dimensional Analysis and Theory of Models." New York: Wiley and Sons.

Lamb H. (1932), *Hydrodynamics*, 6th ed. Cambridge.

Lawrence, F.V., Jr. (1963), "Propagation Velocity of Ultrasonic Waves through Sand." *MIT Research Report R63-8*, Massachusetts Institute of Technology, Cambridge, Massachusetts.

Lueptow, R.M., Akonur, A. & Shinbrot, T. (2000), "PIV for Granular Flows." *Experiments in Fluids*, Vol. 28, pp. 183-186.

Mannheimer, R.J., Oswald, C.J. (1993), "Development of Transparent Porous Media with Permeabilities and Porosities Comparable to Soils." *Ground Water GRWAAP*, Vol. 31, No.5, pp. 781-788, September/October, 1993.

MatLab 7th Edition, The MathWorks, Inc., 2004.

Melen, T. (1994), "Geometrical Modelling and Calibration of Video Cameras for under Water Navigation." Dr. ing Thesis, Norges Tekniske Hogskole, Institutt for Teknisk Kybernetikk.

Michalowski, R. L. and Shi, L. (2002), "Deformation Patterns of Reinforced Foundation Sand at Failure." *ASCE Journal of Geotechnical and Geoenvironmental Engineering*, 129 (5), pp. 439-449.

Muto K., Umemura H. and Sonobe Y. (1960), "Study of the Overturning of Slender Structures." *Proceedings of the Second World Conference on Earthquake Engineering*, Tokyo, pp. 1239-1261.

Paikowsky, S.G., and Xi, F. (2000), "Particle Motions Tracking Utilizing a High-Resolution Digital CCD Camera," *Geotechnical Testing Journal*, 23(1), pp. 123-134.

Psycharis (1982), "Dynamic Behavior of Rocking Structures Allowed to Uplift." Ph.D. Thesis, California Institute of Technology.

Rechenmacher, A.L., and Finno, R.J. (2004), "Digital Image Correlation to Evaluate Shear Banding in Dilative Sands." *ASTM Geotechnical Testing Journal*, 27 (1), pp. 13-22.

Richart, F.E., Jr. (1977), "Dynamic Stress-Strain Relations for Soils, State of Art Report." *Proceedings of the Ninth International Conference on Soil Mechanics and Foundation Engineering*, Tokyo, Vol. 2, 1977, pp. 605-612.

Sadek, S., Iskander, M.G., Liu, J. (2003). "Accuracy of Digital Image Correlation for Measuring Deformations in Transparent Media." *ASCE Journal of Computing in Civil Engineering*, 17(2), pp. 88-96.

Seed, H.B. and Idriss, I.M. (1970), "Soil Moduli and Damping Factors for Dynamic Response Analysis," *Report EERC 70-10*, Earthquake Engineering Research Center, University of California, Berkeley.

Slama, C.C. (ed.) (1980), "Manual of Photogrammetry." 4th ed., American Society of Photogrammetry, Falls Church, Virginia.

Sousa, J. (2002), "Turbulent Flow around a Surface Mounted Obstacle Using 2D-3C DPIV." *Experiments in Fluids*, Vol. 33, pp. 854-862.

Sitharam, T.G., GovindaRaju, L., and Sridharan, A. (2004), "Dynamic Properties and Liquefaction Potential of Soils." *Special Section: Geotechnics and Earthquake Hazards, Current Science*, Vol. 87, No. 10, pp. 1370-1378.

Sveen, J.K. (2004), *An Introduction to MatPIV v.1.6.1*. Eprint No. 2, ISSN 0809-4403, Dept. of Math., University of Oslo

Take W.A. (2003), "The Influence of Seasonal Moisture Cycles on Clay Slopes." Ph.D. dissertation (University of Cambridge)

Terzaghi, K. (1943), *Theoretical Soil Mechanics*, John Wiley and Sons, New York.

Tsai, R.Y. (1987), "A Versatile Camera Calibration Technique for High-Accuracy 3D Machine Vision Metrology Using Off-the-Shelf TV Cameras and Lenses." *IEEE Journal of Robotics and Automation* RA-3(4), pp. 323-344.

Wartman, J. (1996), "The Effect of Fly Ash on the Geotechnical Properties of a Soft Clay." M. Eng. Thesis, University of California Berkeley.

Welker, et al., Bowders, J.J., and Gilbert, R.B. (1999), "Applied Research Using a Transparent Material with Hydraulic Properties Similar to Soil," *Geotechnical Testing Journal*, GTJODJ, Vol. 22, No. 3, September, pp. 266-270.

Weng, J., Cohen, P. & Herniou, M. (1992), "Camera Calibration with Distortion Models and Accuracy Evaluation." *IEEE Transactions on Pattern Analysis and Machine Intelligence*, PAMI-14 (10), pp. 965-980.

White, D.J. (2002), "An Investigation into the Behavior of Pressed-in Piles." PhD dissertation (University of Cambridge).

White, D. J., Take, W.A., and Bolton, M. D. (2003), "Soil Deformation Measurement Using Particle Image Velocimetry (PIV) and Photogrammetry." *Geotechnique*, Vol. 53(7), pp. 619-631.

White, D. J., Randolph, M.F., and Thompson, B. (2005), "An Image-based Deformation Measurement System for Geotechnical Centrifuge." *International Journal on Physical Modeling in Geotechnics*, Vol. 5, No.3, pp. 1-12.

Zhang, J. and Markris, N. (2001), "Rocking Response of Free-Standing Blocks under Cycloidal Pulses." *Journal of Engineering Mechanics*, Vol. 127, No. 5, pp. 473-483.

Zienkiewicz, O.C., F. R. S., Chan, A.H.C., Pastor M., Paul, D.K., and Shiomi T. (1990), "Static and Dynamic Behavior of Soils: a Rational Approach to Quantitative Solutions. I. Fully Saturated Problems." *Proc. R. Soc., Lond., A* 429, pp. 285-309.

VITA

Honghua Zhao, was born on March 20, 1977, in Xiyiao Village, Yuncheng County, Shandong Province, China. She entered the Xiyiao elementary school at the age of eight. After finishing elementary school, she entered the Nanzhaolou Middle School in the fall of 1989. There, she started to learn all kinds of new knowledge such as English, Physics, Chemistry, and Algebra.

After three years of middle school life, she entered the Fourth High School in the town of Huangji in 1992. In the fall of 1995, after three years of high school, she entered the Changsha Communications College (renamed as the Changsha Institute of Technology after merging with the Changsha Power College in 2003). She majored in civil engineering, focusing on structural design. She received a Bachelor's degree in June 1999. In the fall of 1999, she was admitted by the Graduate School of Tongji University and started her graduate studies, focusing on geotechnical engineering. There, she did research on the anisotropic properties of Shanghai yellow soft clay. In May 2002, she received her Master's degree in Geotechnical engineering from Tongji University.

In fall 2002, she began her PhD studies in University of Missouri-Rolla focusing on geotechnical engineering. For the first two years, she worked together with Dr. Thomas Petry to study the chemical stabilization on expansive clay. For the following two and half years, she worked with Dr. Yu-Ning Ge to study the visualization of dynamic soil-structure interaction using transparent soil and the PIV technique. There, she studied the geotechnical engineering systematically and embraced much more new knowledge in the Geotechnical Engineering field. In May 2007, she graduated from UMR with a Ph.D. in Civil Engineering.